이학박사학위논문

Tectonometamorphic evolution of high-pressure eclogites and associated metasedimentary rocks in the Lanterman Range, northern Victoria Land, Antarctica

남극 북빅토리아랜드 랜터만 산맥의 고압
에클로자이트와 주변 변성퇴적암류의
변성지구조적 진화

2019년 8월

서울대학교 대학원

지구환경과학부

김 태 환

Tectonometamorphic evolution of high-pressure eclogites and associated metasedimentary rocks in the Lanterman Range, northern Victoria Land, Antarctica

남극 북빅토리아랜드 랜터만 산맥의 고압 에클로자이트와 주변 변성퇴적암류의 변성지구조적 진화

지도교수 정 해 명

이 논문을 이학박사 학위논문으로 제출함

2019년 8월

서울대학교 대학원

지구환경과학부

김 태 환

김태환의 이학박사 학위논문을 인준함

2019년 8월

위 원 장 _____

부위원장 _____

위 원 _____

위 원 _____

위 원 _____

Tectonometamorphic evolution of high-pressure eclogites and associated metasedimentary rocks in the Lanterman Range, northern Victoria Land, Antarctica

Taehwan KIM

A dissertation submitted in partial fulfillment of the requirements for the degree of Doctor of Philosophy

School of Earth and Environmental Sciences
Graduate School
Seoul National University

August 2019

ABSTRACT

Tectonometamorphic evolution of high-pressure eclogites and associated metasedimentary rocks in the Lanterman Range, northern Victoria Land, Antarctica

Taehwan Kim
School of Earth and Environmental Sciences
Graduate School
Seoul National University

The Lanterman Range eclogites and associated metasedimentary rocks in the Lanterman Range, northern Victoria Land, Antarctica, were investigated to unravel tectonometamorphic evolution of high-pressure (*P)* terrane in the Andean-type Ross orogeny. The pristine eclogites primarily consisting of garnet + omphacite + calcic/sodic-calcic amphibole + epidote + phengite + rutile + quartz, revealed three stages of prograde metamorphism defining two distinctive *P–T* trajectories, $M_{1–2}$ and M_3. A combination of pseudosection modelling, mineral parageneses and thermobarometries suggests that the eclogites have initially evolved from ~15–20 kbar and 520–570 °C (M_1) through ~22–25 kbar and 630–650 °C (M_2), and finally to ~26 ± 3 kbar and 720 ± 80 °C (M_3). The SHRIMP U-Pb dating discriminated two distinct episodes of eclogitic zircon growth at 515 ± 4 Ma (*t*σ; M_2) and 498 ± 11 Ma (*t*σ; M_3) from zircon mantle and rim, respectively. Average burial rates are too low (<2 mm/year) for cold subduction regime (~5–10 °C/km), suggesting an intervening exhumation stage between two prograde *P–T* segments. Thus, two discrete events of burial-exhumation took place with an *c.* 15 Ma gap during the Ross orogeny.

The inherited zircon core ages (590.8 ± 8.3 Ma and 603.2 ± 4.4 Ma, *t*σ) and mildly alkalic, within-plate to continental basalt-like geochemistry of

the eclogites were combined to suggest that their gabbroic protoliths should be a spatial-temporal equivalent to *c.* 600–580 Ma rift to passive margin magmatic rocks in the Tasmanides of eastern Australia. This is the first discovery of Ediacaran rift-related magmatism in the Ross orogen, thereby fulfilling the Antarctic missing link for paleogeographic linkage between Australia and Antarctica during the Neoproterozoic. Furthermore, I suggest oceanward propagation of rifting along the Australian-Antarctic margins from Cryogenian (*c.* 670–650 Ma) to Ediacaran (*c.* 600–580 Ma), followed by two discrete tectonic inversion events at Ediacaran (*c.* 590–570 Ma) and early Cambrian (*c.* 540–530 Ma), respectively. These late Neoproterozoic rift-related events might be responsible for the Pacific-Gondwana zircon population (*c.* 700–500 Ma) in the Paleozoic Gondwana 'mud-pile'.

Manganiferous quartzitic schist rarely occurs as thin layer in the Lanterman Range, intercalated within the quartzofeldspathic schists and gneisses enveloping the metamafic lenses. Strong positive anomaly of Ce of the manganiferous quartzite confirmed incorporation of ferromanganese deposits in the pelagic sedimentary protolith, most likely at continental slope to shelf of passive margin setting. Mineral assemblages represented by spessartine-rich garnet, piemontite-allanite-rich epidote, phengite, magnetite and quartz suggested greenschist to blueschist facies conditions with the relatively high oxygen fugacity. Passive margin sedimentary packages were metamorphosed at middle Cambrian time in the context the Ross orogeny. A compilation of *P–T* paths of high-*P* metamorphic rocks in the Lanterman Range testifies differing subduction-exhumation paths.

Keywords: eclogite, episodic zircon growth, late Neoproterozoic rifting, manganiferous quartzite, Lanterman Range, Ross orogen, East Gondwana margin

TABLE OF CONTENTS

ABSTRACT i

TABLE OF CONTENTS iii

LIST OF FIGURES vi

LIST OF TABLES viii

CHAPTER I: Introduction 1

THE TRANSANTARCTIC MOUNTAINS, NORTHERN VICTORIA LAND AND LANTERMAN RANGE 2

SCOPE OF THESIS AND MAIN ACHIEVEMENT 4

REFERENCES 5

CHAPTER II: *P–T* evolution and episodic zircon growth in barroisite eclogites of the Lanterman Range, northern Victoria Land, Antarctica 7

ABSTRACT 8

INTRODUCTION 10

GEOLOGICAL BACKGROUND 14

SAMPLE DESCRIPTION AND PETROGRAPHY 18

ANALYTICAL METHODS 25

MINERAL CHEMISTRY 26

METAMORPHIC EVOLUTION 46

PRESSURE AND TEMPERATURE ESTIMATIONS 49

ZIRCON GEOCHRONOLOGY 59

DISCUSSTION 69

CONCLUSIONS 76

REFERENCES 77

CHAPTER III: Mafic magmatism at *c.* 590 Ma in the Ross orogen, Antarctica: The Ediacaran missing link for continental rifting and detrital zircon source along the East Gondwana margin 96

ABSTRACT 97
INTRODUCTION 98
GEOLOGICAL BACKGROUND 102
GEOCHEMICAL AND GEOCHRONOLOGICAL RESUTLS 103
DISCUSSION 133
CONCLUSIONS 139
REFERENCES 140

CHAPTER IV: Petrogenesis of manganiferous quartzite in the Lanterman Range, northern Victoria Land, Antarctica 148

ABSTRACT 149
INTRODUCTION 150
GEOLOGICAL BACKGROUND 153
SAMPLE DESCRIPTION AND PETROGRAPHY 157
ANALYTICAL METHODS 163
MINERAL CHEMISTRY 164
METAMORPHIC EVOLUTION AND *P–T* ESTIMATION 176
WHOLE-ROCK GEOCHEMISTRY 178
ZIRCON GEOCHRONOLOGY 180
DISCUSSION 183
CONCLUSIONS 185
REFERENCES 186

CHAPTER V: Conclusions and future work **193**

CONCLUSIONS 194
FUTURE WORK 195

ABSTRACT (in Korean) **198**

ACKNOWLEDGEMENTS 200
ACKNOWLEDGEMENTS (in Korean) 201

LIST OF FIGURES

Figure II-1. Simplified geological map of the study area.

Figure II-2. Geological map and outcrop photographs.

Figure II-3. Photomicrographs and backscattered electron images of the barroisite eclogites.

Figure II-4. X-ray maps and compositional profiles of garnet.

Figure II-5. Compositional diagrams of minerals.

Figure II-6. Mineral paragenesis diagram.

Figure II-7. *P*– and *T*–M_{H2O} pseudo-binary diagrams.

Figure II-8. *P*– and *T*–X_{Fe3+} pseudo-binary diagrams.

Figure II-9. *P*–*T* diagram of the thermobarometric results.

Figure II-10. *P*–*T* pseudosections of barroisite eclogites.

Figure II-11. Representative cathodoluminescence images of zircon.

Figure II-12. Backscattered electron images of zircon.

Figure II-13. Energy dispersive spectroscopy profiles of mineral inclusions in zircon.

Figure II-14. Tera-Wasserburg concordia diagram showing U-Pb zircon ages.

Figure III-1. Simplified geological map of the Australia and Antarctica.

Figure III-2. Whole-rock geochemical data of late Neoproterozoic mafic rocks from the Transantarctic Mountains and Tasmanides.

Figure III-3. Representative cathodoluminescence images of zircon.

Figure III-4. Tera-Wasserburg concordia diagram showing U-Pb zircon ages of sample E-1a.

Figure III-5. Tera-Wasserburg concordia diagram showing U-Pb zircon ages of sample E-1c.

Figure III-1. Simplified geological map of the study area.
Figure III-2. Geological map and outcrop photographs.
Figure III-3. Photomicrographs and backscattered electron images of the manganiferous quartzite.
Figure III-4. X-ray maps and compositional profiles of garnet.
Figure III-5. Backscattered electron image and X-ray maps of epidote group mineral.
Figure III-6. Compositional diagrams of minerals.
Figure III-7. Rare earth elements and yttrium concentration of epidote group mineral.
Figure III-8. Compilation of *P*–*T* paths of metamorphic rocks in the Lanterman Range.
Figure III-9. Whole-rock geochemistry of the manganiferous quartzite.
Figure III-10. Tera-Wasserburg concordia diagram showing U-Pb zircon ages.

LIST OF TABLES

Table II-1. Analytical conditions of the EPMA for rutile.

Table II-2. Representative analyses of rutile and the Zr-in-rutile temperatures.

Table II-3. Representative analyses of minerals in barroisite eclogites.

Table II-4. Whole-rock and effective bulk compositions.

Table II-5. SHRIMP U-Th-Pb isotopic compositions of zircon.

Table III-1. Compilation of geochemical data of rift-related mafic rocks in the Transantarctic Mountains and Tasmanides.

Table III-2. SHRIMP U-Th-Pb isotopic compositions of zircon.

Table IV-1. Representative analyses of minerals in manganiferous quartzite.

Table IV-2. SHRIMP U-Th-Pb isotopic compositions of zircon.

CHAPTER I

Introduction

THE TRANSANTARCTIC MOUNTAINS, NORTHERN VICTORIA LAND AND LANTERMAN RANGE

The Transantarctic Mountains (TAM), a backbone of the Antarctic continent, preserves lines of geologic evidence for: (1) the Neoproterozoic–early Paleozoic rift to passive margin formation associated with break-up of supercontinent Rodinia, and (2) the subsequent Ross orogeny during the late Neoproterozoic to Ordovician (e.g. Stump, 1995; Boger, 2011). Although tectonic evolution and correlation of the East Gondwana margins including the TAM and neighboring Tasmanides of eastern Australia has attracted much attention of previous studies (e.g. Flöttmann et al., 1993; Boger and Miller, 2004; Foden et al., 2006), it is largely unknown because of rare exposure of outcrops and overprinting effect of the accretion-type Terra Australis orogeny (Cawood, 2005).

Northern Victoria Land (NVL), situated at the Pacific end of the TAM, has been a key geologic province where continental arc evolution related to subduction of the paleo-Pacific plate has been documented (e.g. Kleinschmidt and Tessensohn, 1987). Previous studies on the basis of geological survey in NVL were largely covered by many geologists of various fields and countries such as United States, Germany, Italy, Australia, New Zealand, United Kingdom, and Soviet Union (for historical details on the Antarctic expedition in the TAM and NVL, refer to Stump, 1995 and Faure and Mensing, 2010, respectively). Among the priceless contributions to geology of Antarctica, those in NVL mainly came from the German and

Italian geologists. The team GANOVEX, German Northern Victoria Land Expeditions, published a comprehensive geological map of NVL, in cooperation with the Italian team (GANOVEX Team, 1987). In 1991, a preliminary work on structural evolution of the Wilson, Bowers and Robertson Bay terranes was presented (GANOVEX-ItaliAntartide, 1991). Among many aspects of geologic processes responsible for the NVL formation, the accretion of the Wilson and Bowers terranes has served as an obvious target for many studies by Italian geologists. Since the discovery of eclogites in the Lanterman Range (Ricci et al., 1996), the high-*P* metamorphic rocks such as metamafic boudins of eclogites and garnet amphibolites, and enclosing garnet–phengite schists/gneisses were intensively studied (e.g. Di Vincenzo et al., 1997; Capponi et al., 1999; Palmeri et al., 2011).

Geologists from Republic of Korea are now able to explore the Antarctic continent of NVL since the opening of Jang Bogo station in 2012 near Terra Nova Bay, where Gondwana Station (in 1982, German) and Mario Zuccheli Station (in 1986, Italy) were built. I collected the high-*P* rock samples from the Lanterman Range during the 2014/15 and 2015/16 season field work in Antarctica, and struggled to better understand the petrogenesis of the high-*P* rocks including mafic eclogites, amphibolites, garnet–phengite schists and gneisses and manganiferous quartzite.

SCOPE OF THESIS AND MAIN ACHIEVEMENT

In this thesis, I investigated metamorphic and tectonic evolution of the Lanterman Range eclogites and metasedimentary country rocks in the context of Ross orogeny and Neoproterozoic rifting along the East Gondwana margins. This thesis consists of three chapters, each of which is written as a separate paper. In the first chapter, the *P–T–t* evolution of pristine eclogites was constrained on the basis of pseudosection modelling of garnet-bearing assemblages and zircon geochronology. Focusing on prograde evolution, I confirmed that the eclogite facies metamorphism and zircon growth took place episodically at two distinct stages of Cambrian subduction burial during the Ross orogeny. This further implies the activity of the so-called yo-yo tectonics or cyclic subduction and exhumation.

The second chapter discusses tectonic setting of the eclogite protoliths and their correlation to rift-related rocks in the TAM and Tasmanides. I discovered for the first time the Ediacaran rift-related magmatism in the Ross orogen, using whole-rock geochemistry and zircon U-Pb ages of the eclogites. Although the metamafic rocks in the Lanterman Range vary in their geochemistry, a compilation of ages and geochemical data of late Neoproterozoic rift-related magmatism from the TAM and Tasmanides strongly supported their tectonic correlation. Further implications include a possible sedimentary provenance of the so-called Pacific-Gondwana zircon widespread in the late Neoproterozoic to Triassic (meta)sedimentary strata along the East Gondwana margins.

The last chapter deals with the manganiferous quartzite or ‘coticule’. This peculiar lithology has been commonly discovered at a small amount from high-*P* terranes such as Alps. I argued the pelagic protolith with ferromanganese deposit inputs, which are responsible for strong positive anomaly of Ce. The sedimentary protoliths formed at passive margin setting, and buried during the Ross orogeny. Zircon geochronology delineated the time frame from early Cambrian sedimentation to middle Cambrian metamorphism. Mineral assemblages consisting of Mn-bearing silicates and oxides were documented, implying that oxygen fugacity has remained high during prograde metamorphism and were responsible for the relict porphyroblasts of piemontite-rich epidote.

REFERENCES

Boger, S.D. (2011). Antarctica – Before and after Gondwana. *Gondwana Research*, 19, 335–371.

Boger, S.D., & Miller, J.McL. (2004). Terminal suturing of Gondwana and the onset of the Ross–Delamerian Orogeny: the cause and effect of an Early Cambrian reconfiguration of plate motions. *Earth and Planetary Science Letters,* 219, 35–48.

Capponi, G., Crispini, L., & Meccheri, M. (1999). Structural history and tectonic evolution of the boundary between the Wilson and Bowers terranes, Lanterman Range, northern Victoria Land, Antarctica. *Tectonophysics*, 312, 249–266.

Cawood, P.A. (2005). Terra Australis Orogen: Rodinia breakup and development of the Pacific and Iapetus margins of Gondwana during the Neoproterozoic and Paleozoic. *Earth-Science Reviews*, 69, 249–279.

Di Vincenzo, G., Palmeri, R., Talarico, F., Andriessen, P.A., & Ricci, C.A. (1997). Petrology and geochronology of eclogites from the Lanterman Range, Antarctica. *Journal of Petrology*, 38, 1391–1417.

Faure, G., & Mensing, T.M. (2010). *The Transantarctic Mountains – Rocks, ice, meteorites and water*. Springer. 804 pp.

Flöttmann, T., Gibson, G.M., & Kleinschmidt, G. (1993). Structural continuity of the Ross and Delamerian orogens of Antarctica and Australia along the margin of the paleo-Pacific. *Geology*, 21, 319–322.

Foden, J., Elburg, M.A., Dougherty-Page, J., & Burtt, A. (2006). The timing and duration of the Delamerian orogeny: Correlation with the Ross orogen and implications for Gondwana assembly. *Journal of Geology*, 114, 189–210.

GANOVEX-ItaliAntartide (1991). Preliminary geological-structural map of Wilson, Bowers, and Robertson Bay terranes in the area between Aviator and Tucker glaciers (northern Victoria Land, Antarctica). *Memorie della Società Geologica Italiana*, 46, 267–272.

GANOVEX team (1987). *German Antarctic North Victoria Land Expedition 1982/83: GANOVEX III (vol. 2)*, edited by F. Tessensohn & N. W. Roland, Geologisches Jahrbuch (vol. B66). Hannover: Bundesanstalt für Geowissenschaften und Rohstoffe. 324 pp.

Kleinschmidt, G., & Tessensohn, F. (1987). Early Paleozoic westward directed subduction at the Pacific margin of Antarctica. In G.D. McKenzie (Ed.), *Gondwana six: Structure, tectonics and geophysics.* American Geophysical Union (AGU) Geophysical Monograph Series (vol. 40, pp. 89–105). Washington, DC: AGU.

Palmeri, R., Talarico, F.M., & Ricci, C.A. (2011). Ultrahigh-pressure metamorphism at the Lanterman Range (northern Victoria Land, Antarctica). *Geological Journal*, 46, 126–136.

Ricci, C.A., Talarico, F., Palmeri, R., Di Vincenzo, G., & Pertusati, P.C. (1996). Eclogite at the Antarctic palaeo-Pacific active margin of Gondwana (Lanterman Range, northern Victoria Land, Antarctica). *Antarctic Science*, 8, 277–280.

Stump, E. (1995). *The Ross Orogen of the Transantarctic Mountains*, Cambridge: Cambridge University Press. 284 pp.

*CHAPTER II

P–T evolution and episodic zircon growth in barroisite eclogites of the Lanterman Range, northern Victoria Land, Antarctica

* This chapter was published in *Journal of Metamorphic Geology*
Kim, T., Kim, Y.,* Cho, M., & Lee, J. I. (2019). *P–T* evolution and episodic zircon growth in barroisite eclogites of the Lanterman Range, northern Victoria Land, Antarctica. *Journal of Metamorphic Geology*, v. 37, no. 4, p. 509–537, https://doi.org/10.1111/jmg.12474.

ABSTRACT

Prograde *P*–*T*–*t* paths of eclogites are often ambiguous owing to high variance of mineral assemblages, large uncertainty in isotopic age determinations and/or variable degree of retrograde equilibration. I investigated these issues using the barroisite eclogites from the Lanterman Range, northern Victoria Land, Antarctica, which are relatively uncommon but free of retrogression. These eclogites revealed three stages of prograde metamorphism, defining two distinctive *P*–*T* trajectories, $M_{1–2}$ and M_3. Inclusion minerals in garnet porphyroblasts suggest that initial prograde assemblages (M_1) consist of garnet + omphacite + barroisite/Mg-pargasite + epidote + phengite + paragonite + rutile/titanite + quartz, and subsequent M_2 assemblages of garnet + omphacite + barroisite + phengite + rutile ± quartz. The inclusion-rich inner part of garnet porphyroblasts preserves a bell-shaped Mn profile of the M_1, whereas the inclusion-poor outer part (M_2) is typified by the outward decrease in Ca/Mg and X_{Fe} (= $Fe^{2+}/(Fe^{2+} + Mg)$) values. A pseudosection modelling employing fractionated bulk-rock composition suggests that the eclogites have initially evolved from ~15–20 kbar and 520–570 °C (M_1) to ~22–25 kbar and 630–650 °C (M_2). The latter is in accordance with *P*–*T* conditions estimated from two independent thermobarometers: the garnet–clinopyroxene–phengite (~25 ± 3 kbar and 660 ± 100 °C) and Zr-in-rutile (~650–700 °C at 22–27 kbar). The second segment ($M_{3A–B}$) of prograde *P*–*T* path is recorded in the grossular-rich overgrowth rim of garnet. Apart from disequilibrium growth of the M_{3A}

garnet, ubiquitous overgrowth of the M_{3B} garnet permits to estimate the *P–T* conditions at ~26 ± 3 kbar and 720 ± 80 °C. The cathodoluminescence (CL) imaging of zircon grains separated from a barroisite eclogite revealed three distinct zones with bright rim, dark mantle and moderately dark core. Eclogitic phases such as garnet, omphacite, epidote and rutile are present as fine-grained inclusions in the mantle and rim of zircon, in contrast to their absence in the core. The sensitive high-resolution ion microprobe U-Pb dating on metamorphic mantle domains and neoblasts yielded a weighted mean $^{206}Pb/^{238}U$ age of 515 ± 4 Ma ($t\sigma$), representing the time of the M_2 stage. On the other hand, overgrowth rims as well as bright-CL neoblasts of zircon were dated at 498 ± 11 Ma ($t\sigma$), corresponding to the M_3. Average burial rates estimated from the M_2 and M_3 ages are too low (<2 mm/year) for cold subduction regime (~5–10 °C/km), suggesting that an exhumation stage intervened between two prograde segments of *P–T* path. Thus, the *P–T–t* evolution of barroisite eclogites is typified by two discrete episodes with an *c.* 15 Ma gap during the middle Cambrian subduction of the Antarctic Ross orogeny.

Keywords: Antarctic Ross orogen, barroisite eclogites, episodic zircon growth, northern Victoria Land, prograde *P–T* trajectories

INTRODUCTION

The worldwide occurrences of eclogite in suture zones are the product of high-*P* metamorphism along ancient subduction zones (e.g. Carswell, 1990; Smith, 1988), and many studies have investigated a variety of convergent margin processes, including the slab devolatilization and arc magmatism (e.g. Schmidt and Poli, 1998; Tatsumi, 1989), chemical recycling and mass transfer (e.g. Bebout, 2007; Zheng, 2012) and thermal evolution of convergent orogen (e.g. Peacock, 1996; Zhang et al., 2009). Tectonometamorphic evolution of eclogites has also received much attention of previous workers, and comprehensive studies are currently available for: (a) ultrahigh-*P* metamorphism (e.g. Chopin, 1984, 2003; Katayama et al., 2000; Liou et al., 2012); (b) the exhumation-juxtaposition process (e.g. Agard et al., 2009; Chen et al., 2013; Ernst et al., 1997) and (c) exhumation rates estimated from the paragenetic coupling of zircon and garnet (e.g. Baldwin et al., 2004; Kohn et al., 2015). However, prograde stages of eclogite facies metamorphism, particularly at medium to high temperatures (>550 °C; Carswell, 1990), are poorly constrained because low-*T* records are easily obliterated during the peak metamorphism and/or high-*T* retrogression (e.g. Essene, 1989; Krogh, 1982; Nakamura and Hirajima, 2000). Nevertheless, inclusion assemblages preserved within refractory minerals such as garnet permit to quantitatively determine a prograde *P–T* path. In particular, thermodynamic properties of solid-solution minerals such as omphacite and amphibole (Diener and Powell, 2012; Green et al.,

2007) have been significantly improved and the pseudosection modelling can be used to reproduce the eclogite facies parageneses (e.g. Palin et al., 2017; Rebay et al., 2010; Wei and Clark, 2011; Weller et al., 2016). Moreover, compositional zonations of garnet have been successfully modelled by taking into account the elemental sequestration during garnet growth; such modelling, with effective bulk composition, has facilitated the quantitative reconstruction of prograde *P–T* evolution of eclogites (e.g. Du et al., 2014; Gaidies et al., 2008; Konrad-Schmolke et al., 2008).

Isotopic dating, in combination with quantitative determination of *P–T* paths, has also enhanced understanding of the geodynamic evolution of eclogites, and can be used to constrain the timing and duration of high-*P* metamorphic events, and ultimately calculate the rates of subduction burial and tectonic exhumation (e.g. Kaneko et al., 2003; Liati and Gebauer, 1999). A variety of isotope systematics such as ^{40}Ar-^{39}Ar and Rb-Sr of phengite and Lu-Hf and Sm-Nd of garnet have been used for high-*P* geochronological studies (e.g. Cheng et al., 2016; Duchêne et al., 1997; Glodny et al., 2005; Lister and Forster, 2016; Ruffet et al., 1997). However, whole-rock/multi-mineral analyses are often subject to large uncertainties because of excess argon (e.g. Ruffet et al., 1997), low closure temperature of the Rb-Sr systematics of mica (Inger and Cliff, 1994) and selective dissolution of garnet and its accessory mineral inclusions (Scherer et al., 2000). In situ ion-probe U-Pb dating of zircon, particularly when its rare earth element compositions are combined, gives the most reliable time

constraints for high-*P* metamorphism (Bingen et al., 2004; Liu et al., 2006; Liu and Liou, 2011; Rubatto, 2002; Rubatto and Hermann, 2003, 2007). The U-Pb zircon ages reported from a variety of high- to ultrahigh-*P* eclogites, however, are often scattered possibly owing to analytical error, inherited component, Pb loss, geological heterogeneity, etc. (e.g. Di Vincenzo et al., 2016; Gilotti et al., 2004; Hacker et al., 1998; Liu et al., 2006; Mattinson et al., 2006; McClelland et al., 2006; Root et al., 2004; Wan et al., 2005; Zhang et al., 2010). The core-rim zonation and inclusion assemblage of zircon are important for determining the age of each zircon domain and resolving the multiplicity of metamorphic events (e.g. Engi, 2017; Liu and Liou, 2011). Therefore, the isotopic ages of eclogites should be interpreted with care by taking geological and tectonic contexts into account.

The time-scale and prograde *P–T* path of eclogite facies metamorphism are best elucidated for low- to medium-*T* eclogites affected by negligible or minor retrogression (e.g. Du et al., 2014; Groppo and Castelli, 2010; Lapen et al., 2003; Liu et al., 2006; Page et al., 2007; Tsujimori et al., 2006). A candidate for such studies in the Transantarctic Mountains, Antarctica, is the barroisite eclogite rarely reported from the Lanterman Range, northern Victoria Land (NVL) (Figure II-1; Di Vincenzo et al., 1997, 2016). In order to unravel the evolutionary history of the Lanterman Range eclogite, I used *P–T* pseudosection modelling of garnet-bearing assemblages and sensitive high-resolution ion microprobe (SHRIMP) U-Pb dating of zircon, particularly focusing on multiply zoned

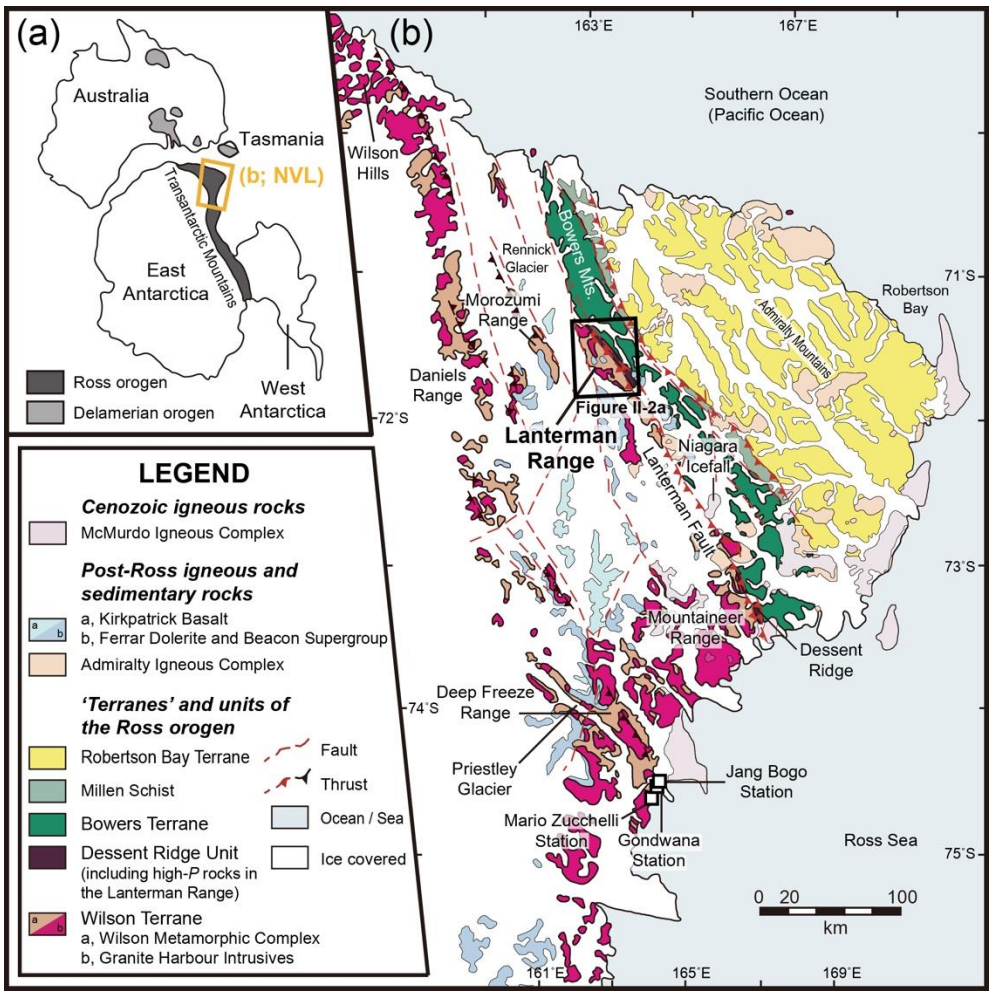

Figure II-1. (a) Schematic map showing an Antarctic–Australian segment of the Ross–Delamerian orogen prior to the breakup of Gondwana. An orange box denotes the location of northern Victoria Land (NVL) enlarged in (b). (b) Tectonic province map of NVL (modified after Läufer et al., 2011). The region in black box is enlarged in Figure II-2a. Three small boxes along the coast of the Ross Sea indicate the locations of the Jang Bogo (Republic of Korea), Gondwana (Germany), and Mario Zucchelli (Italy) stations, respectively, from north to south.

grains. The results provide new petrological perspectives on the growth history of high-*P* zircon and the subduction-exhumation process in the suture zone eclogite.

GEOLOGICAL BACKGROUND

Northern Victoria Land, situated at the Pacific end of the Transantarctic Mountains, is a part of the 4,000-km-long Ross–Delamerian orogen (Figure II-1a). This orogen represents an Antarctic–Australian segment of the Andean-type Terra Australis orogen which is a product of convergent tectonics along the paleo-Pacific continental margin, commenced at the late stage of the Gondwana formation (*c.* 570–530 Ma; for example, Boger, 2011; Cawood, 2005). NVL comprises three NW-trending, fault-bounded blocks of the Wilson, Bowers and Robertson Bay terranes from onshore to offshore, respectively, as a product of southwestward subduction-accretion event(s) (Figure II-1b; Bradshaw and Laird, 1983; GANOVEX Team, 1987; Kleinschmidt and Tessensohn, 1987). The Wilson Terrane is a continental arc primarily consisting of middle Cambrian to Early Ordovician syn- to post-orogenic plutons, the Granite Harbour Intrusives (Bomparola et al., 2007; Borg and Stump, 1987), which intrude metasedimentary rocks of the Wilson Metamorphic Complex (WMC) primarily derived from siliciclastic lithologies of a former passive margin (e.g. Boger, 2011; Estrada et al., 2016; Figure II-1b). The Bowers Terrane forms an elongate belt (~20–50 km wide) of middle to late Cambrian

volcanic-sedimentary sequences, the Sledgers, Mariner and Leap Year groups in the ascending order (Stump, 1995; Weaver et al., 1984). The Robertson Bay Terrane comprises variably folded, late Cambrian–Early Ordovician turbiditic sequences thicker than 3,000 m (Dallmeyer and Wright, 1992; Field and Findlay, 1983). The boundary between the Wilson and Bowers terranes is defined by the Lanterman Fault zone (Figure II-1b; Capponi et al., 1999); its eastern part comprises the Dessent Ridge Unit (e.g. Läufer et al., 2011) which is primarily composed of medium-*P* amphibolites and metapelites to the southeast (Kleinschmidt et al., 1984) and eclogite facies mafic-ultramafic rocks of the Lanterman Range to the northwest (Ricci et al., 1996).

The Lanterman Range occupying the central segment of the Lanterman Fault zone (Figure II-1b) is dominated by the Wilson crystalline rocks (the WMC and Granite Harbour Intrusives) together with limited occurrence of the Bowers sequences to the northeast (Figure II-2a; Roland et al., 1984; Talarico et al., 1998). Three metamorphic units are distinguished from west to east: the Edixon, Bernstein and Gateway Hills Metamorphic complexes (Talarico et al., 1998, 2004). The latter unit contains tectonic lenses of eclogite, amphibolite and meta-ultramafic rock (Di Vincenzo et al., 1997; Ricci et al., 1996). The eclogite outcrops only occur along a ridge near the Husky Pass, which has served as an obvious target for many previous studies (Figure II-2a; Capponi et al., 1997; Di Vincenzo et al., 2016; Ghiribelli et al., 2002; Palmeri et al., 2009, 2011). In

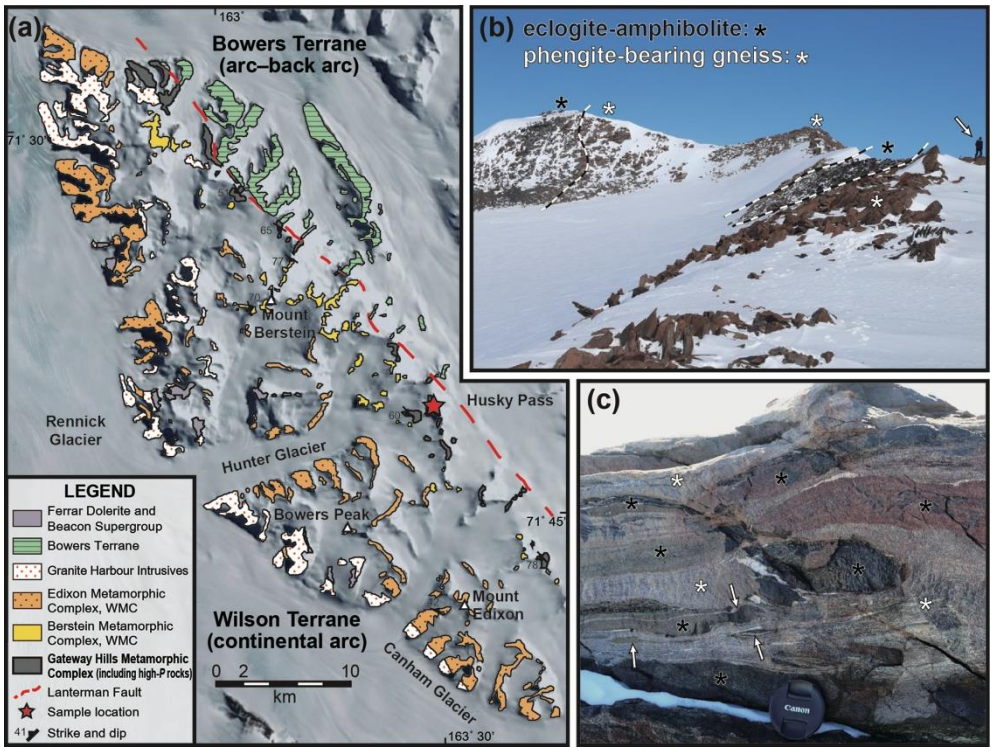

Figure II-2. (a) Geological map of the Lanterman Range, northern Victoria Land (modified after Talarico et al., 1998), shown over the Google Earth satellite image. A red star denotes the eclogite sample locality at a ridge near the Husky Pass, corresponding to the 'outcrop 4' of Capponi et al. (1997). WMC, Wilson Metamorphic Complex. (b, c) Outcrop photographs showing structural relationships among mafic boudins (black asterisk) and phengite-bearing quartzofeldspathic gneisses (white asterisk) along the ridge. (b) Alternating layers of mafic (dark gray) and quartzofeldspathic (brown) lithologies. Dashed lines denote lithologic boundaries. A geologist for scale is ~1.8 m tall (white arrow). (c) A garnet amphibolite boudin (center) enveloped by sub-horizontal intercalations of mafic and felsic gneisses or schists. Complex structures and thin intercalations (white arrows) of mafic and felsic rocks indicate pervasive ductile deformation. A lens cap for scale is ~7 cm.

addition, one garnet-bearing ultramafic rock was reported near the Mt. Berstein (Palmeri et al., 2007). The eclogite and its retrograde product, eclogitic amphibolite, are collectively named here as the Lanterman Range eclogite, and occur in the field as: elongate layers or tabular sheets alternating with (garnet–)phengite-bearing quartzofeldspathic schists and gneisses (Figure II-2b); and deformed lenses or boudins, up to tens of metres thick, enveloped by the felsic gneisses (Figure II-2c; Capponi et al., 1997; Ricci et al., 1996). Previous workers reported two distinctive types and clockwise *P*–*T*–*t* paths of the Lanterman Range eclogite: (a) 'hot' eclogites metamorphosed at ~750–850 °C but undergone the amphibolite facies retrogression (Di Vincenzo and Palmeri, 2001; Di Vincenzo et al., 1997) and (b) 'tepid' eclogites recording quartz-stable peak conditions at ~17–24 kbar and 700 °C, preceded by prograde epidote-amphibolite facies metamorphism at ~9 kbar and 600 °C (Di Vincenzo et al., 2016). The high-*P* metamorphism of 'hot' eclogites was dated at *c.* 500 Ma on the basis of Sm-Nd errorchrons; in contrast, continuous growth and recrystallization of high-*P* zircon in 'tepid' eclogites were dated at *c.* 530–500 Ma using the in situ LA-ICP-MS analyses (Di Vincenzo et al., 2016). On the basis of ^{40}Ar-^{39}Ar ages of amphibole, the cooling and exhumation rates were estimated to be >30 °C/Ma and 2–5 km/Ma respectively, during the decompressional recrystallization at the amphibolite facies conditions (Di Vincenzo et al., 2001; Di Vincenzo and Palmeri, 2001; Goodge and Dallmeyer, 1996). The amphibolite facies structural reworking has been traced throughout the

Lanterman Range, in particular the Gateway Hills Metamorphic Complex (Capponi et al., 1999; Crispini et al., 2007; Federico et al., 2010). The foliations trending NW–SE and dipping steeply to the SW and NE as well as the stretching lineations plunging to the SW are recorded in the mafic lenses and surrounding gneisses. These structural elements were produced by the west-over-east thrusting related to the subduction of paleo-Pacific plate. Finally, sinistral strike-slip deformation took place at the greenschist facies conditions during the late stage of the Ross orogeny.

SAMPLE DESCRIPTION AND PETROGRAPHY

The mafic lenses in the Lanterman Range are dominated by amphibolite facies assemblages rich in calcic amphibole and epidote together with titanite–ilmenite replacing rutile and kelyphitic/symplectitic armour around garnet and omphacite. Thus, the Lanterman Range eclogites are mostly eclogitic amphibolites or retrogressed eclogites, whereas the eclogites *sensu stricto* containing more than 75 vol.% of garnet and omphacite with negligible to minor retrogression (Desmons and Smulikowski, 2007) are volumetrically small. In addition, amphibolites with no vestige of eclogitic precursor uncommonly occur and their microstructures such as thin films of interstitial quartz indicate the presence of former melts (e.g. Sawyer, 2008).

Approximately 70 meta-mafic rocks including ~20 eclogites, ~30 retrogressed eclogites and ~20 amphibolites were collected from the Husky

Pass, Lanterman Range (Figure II-2a). Over 100 thin sections were made for petrographic investigation; when a lineation is present, the XZ section, perpendicular to the foliation and subparallel to the lineation, was used. Samples were mostly collected from the northern part of 'outcrop 4' in the geological map of Capponi et al. (1997), where Di Vincenzo et al. (2016) reported the 'tepid' eclogite. This site is situated several hundred metres northward from the 'hot' eclogite locality (Di Vincenzo et al., 1997). In this study, I concentrated on two pristine eclogite samples (E-1a and E-1c) in order to delineate prograde *P*–*T* evolution of eclogites, precluding any retrogression effect on the compositions of high-*P* minerals. Mineral abbreviations are after Whitney and Evans (2010).

The analysed eclogites are medium-grained and moderately foliated, showing poorly defined lineation. Mineral assemblages are represented by garnet + omphacite + amphibole + epidote + rutile, together with minor amounts of phengite and quartz. The foliation is defined by aligned aggregates of prismatic omphacite, elongate rutile and amphibole, as well as compositional layers either rich or poor in near-equidimensional garnet porphyroblasts (Figure II-3a). Three types of garnet porphyroblasts are identified on the basis of the size, morphology and mineral inclusions. The first type of garnet porphyroblasts (Grt I) is euhedral to subhedral, and up to 1 mm (on average ~700 μm) in the longest dimension; it is often typified by inclusion-rich inner part in contrast to inclusion-poor outer segment (Figure II-3a,b). The inner part shows a yellow tinge to the naked eye, and contains

Figure II-3. Photomicrographs (a, b, e, f) and backscattered electron images (c, d) of the barroisite eclogites showing mineral parageneses and inclusion in garnet porphyroblasts (Grt I and Grt II). Photomicrographs were taken under plane-polarized light. (a) An eclogite sample E-1a, mainly consisting of garnet, omphacite, barroisite, epidote, and rutile. The Ca X-ray maps for two Grt I and one atoll-shaped Grt II porphyroblasts are shown with intensity colors. Dark domains mostly consist of rutile and diopside–oligoclase symplectite (sym). A dashed box is enlarged in Figure II-4a and a white box in (e). (b) Sigmoidal trails of quartz and/or rutile inclusions (Qz–Rt) in the inner domain of the Grt I (sample E-1c). Fine-grained Grt III is slightly elongated (top left). Small white boxes are enlarged in (c) and (d), respectively. (c) Inclusions of omphacite and allanite partly mantled by barroisite and epidote, respectively, in the inner domain of Grt I (sample E-1a). Other inclusion phases include Mg-pargasite, rutile, and zircon. (d) Multi-phase inclusions in the inner domain of Grt I, consisting of paragonite, quartz, and titanite–rutile together with minor Mg-pargasite (sample E-1c). (e) Atoll-shaped Grt II enclosing omphacite, amphibole, epidote, quartz, and rutile (sample E-1a). (f) Poikiloblastic barroisite containing eclogitic minerals such as garnet and omphacite (sample E-1a). Mineral abbreviations in Figures II-3–II-10, II-12 and II-13 and Table II-3 are after Whitney and Evans (2010).

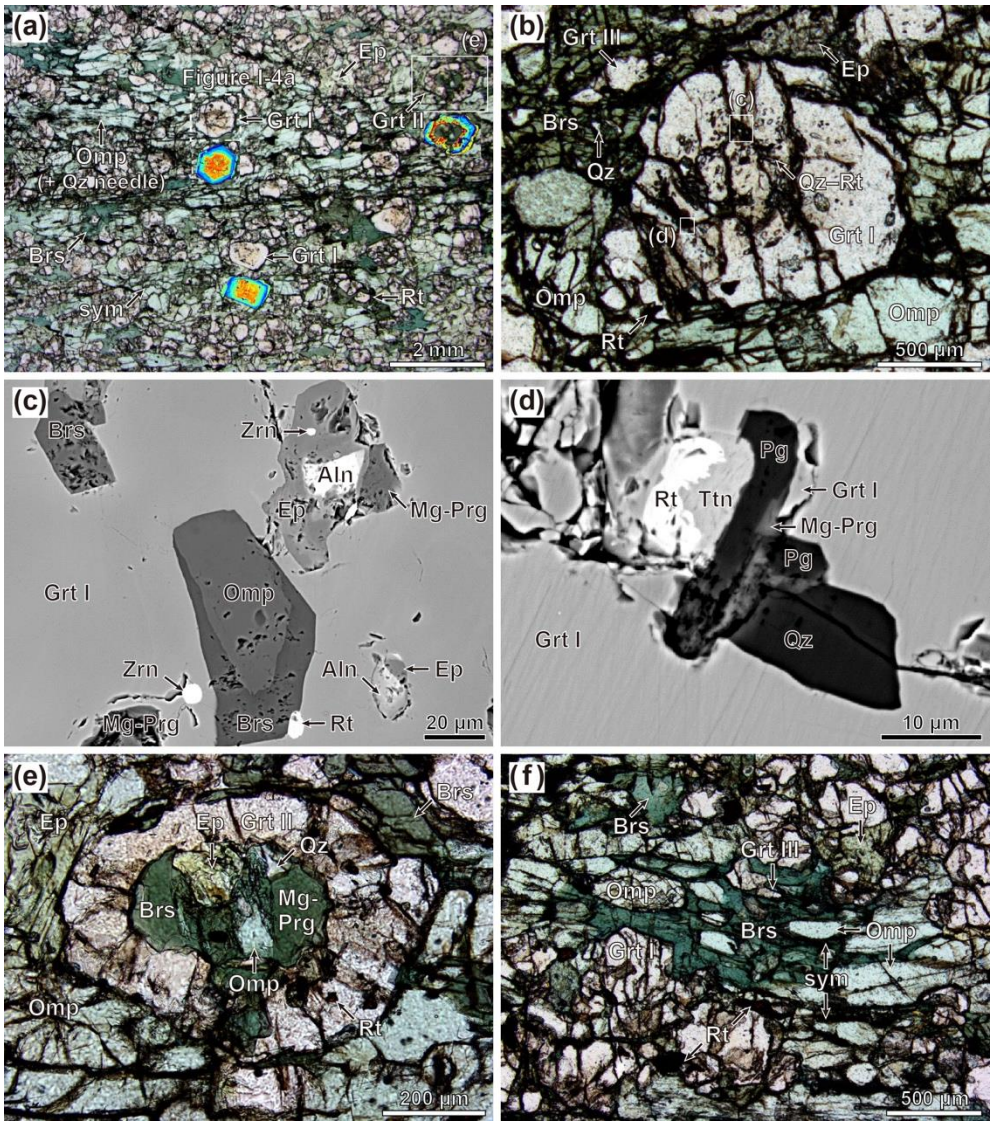
(a)
Ep
(e)
Figure I-4a
Grt I
Grt II
Omp
(+ Qz needle)
Brs
Grt I
sym
Rt
2 mm
(b)
Grt III
Ep
(c)
Brs
Qz
Qz–Rt
(d)
Grt I
Omp
Rt
Omp
500 μm
(c)
Brs
Zrn
Aln
Ep
Mg-Prg
Grt I
Omp
Zrn
Aln
Ep
Mg-Prg
Brs
Rt
20 μm
(d)
Pg
Rt
Ttn
Grt I
Mg-Prg
Pg
Grt I
Qz
10 μm
(e)
Ep
Brs
Ep
Grt III
Qz
Brs
Mg-
Prg
Omp
Omp
Rt
200 μm
(f)
Brs
Ep
Grt III
Omp
Brs
Omp
Grt II
sym
Rt
500 μm

a variety of inclusions such as omphacite + amphibole + epidote + paragonite + rutile + quartz ± titanite (Figure II-3a–d), together with relict albite. Quartz and/or rutile inclusions in the inner part of Grt I occasionally define weak sigmoidal trails (Figure II-3b). The outer segment of Grt I contains a relatively small number of inclusions such as omphacite, amphibole, phengite and rutile (Figures II-3a,b and II-4a). Atoll-shaped garnet porphyroblasts (Grt II) enclose similar mineral inclusions as the Grt I (Figures II-3e and II-4b). Fine-grained hypidio- to xenoblastic garnet porphyroblasts (Grt III, mostly <300 μm) are commonly elongated in shape with their long dimension subparallel to the foliation (Figure II-3b,f).

Euhedral to subhedral prismatic grains of omphacite often contain mineral inclusions such as needle-shaped quartz (Figure II-3a), which are responsible for the cloudy appearance of the inner domains. Fine-grained symplectites of diopside and plagioclase develop along the grain boundary of omphacite (Figure II-3a,f). Amphibole in the matrix is subdivided into two types: idio- to hypidioblasts in contact with garnet and omphacite (Figure II-3e); and skeletal xenoblasts, commonly intergrown with quartz, enclosing a variety of minerals such as garnet, omphacite, rutile and quartz (Figure II-3f). Subhedral to anhedral grains of epidote are common in the matrix (Figure II-3a). Phengite and paragonite as well as accessory minerals, such as zircon, allanite and apatite, occur in the inner parts of the Grt I and Grt II (Figure II-3c), but are virtually absent in the matrix except for zircon.

Figure II-4. X-ray maps (a, b) and compositional profiles (c, d) of garnet porphyroblasts (Grt I and II). Two outermost sub-domains or annuli are notable for the Grt II in (b) (sample E-1c), compared to single domain for the Grt I in (a) (sample E-1a); white arrows in the Ca map denote the outer sub-domain with high grossular contents. Compositional boundaries between the inclusion-rich inner and -poor outer parts are traced in (a, b). Minerals with low X-ray counts or higher than the maximum counts are shown in black for clarity; e.g. clinopyroxene and epidote in the Ca X-ray maps of (a, b). See text for further details.

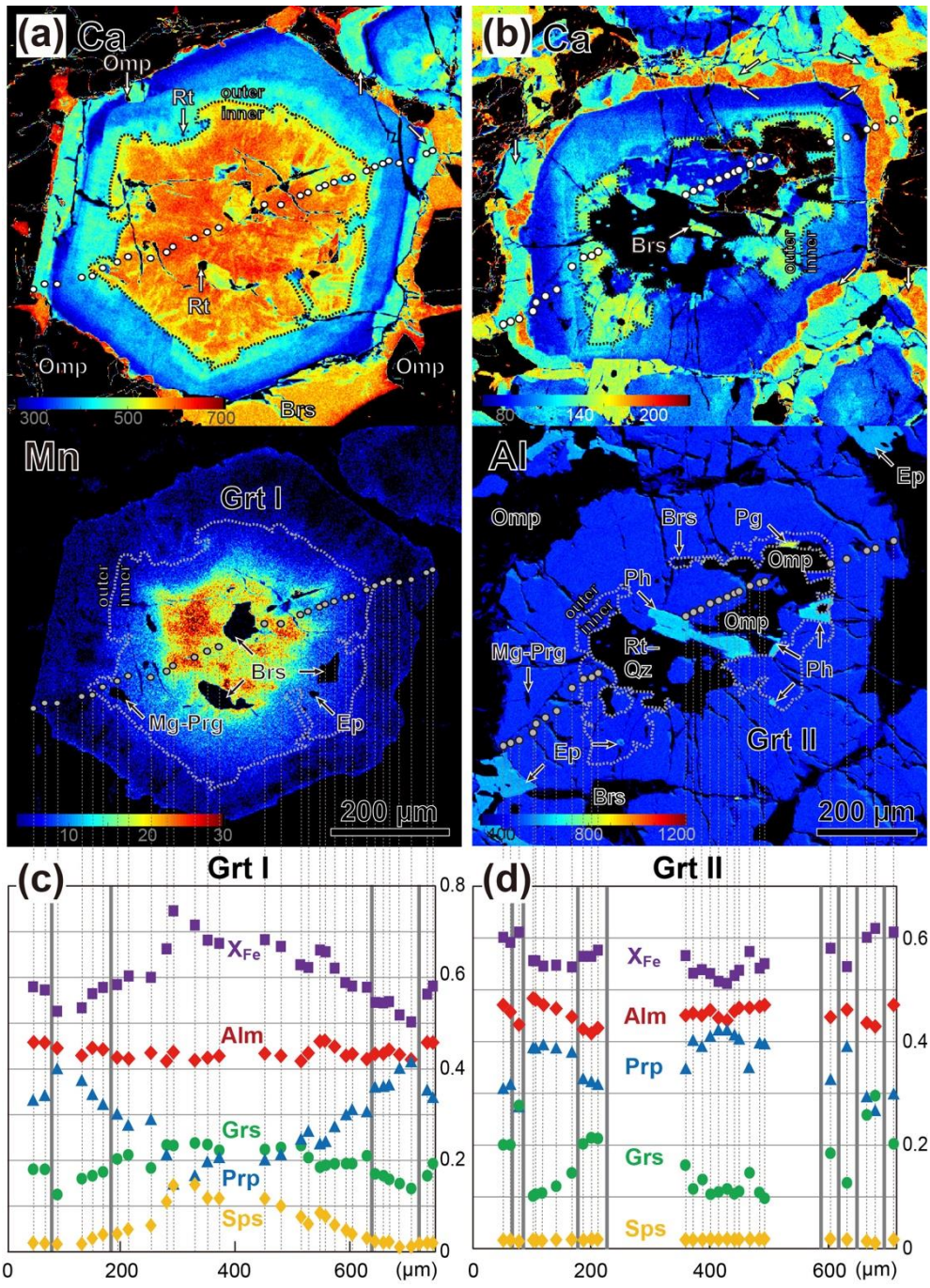
(a) Ca
Omp
Rt
outer
inner
Rt
Omp
Omp
300
500
700
Brs
(b) Ca
Brs
outer
inner
80
140
200
Mn
Grt I
outer
inner
Brs
Mg-Prg
Ep
10
20
30
200 μm
Al
Ep
Omp
Brs
Pg
Omp
Ph
outer
inner
Omp
Mg-Prg
Rt–
Qz
Ph
Ep
Grt II
Brs
400
800
1200
200 μm
(c)
Grt I
XFe
Alm
Grs
Prp
Sps
0
0.2
0.4
0.6
0.8
0
200
400
600
(μm)
(d)
Grt II
XFe
Alm
Prp
Grs
Sps
0
0.2
0.4
0.6
0
200
400
600
(μm)

ANALYTICAL METHODS

Mineral compositions were analysed using a JEOL JXA-8530F field-emission electron microprobe housed at the Korea Polar Research Institute, with 15 kV accelerating voltage, 10 nA beam current, 5 μm beam diameter and 20 s counting times. The concentrations of Zr-in-rutile were measured following the analytical conditions of Zack et al. (2002, 2004), and the calculated detection limit for Zr was ~8 ppm (Table II-1). The rutile analyses with Si >200 ppm were discarded because of a possible excitation of adjacent silicate phases (Zack et al., 2004). Standard materials used for the calibration include natural silicates and synthetic oxides (Table II-1). Data acquisition and reduction were performed using the ZAF matrix correction. The X-ray mapping of garnet was conducted with 15 kV accelerating voltage, 500 nA beam current, 50 ms dwell time per pixel, 3 μm step size and focused beam. Whole-rock compositions of eclogites used for the pseudosection modelling were determined by the inductively-coupled plasma optical emission spectroscopy at the Actlabs, Ontario, Canada, employing a lithium metaborate/tetraborate fusion.

Zircon separates were collected from a barroisite eclogite (sample E-1a), using the heavy-liquid technique of Cheong et al. (2013), and were mounted in epoxy disc with SL13 and FC-1 standard zircon crystals. The former was use for measuring the U concentration (238 ppm; Claoué-Long et al., 1995), and the latter for calibrating $^{206}Pb/^{238}U$ ratios ($^{206}Pb^{*}/^{238}U$ = 0.1859; Paces and Miller, 1993). The cathodoluminescence (CL) images of

zircon crystals were obtained using a JEOL JSM-6610LV scanning electron microscope (SEM) housed at the Korea Basic Science Institute (KBSI). Using the energy dispersive spectroscopy system attached to the SEM, mineral inclusions inside zircon were also identified. The U-Th-Pb isotopic compositions of zircon were measured using the KBSI SHRIMP-IIe. The analytical protocol followed that of Williams (1998). All isotopes were measured using a primary O_2^- beam with ~3–5 nA and ~25 μm diameter spot. Common Pb contributions to total Pb counts were corrected using the 207 Pb correction method based on the Pb/U concordance and model common Pb composition (Cumming and Richards, 1975; Williams, 1998). The isotopic data were reduced using the Prawn/Lead 6.5.5 software (written communication, T. Ireland, 1996), and were plotted using the program Isoplot/Ex (Ludwig, 2008).

MINERAL CHEMISTRY

Garnet, clinopyroxene, sodic-calcic/calcic amphibole, phengite, epidote, paragonite and rutile in two eclogite samples (E-1a and E-1c) were analysed in order to determine their equilibrium compositions at each metamorphic stage. For rutile, Zr contents are of primary interest for the thermometric calculation. Nomenclatures of clinopyroxene and amphibole are after Morimoto et al. (1988) and Leake et al. (1997) respectively. Representative analyses of minerals, except for those of rutile (Table II-2), are given in Table II-3.

Table II-1. Analytical conditions of the electron probe microanalysis for rutile.

Element	X-ray	Crystal	Standard	Peak counting time (s)	Background counting time (s)	Detection limit (ppm)
Si	$K\alpha_1$	TAP	Quartz	150	75	13
Fe	$K\alpha_1$	LIF	Hematite	150	75	10
Cr	$K\alpha_1$	LIF	Cr_2O_3	150	75	11
V	$K\alpha_1$	LIF	$Ca_3(VO_4)_2$	150	75	17
Ti	$K\alpha_1$	PETH	TiO_2	20	10	16
Nb	$L\alpha_1$	PETH	$KNbO_3$	300	150	8
Zr	$L\alpha_1$	PETH	$(Zr, Y)O_2$	300	150	8

Garnet

The majority of garnet porphyroblasts in the eclogite samples preserve prominent compositional zonation (Figure II-4). The Grt I preserves a bell-shaped Mn profile (Sps = Mn/(Fe^{2+} + Mg + Ca + Mn) = 0.03–0.16) that broadly compensates the corresponding Mg trough (Prp = Mg/(Fe^{2+} + Mg + Ca + Mn) = 0.11–0.33; Figure II-4a,c). The rest of garnet porphyroblasts are relatively depleted in Mn (Sps <0.05). The inner domain of Grt I with the Mn plateau is relatively rich in Ca (Grs = Ca/(Fe^{2+} + Mg + Ca + Mn) = 0.17–0.25), whereas the outer segment is characterized by a monotonous increase in Mg (Prp = 0.27–0.40) but a decrease in Ca (Grs = 0.18–0.08) towards the margin (Figures II-4 and II-5a). The X_{Fe} values (= Fe^{2+}/(Fe^{2+} + Mg) = 0.56–0.85) of the Grt I widely vary but generally decrease outward (Figures II-4c and II-5a). Compositional variations of the Grt II are similar to those of the Grt I, except for the lack of compositions equivalent to the Mn-rich inner domain of the Grt I (Figure II-4b,d). On the other hand, fine-grained Grt III contains the inner domain (Prp = 0.30–0.41; Grs = 0.09–0.17; X_{Fe} = 0.51–0.64) compositionally comparable to the outer segment of the Grt I (Figure II-4a). The Ca-Kα X-ray map shows that the mantle and rim of garnet are characterized by two outermost sub-domains with rebounding Ca contents (Figure II-4a,b). An abrupt Ca increase is conspicuous in the inner sub-domain of the Grt I and Grt II (Prp = 0.27–0.29, Grs = 0.26–0.30 and X_{Fe} = 0.60–0.62; Figure II-4b). The outermost sub-domains are present in all types of garnet porphyroblasts, and are typified by

Table II-2. Representative analyses of rutile and the Zr-in-rutile temperatures.

Grain no.	SiO_2	FeO	Cr_2O_3	V_2O_3	TiO_2	Nb_2O_5	ZrO_2	Total	Si (ppm)	Zr (ppm)	Input P (kbar)	Output T (°C)	Petrographic domain
Sample E-1a													
Rt (Grt5)	0.04	0.74	0.11	0.43	98.61	0.06	0.03	100.01	187	192	23.5	671	Incl in Grt
Rt lr	0.02	0.65	0.28	0.56	98.28	0.08	0.02	99.89	112	178	23.5	665	Matrix
Rt 2-1	b.d.	0.41	0.24	0.68	98.90	0.11	0.03	100.37	-	192	23.5	671	Matrix
Rt 2-2	b.d.	0.34	0.23	0.66	98.92	0.11	0.02	100.29	-	178	23.5	665	Matrix
Rt 2-3	b.d.	0.38	0.24	0.67	98.85	0.11	0.03	100.28	-	185	23.5	668	Matrix
Rt 2-4	b.d.	0.42	0.24	0.68	98.82	0.10	0.03	100.29	-	200	23.5	674	Matrix
Rt 2-5	b.d.	0.44	0.23	0.68	98.80	0.10	0.03	100.27	-	185	23.5	668	Matrix
Rt 2-7	b.d.	0.49	0.22	0.67	98.64	0.12	0.02	100.16	-	170	23.5	662	Incl in Grt
Rt 3-2	b.d.	0.44	0.27	0.59	98.81	0.21	0.03	100.34	-	200	23.5	674	Incl in Omp
Rt 3-3	b.d.	0.52	0.27	0.59	98.74	0.12	0.03	100.27	-	215	23.5	680	Incl in Omp
Rt 3-4	b.d.	0.49	0.27	0.61	98.72	0.15	0.03	100.26	-	200	23.5	674	Incl in Grt
Rt 3-5	b.d.	0.00	0.27	0.60	98.73	0.23	0.02	99.85	-	163	23.5	658	Incl in Grt
Rt 3-6	b.d.	0.51	0.27	0.00	98.75	0.26	0.02	99.81	-	163	23.5	658	Incl in Grt
Rt 3-8	b.d.	0.44	0.25	0.00	98.95	0.11	0.03	99.78	-	192	23.5	671	Incl in Grt
Rt 3-9	b.d.	0.54	0.25	0.58	98.78	0.20	0.02	100.38	-	178	23.5	665	Incl in Grt
Rt 3-10	b.d.	0.53	0.00	0.59	98.88	0.10	0.03	100.12	-	185	23.5	668	Incl in Grt
Rt 3-11	b.d.	0.45	0.25	0.60	98.83	0.13	0.02	100.28	-	163	23.5	658	Incl in Omp

Rt 3-12	b.d.	0.00	0.25	0.61	98.71	0.13	0.02	99.72	-	178	23.5	665	Incl in Omp
Rt 3-13	b.d.	0.40	0.25	0.61	98.78	0.26	0.02	100.32	-	170	23.5	662	Incl in Omp
Rt 3-14	0.01	0.42	0.25	0.60	98.75	0.11	0.03	100.18	47	185	23.5	668	Incl in Omp
Rt 3-16	b.d.	0.52	0.26	0.61	98.70	0.13	0.02	100.24	-	155	23.5	655	Incl in Omp
Sample E-1c													
Rt t1	b.d.	0.44	0.20	0.65	98.61	0.11	0.03	100.04	-	215	23.5	680	Matrix
Rt t2	b.d.	0.44	0.19	0.65	98.61	0.11	0.03	100.03	-	215	23.5	680	Matrix
Rt 1-1	b.d.	0.48	0.20	0.67	98.57	0.07	0.03	100.01	-	207	23.5	677	Incl in Grt
Rt 1-2	b.d.	0.44	0.20	0.00	98.53	0.09	0.03	99.28	-	185	23.5	668	Incl in Grt
Rt 1-3	b.d.	0.38	0.20	0.65	98.61	0.10	0.03	99.96	-	185	23.5	668	Incl in Grt
Rt 1-4	b.d.	0.46	0.20	0.67	98.61	0.11	0.03	100.09	-	230	23.5	685	Incl in Omp
Rt 1-5	b.d.	0.39	0.20	0.66	98.55	0.12	0.03	99.95	-	207	23.5	677	Incl in Omp
Rt 1-6	0.01	0.45	0.21	0.66	98.42	0.14	0.03	99.92	51	185	23.5	668	Incl in Omp
Rt 1-7	0.01	0.42	0.22	0.65	98.65	0.13	0.02	100.10	28	178	23.5	665	Incl in Omp
Rt 1-8	b.d.	0.49	0.22	0.64	98.61	0.11	0.03	100.10	-	192	23.5	671	Incl in Omp
Rt (Grt1)	0.04	0.91	0.14	0.49	98.02	0.10	0.02	99.72	164	178	23.5	665	Incl in Grt
Rt (Amp 2)	b.d.	0.43	0.34	0.59	98.79	0.10	0.03	100.28	-	207	23.5	677	Incl in Brs
Rt (Amp 3)	0.02	0.67	0.23	0.50	98.52	0.09	0.03	100.05	89	215	23.5	680	Incl in Brs
Rt Grt3	0.01	0.51	0.34	0.47	98.56	0.08	0.02	99.99	37	155	23.5	655	Matrix
Rt Grtat1	0.02	0.54	0.14	0.52	98.70	0.10	0.03	100.05	103	200	23.5	674	Matrix

Rt Omp1	0.02	0.70	0.25	0.50	98.30	0.12	0.02	99.91	108	155	23.5	655	Matrix
Rt Grt7	0.01	0.59	0.13	0.57	98.01	0.14	0.02	99.48	61	155	23.5	655	Matrix
Rt (Grt7)	0.03	0.93	0.18	0.66	98.39	0.12	0.03	100.33	117	185	23.5	668	Incl in Grt
Rt bl1	b.d.	0.49	0.18	0.65	98.57	0.18	0.03	100.09	-	200	23.5	674	Matrix
Rt t3	b.d.	0.41	0.26	0.54	98.86	0.11	0.02	100.20	-	170	23.5	662	Matrix
Rt (GrtRF)	0.03	0.34	0.33	0.61	99.23	0.09	0.03	100.66	154	192	23.5	671	Incl in Grt

b.d., below detection limit ; Incl, inclusion.

Table II-3. Representative analyses of minerals in barroisite eclogites.

mineral	Garnet										
sample	E-1a										
	Grt I id		Grt I od		Grt II od	Grt III id	Grt I isd	Grt II isd	Grt I osd	Grt II osd	Grt III osd
SiO_2	38.04	38.04	39.02	39.03	39.33	40.02	39.11	39.34	39.05	39.22	39.47
TiO_2	0.15	0.13	0.08	0.05	0.01	0.03	0.16	0.06	0.04	b.d.	0.01
Al_2O_3	21.40	21.42	22.09	22.15	22.29	22.59	22.19	22.22	21.97	22.18	22.39
Cr_2O_3	0.07	0.11	0.05	b.d.	0.04	0.10	0.09	0.06	0.08	0.04	0.01
FeO*	19.66	23.84	23.66	25.15	23.97	20.15	20.08	20.40	21.40	22.31	20.28
MnO	7.39	5.85	1.99	0.69	0.87	0.13	0.63	0.65	0.74	0.92	0.75
MgO	3.80	2.84	7.11	9.53	9.35	10.99	6.98	7.70	8.48	8.97	9.45
CaO	8.95	8.48	6.37	2.76	4.54	6.33	10.60	9.57	7.44	5.78	7.33
Na_2O	b.d.	b.d.	b.d.	0.04	0.03	0.02	0.03	0.04	b.d.	b.d.	0.02
K_2O	0.02	b.d.	b.d.	b.d.	b.d.	b.d.	b.d.	0.02	b.d.	0.02	b.d
Total	99.49	100.72	100.38	99.40	100.43	100.35	99.86	100.08	99.20	99.45	99.72
Cations per 12 oxygens											
Si	3.00	2.99	3.00	3.00	2.99	3.00	2.99	3.00	3.00	3.00	3.00
Al	1.99	1.99	2.00	2.01	2.00	1.99	2.00	1.99	1.99	2.00	2.00
Cr	0.00	0.01	0.00	b.d.	0.00	0.01	0.01	0.00	0.00	0.00	0.00

Ti	0.01	0.01	0.00	0.00	0.00	0.00	0.01	0.00	0.00	b.d.	0.00
Fe^{2+}	1.30	1.57	1.52	1.62	1.52	1.26	1.28	1.30	1.37	1.43	1.29
Mn	0.49	0.39	0.13	0.04	0.06	0.01	0.04	0.04	0.05	0.06	0.05
Mg	0.45	0.33	0.81	1.09	1.06	1.23	0.80	0.87	0.97	1.02	1.07
Ca	0.76	0.71	0.52	0.23	0.37	0.51	0.87	0.78	0.61	0.47	0.60
Na	b.d.	b.d.	b.d.	0.01	0.00	0.00	0.01	0.01	b.d.	b.d.	0.00
K	0.00	b.d.	b.d.	b.d.	b.d.	b.d.	b.d.	0.00	b.d.	0.00	b.d.
Total	8.00	8.00	8.00	8.00	8.00	8.00	8.00	8.00	8.00	8.00	8.00
X_{Fe}	0.74	0.82	0.65	0.60	0.59	0.51	0.62	0.60	0.59	0.58	0.55
Alm	0.43	0.52	0.51	0.54	0.51	0.42	0.43	0.43	0.46	0.48	0.43
Prp	0.15	0.11	0.27	0.37	0.35	0.41	0.27	0.29	0.32	0.34	0.36
Grs	0.25	0.24	0.18	0.08	0.12	0.17	0.29	0.26	0.20	0.16	0.20
Sps	0.16	0.13	0.04	0.02	0.02	0.00	0.01	0.01	0.02	0.02	0.02

Table II-3. Continued.

mineral	Garnet										
sample	E-1c										
	Grt I id		Grt I od		Grt II od	Grt III id	Grt I isd	Grt II isd	Grt I osd	Grt II osd	Grt III osd
SiO_2	38.86	38.10	39.41	39.48	39.03	39.20	39.17	39.16	39.57	39.64	39.27
TiO_2	0.15	0.05	b.d.	0.04	b.d.	b.d.	0.08	0.12	b.d.	0.01	0.01
Al_2O_3	22.04	21.45	22.33	22.36	22.09	22.09	22.05	22.02	22.37	22.43	22.21
Cr_2O_3	0.07	0.09	0.05	0.01	0.02	0.08	0.09	0.10	0.08	0.05	0.01
FeO*	19.87	30.16	23.80	21.58	25.44	25.51	19.93	20.08	21.96	21.30	20.90
MnO	3.18	1.81	0.24	0.83	1.34	2.68	0.47	0.61	0.69	0.66	0.70
MgO	8.67	3.09	10.67	9.20	7.73	7.89	7.04	7.32	8.48	9.04	8.94
CaO	6.47	6.12	3.97	6.66	4.67	3.40	10.84	10.22	7.31	7.41	7.44
Na_2O	b.d.	b.d.	b.d.	b.d.	0.03	b.d.	0.03	0.02	b.d.	b.d.	0.03
K_2O	0.02	b.d.	0.02	b.d.	b.d.	b.d.	0.02	b.d.	b.d.	b.d.	b.d.
Total	99.34	100.88	100.55	100.16	100.35	100.86	99.73	99.67	100.46	100.55	99.51
Cations per 12 oxygens											
Si	2.99	3.00	2.98	3.00	3.00	3.00	3.00	3.00	3.00	3.00	3.00
Al	2.00	1.99	1.99	2.00	2.00	2.00	1.99	1.99	2.00	2.00	2.00
Cr	0.00	0.01	0.00	0.00	0.00	0.00	0.01	0.01	0.00	0.00	0.00

Ti	0.01	0.00	b.d.	0.00	b.d.	b.d.	0.00	0.01	b.d.	0.00	0.00
Fe^{2+}	1.28	1.99	1.51	1.37	1.64	1.64	1.28	1.29	1.39	1.35	1.33
Mn	0.21	0.12	0.02	0.05	0.09	0.17	0.03	0.04	0.04	0.04	0.05
Mg	0.99	0.36	1.20	1.04	0.89	0.90	0.80	0.84	0.96	1.02	1.02
Ca	0.53	0.52	0.32	0.54	0.38	0.28	0.89	0.84	0.59	0.60	0.61
Na	b.d.	b.d.	b.d.	b.d.	0.01	b.d.	0.00	0.00	b.d.	b.d.	0.00
K	0.00	b.d.	0.00	b.d.	b.d.	b.d.	0.00	b.d.	b.d.	b.d.	b.d.
Total	8.01	7.99	8.02	8.00	8.00	8.00	8.00	8.00	8.00	8.00	8.01
X_{Fe}	0.56	0.85	0.56	0.57	0.65	0.64	0.61	0.61	0.59	0.57	0.57
Alm	0.42	0.67	0.49	0.46	0.55	0.55	0.43	0.43	0.47	0.45	0.44
Prp	0.33	0.12	0.40	0.35	0.30	0.30	0.27	0.28	0.32	0.34	0.34
Grs	0.18	0.17	0.11	0.18	0.13	0.09	0.30	0.28	0.20	0.20	0.20
Sps	0.07	0.04	0.01	0.02	0.03	0.06	0.01	0.01	0.01	0.01	0.02

*Total Fe as FeO.

b.d., below detection limit; id, inner domain; od, outer domain; isd, inner sub-domain, osd, outermost sub-domain; $X_{Fe} = Fe^{2+}/(Fe^{2+} + Mg)$; Alm = Fe^{2+}/M, Prp = Mg/M, Grs = Ca/M, and Sps = Mn/M, where M = (Fe^{2+} + Mg + Ca + Mn).

Table II-3. Continued.

mineral	Omphacite													
sample	E-1a							E-1c						
	id	od		incl. (Grt I id)	incl. (Grt I od)	incl. (Grt I osd)	symplec -tite	id	od		incl. (Grt I id)	incl. (Grt I od)	incl. (Grt I osd)	symplec-tite
SiO_2	54.89	55.22	55.37	54.51	55.43	55.49	54.53	54.93	55.56	55.08	54.55	55.14	54.98	54.59
TiO_2	0.08	0.11	0.18	0.23	0.09	0.10	0.14	0.05	0.06	0.06	0.04	0.11	0.07	0.10
Al_2O_3	8.35	8.78	7.89	6.68	8.22	8.16	4.71	8.29	8.58	8.32	7.69	7.95	7.99	2.01
Cr_2O_3	0.08	0.04	b.d.	0.26	0.16	0.05	0.16	0.09	0.04	0.05	0.14	0.19	0.10	0.20
FeO*	5.83	4.92	6.28	6.60	5.91	5.86	7.96	6.33	5.32	5.87	6.27	6.48	7.10	7.39
MnO	0.04	0.00	0.03	0.10	0.04	0.04	0.06	0.08	0.06	0.04	0.06	0.06	0.12	0.04
MgO	9.77	9.74	9.72	10.12	9.66	9.91	11.14	9.52	9.70	9.92	9.68	9.52	9.34	13.19
CaO	15.50	15.51	15.34	16.14	15.08	15.25	18.41	15.01	15.13	15.49	15.27	15.09	14.68	20.91
Na_2O	5.17	5.14	5.06	4.74	5.23	5.09	3.01	5.05	5.33	5.13	4.94	5.18	5.00	1.91
K_2O	b.d.	b.d.	0.02	b.d.	b.d.	b.d.	b.d.	b.d.	b.d.	b.d.	0.03	b.d.	b.d.	b.d.
Total	99.70	99.47	99.88	99.39	99.81	99.96	100.11	99.33	99.80	99.96	98.67	99.72	99.40	100.34
Cations per 6 oxygens														
Si	1.99	1.99	2.00	1.99	2.00	2.00	2.00	1.99	2.00	1.99	2.00	2.00	2.00	2.01
Al	0.36	0.37	0.34	0.28	0.35	0.34	0.20	0.35	0.36	0.35	0.33	0.34	0.34	0.09

Cr	0.00	0.00	b.d.	0.01	0.00	0.00	0.00	0.00	0.00	0.00	0.00	0.01	0.00	0.01
Ti	0.00	0.00	0.00	0.01	0.00	0.00	0.00	0.00	0.00	0.00	0.00	0.00	0.00	0.00
Fe^{3+}	0.02	0.00	0.02	0.05	0.01	0.01	0.01	0.00	0.01	0.02	0.02	0.02	0.01	0.04
Fe^{2+}	0.16	0.15	0.17	0.15	0.17	0.17	0.24	0.19	0.15	0.16	0.18	0.18	0.21	0.18
Mn	0.00	0.00	0.00	0.00	0.00	0.00	0.00	0.00	0.00	0.00	0.00	0.00	0.00	0.00
Mg	0.53	0.52	0.52	0.55	0.52	0.53	0.61	0.52	0.52	0.53	0.53	0.51	0.51	0.72
Ca	0.60	0.60	0.59	0.63	0.58	0.59	0.72	0.58	0.58	0.60	0.60	0.59	0.57	0.82
Na	0.36	0.36	0.35	0.34	0.37	0.36	0.21	0.36	0.37	0.36	0.35	0.36	0.35	0.14
K	b.d.	b.d.	0.00	b.d.	b.d.	b.d.	b.d.	b.d.	b.d.	b.d.	0.00	b.d.	b.d.	b.d.
Total	4.01	4.00	4.00	4.01	4.00	4.00	4.00	4.00	4.00	4.01	4.01	4.01	4.00	4.01
X_{Fe}	0.23	0.22	0.25	0.22	0.24	0.24	0.28	0.27	0.23	0.23	0.25	0.25	0.29	0.20
Jd	0.34	0.36	0.34	0.28	0.35	0.34	0.20	0.35	0.36	0.34	0.33	0.34	0.34	0.09
Aeg	0.02	0.00	0.02	0.05	0.01	0.01	0.01	0.00	0.01	0.02	0.02	0.02	0.01	0.04

*Total Fe as FeO. Fe^{3+} contents were calculated as Fe^{3+} = Na – Al – Cr.
b.d., below detection limit; id, inner domain; od, outer domain; osd, outermost sub-domain; incl., inclusion; $X_{Fe} = Fe^{2+}/(Fe^{2+} + Mg)$; Jd = Na – Fe^{3+} – Cr; Aeg = Fe^{3+}.

Table II-3. Continued.

mineral	Amphibole											
sample	E-1a						E-1c					
	incl. (Grt I id)	incl. (Grt I od)	incl. (Grt I isd)	matrix porphyroblast			incl. (Grt I id)	incl. (Grt I od)		incl. (Grt I osd)	matrix porphyroblast	
SiO_2	39.31	49.93	45.49	49.89	49.16	47.59	40.04	48.81	48.38	43.96	48.86	50.53
TiO_2	1.03	0.26	0.17	0.22	0.27	0.25	0.37	0.27	0.27	b.d.	0.29	0.11
Al_2O_3	20.28	12.82	15.39	10.23	11.05	12.20	19.50	12.12	12.57	16.64	11.43	9.47
Cr_2O_3	0.11	0.11	0.07	0.11	0.08	0.12	0.02	0.23	0.03	0.04	0.15	0.15
FeO*	12.78	6.06	9.28	9.07	10.02	10.94	14.94	7.41	9.66	11.14	10.69	8.17
MnO	0.20	0.07	0.07	0.07	0.08	0.09	0.27	0.10	0.06	0.08	0.09	0.04
MgO	10.21	16.62	14.12	15.35	14.47	13.50	9.32	16.13	14.80	12.37	14.03	16.31
CaO	9.43	9.15	9.81	9.07	8.88	8.88	8.26	9.17	8.71	9.71	9.12	9.23
Na_2O	4.05	3.24	3.39	3.15	3.31	3.48	4.41	3.11	3.27	3.65	3.24	3.19
K_2O	b.d.	0.34	0.01	0.41	0.40	0.17	b.d.	0.43	0.06	b.d.	0.31	0.49
Total	97.39	98.59	97.80	97.57	97.73	97.23	97.12	97.77	97.82	97.59	98.21	97.72
Cations per 23 oxygens												
Si	5.74	6.87	6.44	7.04	6.96	6.81	5.90	6.82	6.79	6.30	6.91	7.10
Al^{IV}	2.26	1.13	1.56	0.96	1.04	1.19	2.10	1.18	1.21	1.70	1.09	0.90
Al^{VI}	1.23	0.94	1.00	0.74	0.80	0.86	1.28	0.82	0.87	1.11	0.81	0.67

Cr	0.01	0.01	0.01	0.01	0.01	0.01	0.00	0.03	0.00	0.00	0.02	0.02
Ti	0.11	0.03	0.02	0.02	0.03	0.03	0.04	0.03	0.03	b.d.	0.03	0.01
Fe^{3+}	0.36	0.32	0.39	0.30	0.32	0.35	0.38	0.39	0.48	0.37	0.31	0.29
Fe^{2+}	1.20	0.37	0.71	0.77	0.87	0.96	1.46	0.48	0.65	0.96	0.95	0.67
Mn	0.02	0.01	0.01	0.01	0.01	0.01	0.03	0.01	0.01	0.01	0.01	0.01
Mg	2.22	3.41	2.98	3.23	3.05	2.88	2.05	3.36	3.10	2.64	2.96	3.42
Ca	1.48	1.35	1.49	1.37	1.35	1.36	1.30	1.37	1.31	1.49	1.38	1.39
Na	1.15	0.86	0.93	0.86	0.91	0.97	1.26	0.84	0.89	1.01	0.89	0.87
K	b.d.	0.06	0.00	0.07	0.07	0.03	b.d.	0.08	0.01	b.d.	0.06	0.09
Total	15.79	15.36	15.53	15.39	15.42	15.46	15.81	15.40	15.35	15.61	15.42	15.43
X_{Fe}	0.35	0.10	0.19	0.19	0.22	0.25	0.42	0.12	0.17	0.27	0.24	0.16

*Total Fe as FeO. Fe^{3+} contents of amphibole were calculated by averaging maximum and minimum values of charge balance method (Leake et al., 1997).
b.d., below detection limit; id, inner domain; od, outer domain; isd, inner sub-domain, osd, outermost sub-domain; incl., inclusion; X_{Fe} = $Fe^{2+}/(Fe^{2+} + Mg)$.

Table II-3. Continued.

mineral	Epidote				Phengite			Paragonite		Plagioclase			
sample	E-1a	E-1c	E-1a	E-1c	E-1a	E-1c	E-1c	E-1a	E-1c	E-1a	E-1c	E-1a	E-1c
	incl. (Grt I id)		matrix porphyroblast		incl. (Grt I od)		incl. (Grt I osd)	incl. (Grt I id)		incl. (Grt I id)		symplectite	
SiO_2	38.62	37.83	38.82	38.35	50.05	51.60	50.97	47.13	46.34	66.85	67.22	65.82	64.97
TiO_2	0.15	0.04	0.19	0.10	0.43	0.51	0.54	0.34	0.41	0.02	0.03	0.02	0.03
Al_2O_3	27.74	24.50	30.03	25.98	28.69	27.25	28.10	39.32	38.55	19.44	20.47	19.14	20.70
Cr_2O_3	0.60	0.31	0.15	0.11	0.05	0.28	0.21	0.06	0.45	b.d.	b.d.	b.d.	b.d.
FeO*	7.30	11.03	4.29	9.62	1.60	1.44	1.56	1.09	0.95	0.88	0.35	0.87	0.35
MnO	0.11	0.17	b.d.	0.12	0.06	b.d.	b.d.	0.04	b.d.	b.d.	b.d.	b.d.	b.d.
MgO	0.41	0.11	0.34	0.15	3.59	4.00	3.85	0.22	0.44	1.26	0.39	1.24	0.39
CaO	22.56	23.05	23.40	23.10	0.06	0.05	0.04	0.39	0.24	1.43	0.77	2.93	3.45
Na_2O	0.05	b.d.	b.d.	0.04	0.83	0.49	0.57	7.52	7.40	9.89	10.89	9.73	9.69
K_2O	b.d.	b.d.	b.d.	b.d.	10.40	10.30	10.27	0.05	1.05	0.04	0.01	0.04	0.01
Total	97.55	97.04	97.23	97.57	95.73	95.91	96.12	96.16	95.82	99.81	100.12	99.78	99.60
Cations per 12.5, 11, and 8 oxygens for epidote, white mica, and feldspar, respectively.													
Si	3.00	2.99	3.00	3.00	3.32	3.40	3.36	2.99	2.97	2.94	2.94	2.91	2.88
Al^{IV}	0.00	0.01	0.00	0.00	0.68	0.60	0.64	1.01	1.03	0.06	0.06	0.09	0.12

Al^{VI}	2.54	2.27	2.73	2.39	1.57	1.52	1.54	1.93	1.89	0.95	0.99	0.91	0.96
Cr	0.04	0.02	0.01	0.01	0.00	0.01	0.01	0.02	0.02	b.d.	b.d.	b.d.	b.d.
Ti	0.01	0.00	0.01	0.01	0.02	0.03	0.03	0.00	0.02	0.00	0.00	0.00	0.00
Fe^{3+}	0.47	0.71	0.28	0.63	-	-	-	-	-	-	-	-	-
Mn^{3+}	0.01	0.00	b.d.	0.01	-	-	-	-	-	-	-	-	-
Fe^{2+}	0.00	0.02	0.00	0.00	0.09	0.08	0.09	0.06	0.05	0.03	0.01	0.03	0.01
Mn	0.00	0.01	b.d.	0.00	0.00	b.d.	b.d.	0.00	b.d.	b.d.	b.d.	b.d.	b.d.
Mg	0.05	0.01	0.04	0.02	0.35	0.39	0.38	0.02	0.04	0.08	0.03	0.08	0.03
Ca	1.88	1.95	1.94	1.93	0.00	0.00	0.00	0.03	0.02	0.07	0.04	0.14	0.16
Na	0.01	b.d.	b.d.	0.01	0.11	0.06	0.07	0.93	0.92	0.84	0.92	0.84	0.83
K	b.d.	b.d.	b.d.	b.d.	0.88	0.87	0.86	0.00	0.09	0.00	0.00	0.00	0.00
Total	8.00	8.00	8.00	8.00	7.03	6.97	6.98	6.99	7.04	4.98	4.99	5.00	5.00
X_{Fe3+}	0.46	0.72	0.28	0.61	-	-	-	-	-	-	-	-	-
An	-	-	-	-	-	-	-	-	-	0.07	0.04	0.14	0.16
Ab	-	-	-	-	-	-	-	-	-	0.92	0.96	0.86	0.83
Or	-	-	-	-	-	-	-	-	-	0.00	0.00	0.00	0.00

*Total Fe as FeO.
b.d., below detection limit; id, inner domain; od, outer domain; osd, outermost sub-domain; incl., inclusion; $X_{Fe3+} = Fe^{3+}/(Al^{VI} + Fe^{3+} – 2)$; An = Ca/M, Ab = Na/M, and Or = K/M, where M = Ca + Na + K.

higher Mg and lower Ca (Prp = 0.32–0.36; Grs = 0.16–0.20; X_{Fe} = 0.55–0.59) relative to the inner sub-domains sparsely observed (Figures II-4a,b and II-5a). Slight enrichments of Fe and Mn are detected along the grain boundary (<10 μm wide) of most garnet grains.

Clinopyroxene

The jadeite content (Jd = Na – Fe^{3+} – Cr) and X_{Fe} values of omphacite inclusions range from 0.28 to 0.35 and from 0.21 to 0.25 respectively (Figure II-5b). Rare omphacite inclusions inside the outermost sub-domain of garnet porphyroblasts are relatively homogeneous in jadeite (Jd = 0.34), but their X_{Fe} values (0.24–0.29) are slightly higher than those inside the inner domains of garnet. The jadeite content of omphacite porphyroblasts is restricted (Jd = 0.34–0.36), and their X_{Fe} values vary from 0.22 to 0.27. A slight increase in the X_{Fe} value (0.27–0.29) is detected at the margin. The omphacite inclusions are higher in aegirine (Aeg = Fe^{3+} = 0.02–0.12) than the omphacite porphyroblasts in the matrix (Aeg = 0.01–0.07). The vermicular clinopyroxene replacing omphacite is diopsidic in composition (Jd = 0.09–0.20).

Amphibole

Amphibole is rich in sodic components and ranges from sodic-calcic to calcic amphibole encompassing barroisite to Mg-pargasite, together with

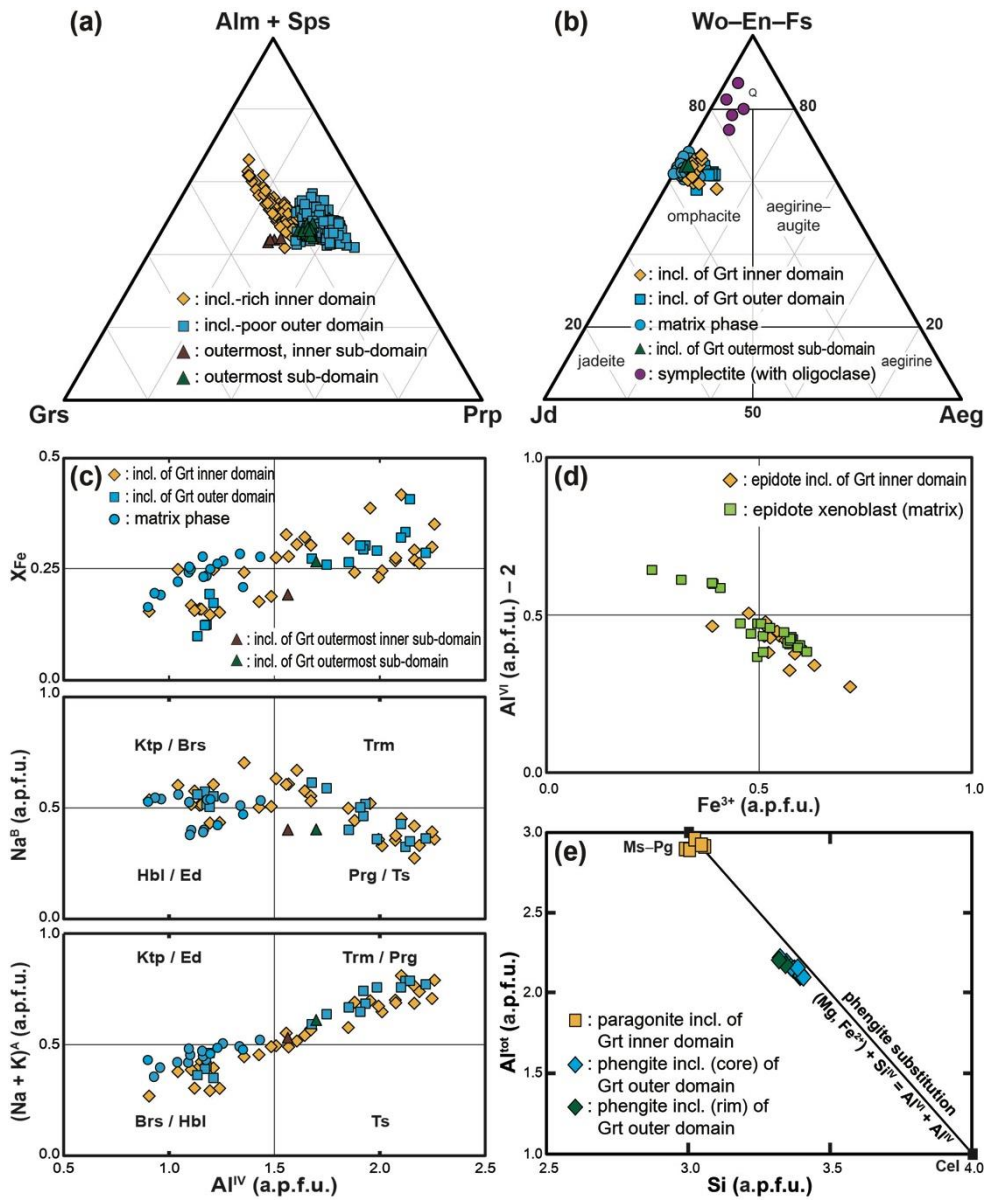

Figure II-5. Compositional diagrams of (a) garnet, (b) clinopyroxene (after Morimoto et al., 1988), (c) amphibole (after Leake et al., 1997), (d) epidote, and (e) paragonite and phengite. incl., inclusion.

minor amounts of Mg-katophorite, -taramite and -hornblende (Figure II-5c; Leake et al., 1997). The compositions of amphibole inclusions in the inner domains of the Grt I and Grt II are subdivided into two groups; high-Al^{IV} (>1.35 a.p.f.u.) Mg-pargasite and low-Al^{IV} (<1.25 a.p.f.u.) barroisite. The former generally occurs as single-phase inclusion, and its Na^{B} (0.27–0.70 a.p.f.u.) and $(Na + K)^{A}$ (0.44–0.81 a.p.f.u.) antithetically vary with increasing Al^{IV} (1.36–2.26 a.p.f.u.). The latter, commonly intergrown with omphacite and/or paragonite, is less variable in Na^{B} and $(Na + K)^{A}$ which are in the range 0.43–0.60 a.p.f.u. and 0.27–0.42 a.p.f.u. respectively. The amphibole inclusion compositions in outer segments of the Grt I and Grt II comprise two groups showing broadly similar trends to those in inner domains. Amphibole porphyroblasts in the matrix are mostly barroisite and Mg-hornblende containing high Na^{B} (0.38–0.56 a.p.f.u.), which are compositionally similar to the barroisitic inclusions. Amphibole enclosed in outermost sub-domains of Grt I and Grt II is represented by Mg-pargasite whose Al^{IV} and Na^{B} are 1.56–1.70 a.p.f.u. and 0.40 a.p.f.u. respectively.

Epidote

Both epidote and allanite occur as inclusions in garnet (Figure II-3c). The compositions of epidote are variable, as shown in Figure II-5d. The X_{Fe3+} (= $Fe^{3+}/(Fe^{3+} + Al^{VI} - 2)$) values of epidote inclusions in the inner part of garnet porphyroblasts are in the range 0.46–0.72, slightly higher than those of xenoblastic epidote in the matrix (X_{Fe3+} = 0.28–0.61).

White mica

The Na/(Na + K + Ca) values of paragonite inclusions in the inner part of garnet porphyroblasts are in the range 0.85–0.97, whereas those of phengite vary from 0.05 to 0.13. Phengite inclusions in the outer segment of garnet are zoned in the celadonite component, slightly decreasing from the core (Si = 3.34–3.40 a.p.f.u.) to rim (Si = 3.32–3.36 a.p.f.u.; Figure II-5e). Stoichiometric Fe^{3+} calculation method was not applied owing to possible octahedral vacancy and O–OH substitution (e.g. Page et al., 2007), although the excess Fe + Mg relative to Si indicates the presence of Fe^{3+} as the ferri-muscovite component (Ahn et al., 1985; Giorgetti et al., 2000). The Ti content of phengite is low (0.02–0.05 a.p.f.u.).

Rutile and plagioclase

The Zr contents of rutile are in the range ~160–230 ppm and appear to be independent of grain sizes and occurrences as inclusion or matrix phase (Table II-2). Rutile contains minor amounts of SiO_2 (<0.04 wt%), Nb_2O_5 (<0.26 wt%), Cr_2O_3 (<0.28 wt%), V_2O_3 (<0.68 wt%) and FeO (<0.74 wt%). The compositions of vermicular plagioclase grains intergrown with diopside belong to oligoclase (An = Ca/(Ca + Na + K) = 0.14–0.16), whereas those of inclusion phases in the garnet core are albite (An = 0.04–0.07).

METAMORPHIC EVOLUTION

On the basis of the petrography and mineral chemistry, four metamorphic stages (M_1–M_4) are defined in two eclogite samples E-1a and E-1c (Figure II-6). Inclusion assemblages in the inner core of garnet porphyroblasts (Grt I and Grt II) define the prograde M_1 stage, whereas those of inclusion-poor outer mantle denote the M_2. Two sub-domains of the outermost garnet rim represent the M_{3A} and M_{3B} respectively. Symplectites of diopside and oligoclase replacing omphacite grains are the M_4 product. An inclusion assemblage of paragonite and Mg-pargasite together with albite and titanite inside the garnet core suggests the presence of pre-M_1 episode, possibly belonging to the amphibolite facies. In the following sections, I describe metamorphic reactions responsible for producing mineral assemblages at the M_1–M_4 stages.

The M_1 prograde eclogite facies assemblage is characterized by the inclusion-rich inner domains of garnet porphyroblasts and enclosed minerals therein, that is, garnet + omphacite + barroisite/Mg-pargasite + epidote + phengite + paragonite + rutile/titanite + quartz (Figure II-4b–d). The outward monotonous decrease in the X_{Fe} value (from 0.85 to 0.56) of garnet with bell-shaped Mn profile indicates its prograde growth at the expense of chlorite by the reaction (1) of Konrad-Schmolke et al. (2008):

chlorite + epidote + quartz

= garnet + calcic amphibole (Mg-pargasite) + H_2O.

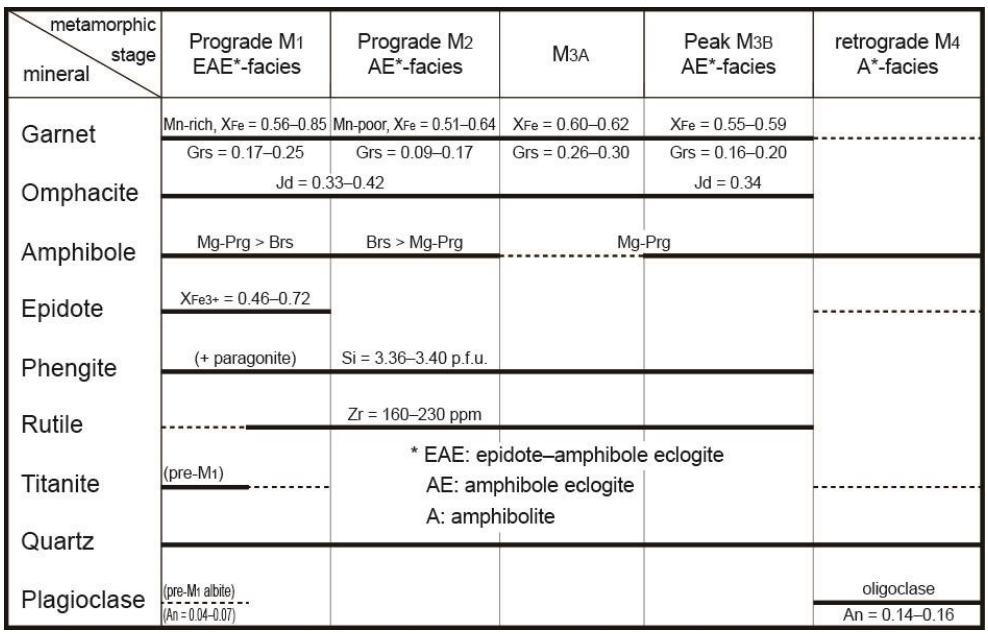

Figure II-6. Mineral paragenesis diagram of barroisite eclogites (sample E-1a and E-1c). Compositions of minerals are given for each metamorphic stage. Dashed lines represent rare or highly probable occurrence of each phase.

The M_2 stage represents the metamorphic growth of garnet and omphacite at the expense of barroisitic amphibole, which is reflected in the Jd zonation of prismatic omphacite and the Grs trend (from 0.18 to 0.08) of the outer domain of the Grt I and Grt II (Figures II-4 and II-5). Similar to the 'reaction (3)' of Konrad-Schmolke et al. (2008), the reaction governing the M_2 is simplified as:

sodic-calcic amphibole + Jd-poorer clinopyroxene

= garnet + Jd-richer clinopyroxene + quartz + H_2O.

This reaction is most likely concurrent with the transition from calcic (Mg-pargasite; M_1) to sodic-calcic (barroisite; M_2) amphibole, because the latter is predominant in the matrix as well as the inclusion assemblages (Figure II-5c).

The M_{3A} stage is represented by the irregularly shaped, isolated inner sub-domain of the outermost part enriched in grossular (Grs = 0.26–0.30; Figures II-4 and II-5), which may represent an inheritance from the former calcic minerals such as omphacite and amphibole due to slow diffusivity of Ca (Chernoff and Carlson, 1997; Kim and Cho, 2008). Relatively dry conditions of the eclogite subsequent to the $M_{1–2}$ dehydration might further decelerate the Ca mobility during the M_{3A} garnet growth (e.g. Rubie, 1990). The M_{3A} garnet growth due to the fractionation effect (e.g. Konrad-Schmolke et al., 2008) cannot account for an abrupt increase in

grossular of the outermost sub-domain (M_{3B} garnet). Thus, the grossular enrichment in the M_{3A} garnet likely reflects the variation in local bulk compositions instead of *P–T* conditions (Castro and Spear, 2017; Kim and Cho, 2008); the *P–T* conditions for the M_3 garnet overgrowth are estimated only from the composition of the M_{3B} garnet. The M_{3B} growth stage was subject to the same reaction producing the M_2 garnet.

The M_4 represents the exhumation stage and is typified by the symplectitic growth of diopside–oligoclase at the expense of omphacite. This replacement is well accounted for by an anhydrous reaction (Mysen and Griffin, 1973):

omphacite + quartz = diopsidic clinopyroxene + oligoclase.

PRESSURE AND TEMPERATURE ESTIMATIONS

The garnet–clinopyroxene–phengite–kyanite–quartz/coesite (GCPKS) thermobarometry of Ravna and Terry (2004) was applied for *P–T* estimations using internally consistent thermodynamic data sets of Holland and Powell (1998, 2011). The *P–T* pseudosections were calculated in the Na_2O–CaO–K_2O–FeO–MgO–Al_2O_3–SiO_2–H_2O–Fe_2O_3 (± MnO) model system using the theriak–domino software (de Capitani and Petrakakis, 2010). Solid-solution phases (and references for their activity models) were: garnet (White et al., 2007), clinopyroxene (Green et al., 2007), amphibole (Diener and Powell, 2012), epidote and talc (Holland and Powell, 1998),

white mica (Coggon and Holland, 2002), chloritoid (White et al., 2000), chlorite (Holland et al., 1998) and feldspar (Baldwin et al., 2005). Pure end-member phases include lawsonite, kyanite, quartz/coesite and H_2O. H_2O is set to be in excess. The *P*–*T*–M_{H2O} relationship, shown in Figure II-7, further suggests that >10 and 1 mol.% of H_2O are necessary for the H_2O saturation of assemblages M_1 and M_2 respectively. Relatively high amounts of H_2O are required for the M_1 assemblages in which hydrous phases such as amphibole, epidote and chlorite are stable (Figure II-7). The Fe^{3+} content of each bulk composition was estimated on the basis of *P*–X_{Fe3+} and *T*–X_{Fe3+} diagrams (Figure II-8), where $X_{Fe3+} = Fe_2O_3/(FeO + Fe_2O_3)$. Based on this estimation, I adopted the X_{Fe3+} values of 0.40 and 0.18 for original and Grt_{M1}-subtracted bulk-rock compositions respectively. The former is similar to the X_{Fe3+} values of medium-*T* eclogites (e.g. Chen et al., 2013; Rebay et al., 2010), whereas the latter to those of unaltered mid-ocean ridge basalts (e.g. Cottrell and Kelly, 2011). Partial melting was not considered. The appropriate amount of Ca (= 3.33 molar P_2O_5) was subtracted from whole-rock composition to account for the occupancy by apatite. TiO_2 was ignored because of its predominance in rutile.

Thermobarometry

Although barroisite eclogite samples are apparently free of kyanite, I obtained *P*–*T* constraints using compositions of the GCP assemblage, based on the calibration of Ravna and Terry (2004) (Figure II-9). Uncertainties in

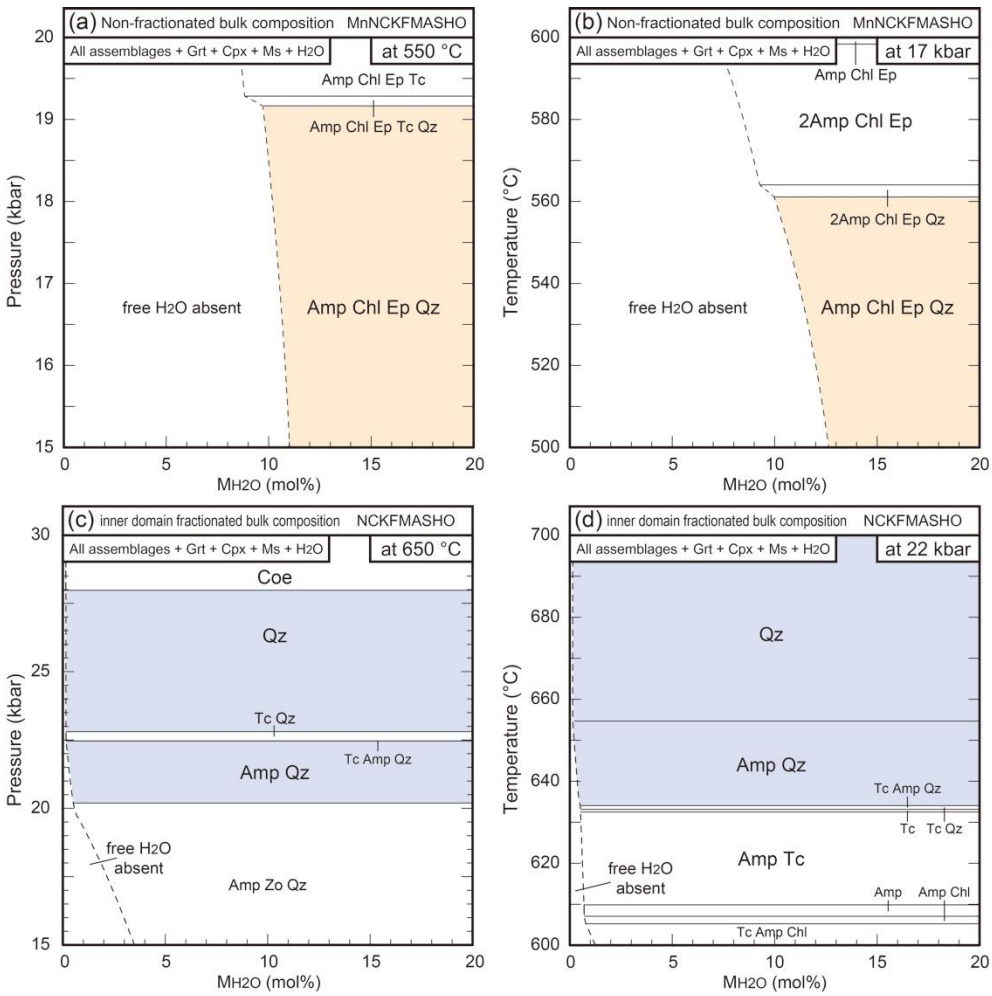

Figure II-7. The *P*– and *T*–M_{H2O} diagrams for the original (a, b) and modified bulk-rock compositions (c, d) of the eclogite samples. The aqueous fluid phase is absent in the modelled *P*– and *T*–M_{H2O} fields where the bulk-rock H_2O contents are lower than those marked by broken lines. The stability fields of the M_1 (>1 mol.% H_2O) and M_2 (>10 mol.% H_2O) assemblages in the eclogites are colored in orange and blue, respectively.

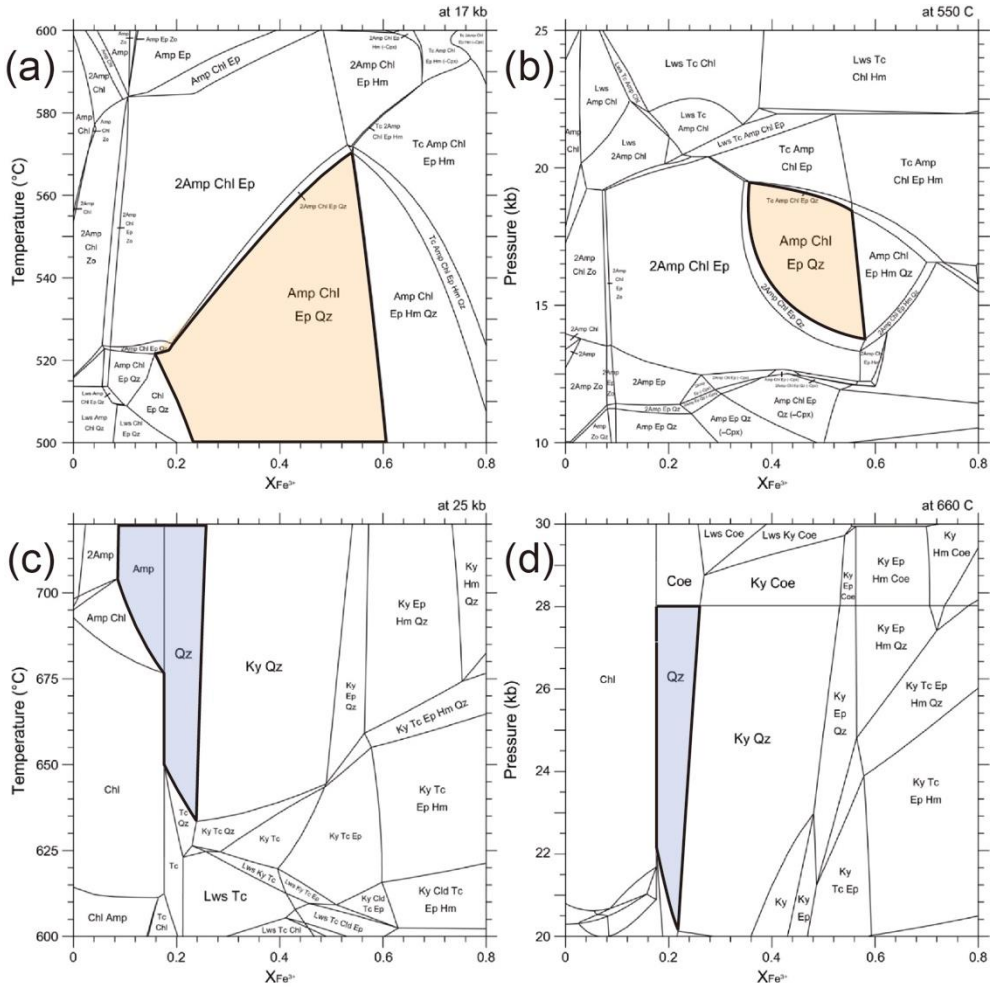

Figure II-8. The *P*– and *T*–X_{Fe3+} diagrams for the original (a, b) and modified (c, d) bulk-rock compositions of the eclogite samples. The assemblages of interest are colored in orange and blue, respectively.

temperature estimates are large owing to the assumption of ferric ion contents (Ravna and Paquin, 2003). Four pairs of the M_2 garnet and its omphacite–phengite inclusions yielded ~25 ± 3 kbar and 660 ± 100 °C (2σ) for the M_2 stage. Combined with the inclusions of M_{3B} omphacite and phengite, the high-grossular marginal overgrowth of M_{3B} garnet gave ~26 ± 3 kbar and 720 ± 80 °C (2σ) for the M_3 stage (Figure II-9). The Zr-in-rutile thermometer (Tomkins et al., 2007) resulted in ~650–700 °C (at 22–27 kbar; Figure II-9). The jadeite contents (Jd = 0.09 and 0.20) of diopside replacing omphacite gave the maximum pressure for the M_4 decompression, ~7–8 kbar and 10–12 kbar at 500–600 °C respectively (Figure II-9; Holland, 1980, 1983).

Pseudosection modelling

The bulk-rock compositions used for the pseudosection construction are twofold: (a) an average composition of two eclogite samples (E-1a and E-1c) which are petrologically identical; and (b) an effective bulk composition estimated from the average composition modified by subtracting elemental proportions of the M_1 garnet, corresponding to ~25–30 vol.% in a single garnet grain (Table II-4; Du et al., 2014). The former, incorporating the MnO component, was used for deciphering the prograde assemblage involving Mn-rich M_1 garnet. On the other hand, this component was excluded in the latter for reproducing the M_2 assemblage because of negligible Sps contents in the M_2 garnet. Appropriate amounts of

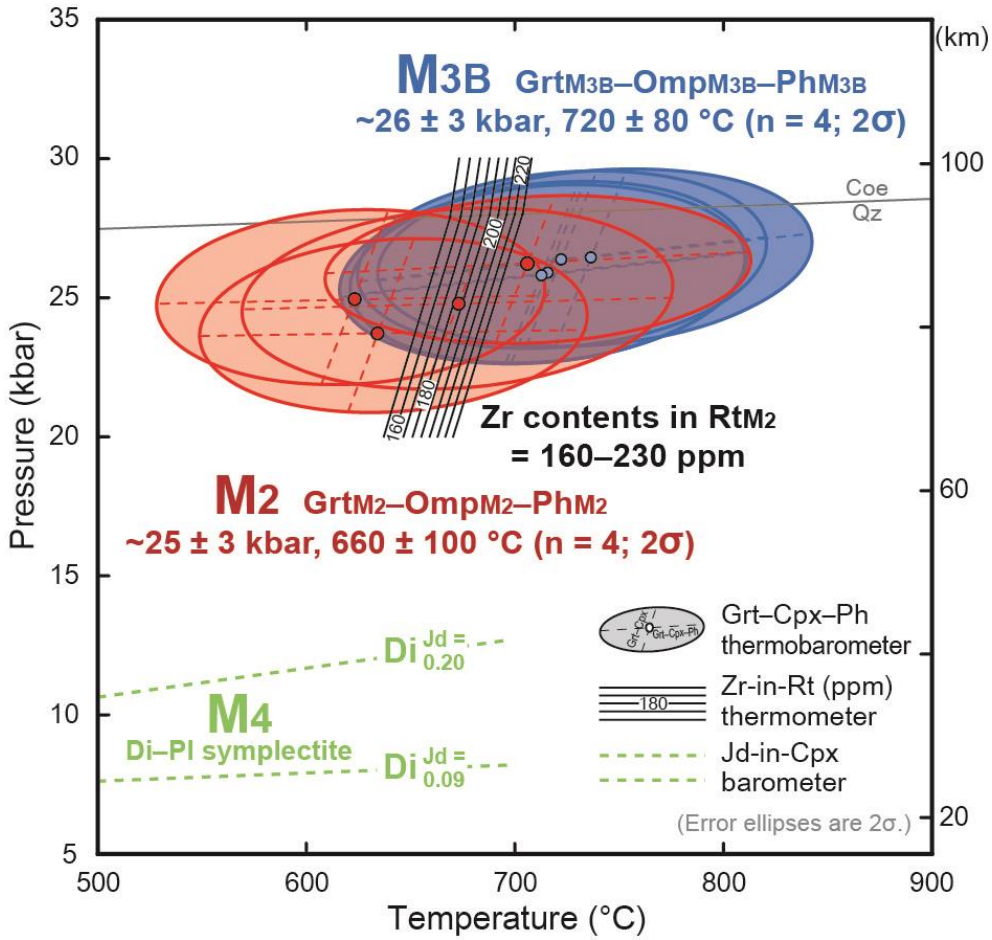

Figure II-9. The *P–T* diagram summarizing the thermobarometric results. The Grt–Cpx–Ph (GCP) thermobarometer (red and blue error ellipses for M_2 and M_{3B}, respectively) is from Ravna and Terry (2004), the Zr-in-Rt thermometer (black lines with Zr contents in ppm) from Tomkins et al. (2007), and the Jd-in-Cpx barometer (green broken line) from Holland (1980, 1983).

Table II-4. Whole-rock and effective bulk compositions used for calculating the pseudosections.

(wt%)	Raw data		Average composition[a]	Effective bulk composition[a]
sample	E-1a	E-1c		
SiO_2	45.94	45.83	47.99	49.40
TiO_2	1.74	1.82	-	-
Al_2O_3	14.61	14.63	15.29	13.59
Fe_2O_3[b]	14.33	14.06	12.02	11.54
MnO	0.80	0.83	0.85	-
MgO	9.11	8.86	9.40	9.81
CaO	11.08	11.22	11.61	12.21
Na_2O	2.66	2.63	2.77	3.35
K_2O	0.10	0.06	0.08	0.10
P_2O_5	0.03	0.05	-	-
LOI[c]	0.23	0.22	-	-
Total	100.63	100.22	100.00	100.00

[a], Used for calculating pseudosections. Normalized to 100.
[b], Total Fe as Fe_2O_3.
[c], Loss of ignition.

MnO and other major oxides were extracted from the effective bulk composition following an ideal stoichiometry of the M_1 garnet.

Pseudosection using an average bulk-rock composition

The *P–T* pseudosection was calculated at a *P–T* range of 10–25 kbar and 500–800 °C using the average whole-rock composition (Figure II-10a), and was contoured with isopleths of pyrope and grossular in the M_1 garnet domain (Figure II-10b). The result suggests that the Grt + Omp + Amp + Ep + Ph + H_2O assemblage is stable over a wide *P–T* range, explaining its predominance in the M_1. The prograde M_1 conditions were constrained to be ~15–20 kbar and 520–570 °C on the basis of: (a) the stability field of Grt + Omp + Amp + Chl + Ep + Ph + Qz assemblage; and (b) the intersectional isopleths of the M_1 garnet (Sps = 0.12–0.16, Prp = 0.12–0.16 and Grs = 0.26–0.28). Chlorite is not present in the eclogite samples, and might have been exhausted during the dehydration reaction at M_1 (e.g. Konrad-Schmolke et al., 2008). The *P–T* range for the M_1 belongs to the stability field of rutile (Figure II-10b; Liu et al., 1996) which occurs as an inclusion phase in the M_1 garnet.

Pseudosection using a fractionated bulk composition

The *P–T* pseudosection was calculated at a *P–T* range of 5–35 kbar and 500–900 °C using the M_1 garnet-sequestered effective bulk composition (Figure II-10c), and was contoured with compositional isopleths of garnet,

Figure II-10. The *P–T* pseudosections of barroisite eclogites, using (a, b) average whole-rock compositions of samples E-1a and E-1c and (c, d) effective bulk compositions, respectively. The equilibrium assemblage fields in (a) and (c) are shaded by grey-scale colors reflecting the degree of freedom. All fields contain garnet, clinopyroxene (mostly omphacite), muscovite (mostly phengite), and H_2O, unless stated. Colored curves refer to mineral-in/out boundaries. The Mn-bearing pseudosection (b) simplified from (a) is contoured with the grossular, pyrope, and spessartine isopleths of garnet. An orange area represents the M_1 *P–T* conditions responsible for the growth of Mn-rich garnet. The Mn-free pseudosection (d) simplified from (c) is contoured with mineral isopleths of garnet, phengite, and amphibole. Red area represents the *P–T* field of the M_2. The error ellipses are adopted from the *P–T* estimates in Figure II-9. Two bold arrows in (d) indicate prograde *P–T* trajectories of $M_{1–2}$ and $M_{2–3B}$, respectively, and green for $M_{3–4}$. Wet solidus curve for basalt (dashed) is from Lambert and Wyllie (1972). The phase stability curves among rutile, titanite, and ilmenite of quartz tholeiite in (d) are from Liu et al. (1996).

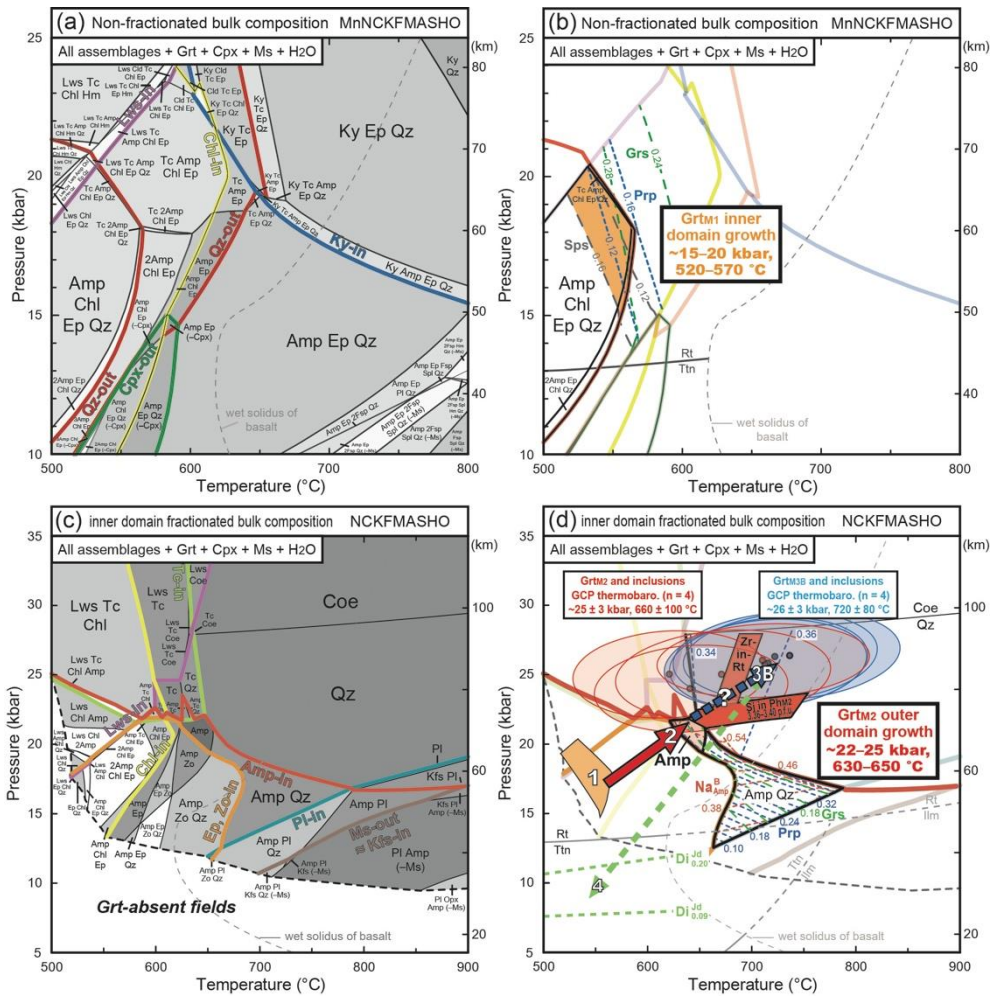
(a) Non-fractionated bulk composition MnNCKFMASHO
All assemblages + Grt + Cpx + Ms + H2O
Ky Ep Qz
Amp Chl Ep Qz
Amp Ep Qz
Lws Tc Chl Hm
Lws-in
Chl-in
Ky-in
Qz-out
Cpx-out
wet solidus of basalt
(b) Non-fractionated bulk composition MnNCKFMASHO
All assemblages + Grt + Cpx + Ms + H2O
GrtM1 inner domain growth ~15–20 kbar, 520–570 °C
Grs
Prp
Sps
Rt
Ttn
wet solidus of basalt
(c) inner domain fractionated bulk composition NCKFMASHO
All assemblages + Grt + Cpx + Ms + H2O
Lws Tc Chl
Coe
Qz
Amp Qz
Amp Pl
Pl Amp (–Ms)
Lws-in
Chl-in
Amp-in
Pl-in
Ep, Zo-in
Ms-out ≈ Kfs-in
Grt-absent fields
wet solidus of basalt
(d) inner domain fractionated bulk composition NCKFMASHO
All assemblages + Grt + Cpx + Ms + H2O
GrtM2 and inclusions GCP thermobaro. (n = 4) ~25 ± 3 kbar, 660 ± 100 °C
GrtM3B and inclusions GCP thermobaro. (n = 4) ~26 ± 3 kbar, 720 ± 80 °C
GrtM2 outer domain growth ~22–25 kbar, 630–650 °C
Zr-in-Rt
Amp
Amp Qz
Grs
Prp
Di
Rt
Ttn
Ilm
wet solidus of basalt
Pressure (kbar)
Temperature (°C)
(km)

amphibole and phengite (Figure II-10d). The result suggests that the Grt + Omp + Amp + Ph assemblage is stable over a wide *P–T* range, explaining its predominance in the eclogite samples. On the basis of the stability field of Grt + Omp + Amp + Ph ± Qz assemblage, the intersectional isopleths of pyrope and grossular in the M_2 garnet (Prp = 0.36–0.38, Grs = 0.18–0.20), the Si isopleths of phengite (3.36–3.40 a.p.f.u.) and the Na^B isopleths of barroisite (up to 0.57 a.p.f.u.), the M_2 conditions were estimated at ~20–23 kbar and 630–650 °C (Figure II-10d). This *P–T* result is consistent with that from the thermobarometric calculations (~25 ± 3 kbar and 660 ± 100 °C).

ZIRCON GEOCHRONOLOGY

Zircon crystals from a barroisite eclogite sample (E-1a) are subhedral to anhedral and ~50–300 μm in size; their aspect ratios reach up to 3 (Figure II-11). The majority of zircon is >100 μm in the longest dimension, and typically shows core-mantle-rim growth zones: (a) the core is euhedral to subhedral, intermediate in CL intensities and generally homogeneous except for weak oscillatory zonation; (b) the mantle shows euhedral or subhedral boundary and dark CL oscillatory zoning with low contrast and (c) the outermost rim is structureless and bright in CL intensities. The core and mantle domains are often corroded. On the other hand, relatively fine-grained zircon neoblasts, ~50–100 μm in the longest dimension, are mostly zoned with thin bright-CL rims, but the core-mantle-rim structure recognized in the larger crystals is absent. Fine-grained (<30

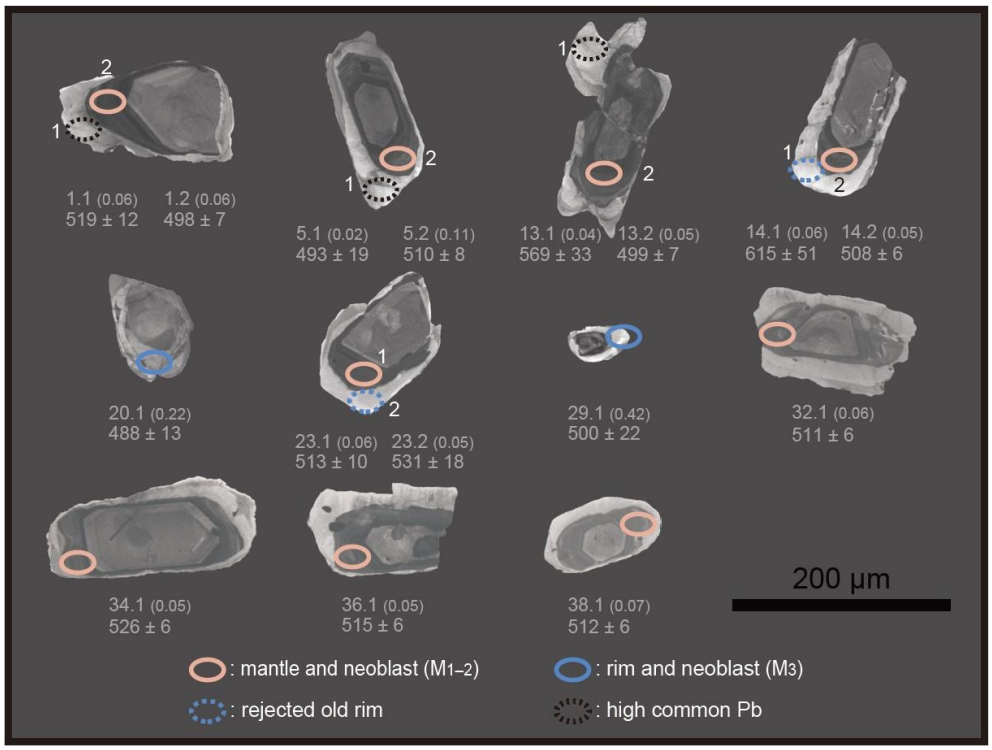

Figure II-11. Representative cathodoluminescence images of zircon from a barroisite eclogite (sample E-1a). Spot numbers for the U-Th-Pb analysis listed in Table II-5 are shown for individual zircon grains, followed by their Th/U ratios in parentheses. The bottom lines list the $^{206}Pb/^{238}U$ dates (in Ma) with 1σ errors. Ellipses denote the analytical spots.

μm) inclusions are occasionally present inside zircon, and apparently distinctive in each domain: the cores of zircon mainly contain quartz and needle-shaped apatite, indicating an igneous origin (Bacon, 1989; Tomaschek et al., 2003), whereas the mantle and rim enclose garnet, omphacite, epidote, allanite, rutile and apatite (Figures II-12 and II-13). The inclusions in zircon neoblasts are variable and comprise garnet, omphacite, barroisite, epidote, phengite and rutile together with rare quartz (Figure II-11).

The U-Th-Pb isotopic compositions of 50 spots measured on 40 zircon crystals are shown in the Tera-Wasserburg concordia diagram (Figure II-14a; Table II-5). These data reveal an apparently bimodal distribution of U (2–57 ppm and 77–311 ppm), low concentration of Th (0.1–51 ppm except for a spot 22.1) and relatively low concentration of radiogenic Pb. As a consequence, the proportion of common lead could be high enough to result in large uncertainties and discordances (e.g. Rubatto et al., 1999; Timmermann et al., 2004). Thus, 19 analyses with >1% common ^{206}Pb were rejected in the age calculation (Figure II-14a). An additional four analyses with $^{207}Pb/^{206}Pb$ ratios below zero (spots 3.1, 10.2, 12.1 and 16.1) were discarded because of possible Pb overcorrection. Four spot analyses from the outermost rim (spots 10.1, 11.1, 14.1 and 23.2) yielded $^{206}Pb/^{238}U$ ages older than the core or mantle of each grain, and were also ignored in the mean age calculation. The U-Pb isotopic compositions of the remaining 23 analyses from mantle-rim domains and neoblasts of zircon are clustered

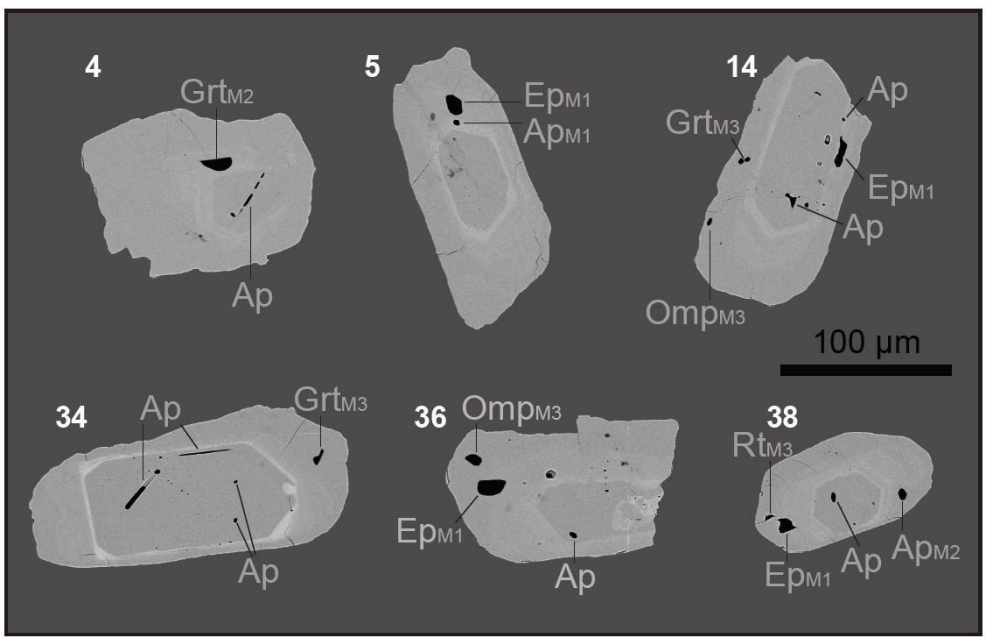

Figure II-12. Backscattered electron images of zircon showing fine-grained mineral inclusions of metamorphic or igneous origin. Metamorphic inclusions are denoted as M_1, M_2, and M_3, whereas igneous ones are represented by apatite. The spot numbers for the SHRIMP zircon analyses (Table II-5) are shown.

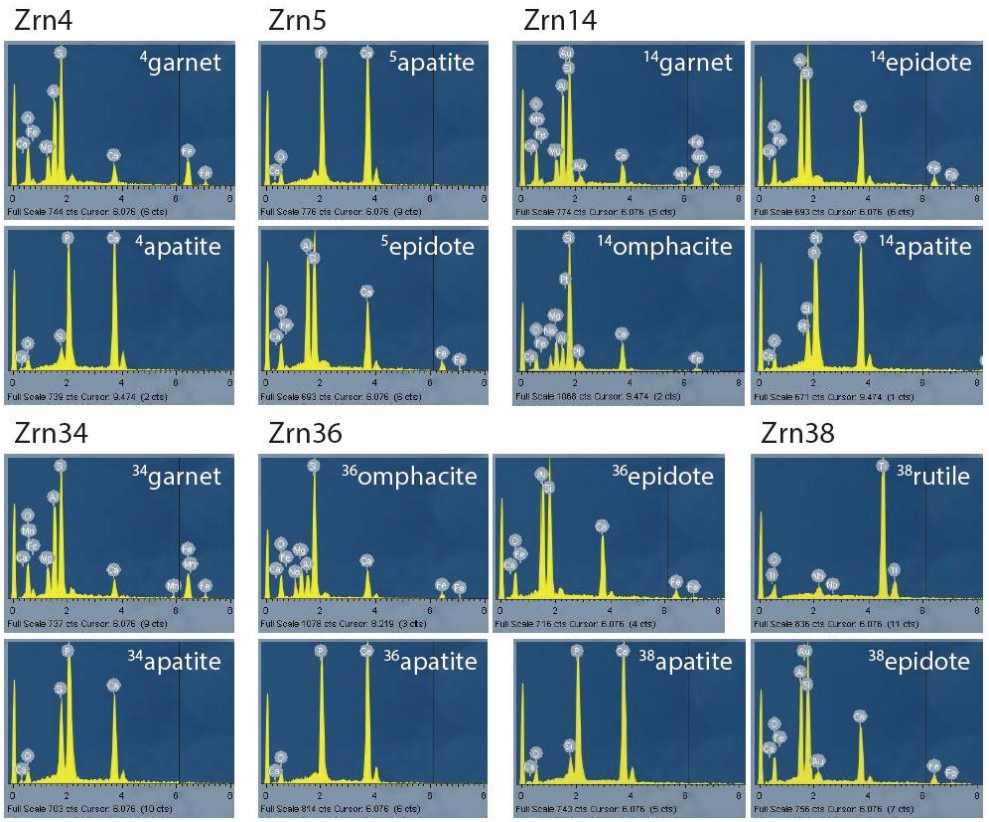

Figure II-13. Energy dispersive spectroscopy profiles of mineral inclusions in zircon. The spot numbers for the SHRIMP zircon analyses (Table II-5) are shown.

Figure II-14. (a) Tera-Wasserburg concordia diagram showing the SHRIMP spot dates of zircon from a barroisite eclogite (sample E-1a). Dashed ellipses denote spot analyses that are excluded in the mean age calculation. Inset diagram shows the error bars of each $^{206}Pb/^{238}U$ date, which are color-coded similar to the error ellipses. (b–c) The weighted mean $^{206}Pb/^{238}U$ ages of two zircon domains, mantle and rim, respectively. The U-Pb spot dates of neoblasts are incorporated into age calculations for each domain. MSWD, mean square of weighted deviates.

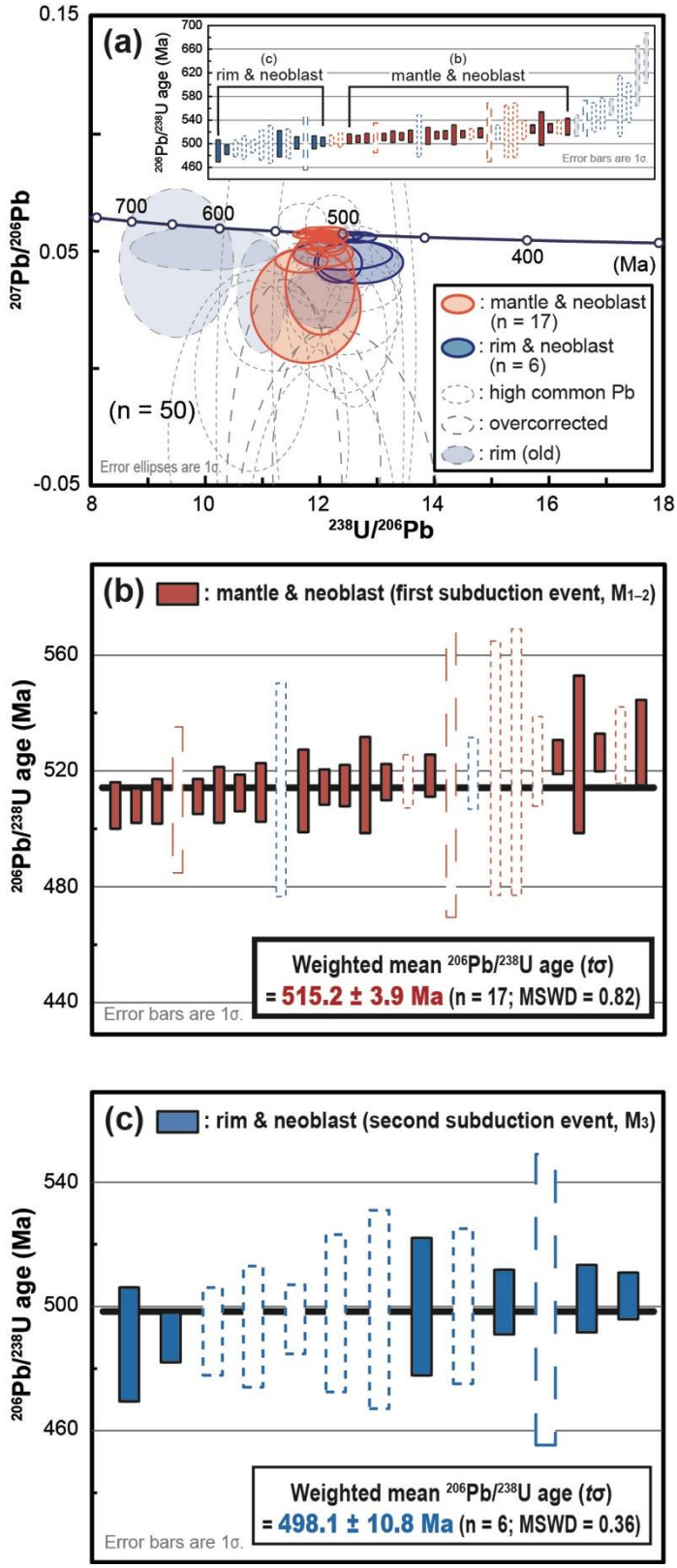
(a)
(c)
rim & neoblast
(b)
mantle & neoblast
Error bars are 1σ.
700
600
500
400
(Ma)
: mantle & neoblast (n = 17)
: rim & neoblast (n = 6)
: high common Pb
: overcorrected
: rim (old)
(n = 50)
Error ellipses are 1σ.
0.15
0.05
-0.05
8
10
12
14
16
18
207Pb/206Pb
238U/206Pb
(b) : mantle & neoblast (first subduction event, M1–2)
560
520
480
440
206Pb/238U age (Ma)
Weighted mean 206Pb/238U age (tσ)
= 515.2 ± 3.9 Ma (n = 17; MSWD = 0.82)
Error bars are 1σ.
(c) : rim & neoblast (second subduction event, M3)
540
500
460
206Pb/238U age (Ma)
Weighted mean 206Pb/238U age (tσ)
= 498.1 ± 10.8 Ma (n = 6; MSWD = 0.36)
Error bars are 1σ.

Table II-5. The SHRIMP U-Th-Pb isotopic compositions of zircon from the barroisite eclogite.

Spot no.	Texture	U (ppm)	Th (ppm)	Th/U	Common ^{206}Pb (%)	$^{207}Pb^*/^{206}Pb^*$	$^{208}Pb^*/^{206}Pb^*$	$^{206}Pb^*/^{238}U$	$^{208}Pb^*/^{232}Th$	$^{207}Pb/^{206}Pb$ age (Ma)	$^{206}Pb/^{238}U$ age (Ma)	$^{208}Pb/^{232}Th$ age (Ma)	Concordance (%)
Sample E-1a													
1.1	rim	110	6	0.06	1.94	0.05075 ± 244	0.0218 ± 336	0.08390 ± 205	0.031 ± 494	229 ± 115	519 ± 12	622 ± 97	90
2.1	mantle	176	13	0.07	0.32	0.05136 ± 258	0.0196 ± 309	0.08262 ± 161	0.022 ± 354	257 ± 120	512 ± 10	443 ± 70	91
3.1	neoblast	14	3	0.19	0.16	-0.04006 ± 3771	0.0354 ± 1855	0.08233 ± 422	0.015 ± 813	-	510 ± 25	309 ± 163	-
4.1	rim	7	0	0.03	2.12	-0.07613 ± 5069	-0.0059 ± 2069	0.08287 ± 593	-0.019 ± 6707	-	513 ± 35	-	-
4.2	mantle	197	51	0.26	3.46	0.06281 ± 490	0.1662 ± 572	0.08539 ± 200	0.055 ± 245	702 ± 175	528 ± 12	1081 ± 47	107
5.1	rim	21	0	0.02	3.68	0.04731 ± 881	0.0144 ± 1131	0.07956 ± 324	0.059 ± 4642	65 ± 515	493 ± 19	1156 ± 906	85
5.2	mantle	215	24	0.11	0.21	0.05243 ± 206	0.0374 ± 132	0.08226 ± 130	0.027 ± 110	304 ± 92	510 ± 8	543 ± 22	93
6.1	mantle	24	3	0.12	1.20	0.03358 ± 877	0.0412 ± 592	0.08458 ± 260	0.030 ± 445	-	523 ± 15	593 ± 88	63
6.2	mantle	77	4	0.05	0.87	0.04558 ± 332	0.0181 ± 413	0.08551 ± 221	0.030 ± 694	-	529 ± 13	598 ± 137	82
7.1	neoblast	24	4	0.18	0.23	0.03601 ± 1456	0.0425 ± 1102	0.08320 ± 276	0.020 ± 520	-	515 ± 16	397 ± 103	67
8.1	rim	7	0	0.03	1.06	-0.03123 ± 4810	0.0076 ± 1507	0.09142 ± 868	0.026 ± 5143	-	564 ± 52	519 ± 989	-
8.2	mantle	170	8	0.05	1.61	0.05411 ± 202	0.0163 ± 310	0.08161 ± 146	0.027 ± 518	376 ± 86	506 ± 9	538 ± 102	95
9.1	rim	25	6	0.24	2.83	0.01644 ± 1197	0.0667 ± 854	0.08929 ± 442	0.025 ± 358	-	551 ± 26	504 ± 71	32
10.1	rim	28	0	0.01	0.77	0.03031 ± 1597	0.0016 ± 532	0.09110 ± 230	0.011 ± 3677	-	562 ± 14	221 ± 722	57
10.2	mantle	2	0	0.06	0.03	-0.78191 ± 33407	-0.0004 ± 4150	0.08388 ± 834	-0.001 ± 6045	-	519 ± 50	-	-

11.1	rim	13	1	0.06	0.66	0.04466	±	2106	0.0276	±	1224	0.10526	±	729	0.045	±	2048		-	645	± 43	891	± 400	77
11.2	mantle	167	9	0.06	8.48	0.05635	±	137	0.0181	±	196	0.08347	±	149	0.027	±	305	466	± 55	517	± 9	546	± 60	98
12.1	rim	6	0	0.05	0.48	-0.05803	±	6313	-0.0040	±	2226	0.08785	±	514	-0.007	±	3720		-	543	± 31		-	-
13.1	rim	11	0	0.04	4.87	-0.00385	±	2701	0.0060	±	855	0.09235	±	563	0.014	±	2018		-	569	± 33	284	± 398	-
14.1	rim	19	1	0.06	0.88	0.05077	±	611	0.0181	±	914	0.10009	±	859	0.032	±	1660	230	± 256	615	± 51	638	± 328	87
14.2	mantle	179	9	0.05	-0.01	0.05621	±	77	0.0193	±	340	0.08190	±	97	0.024	±	229	461	± 30	508	± 6	488	± 45	89
15.1	rim	25	6	0.25	2.04	0.03497	±	772	0.0772	±	576	0.08029	±	423	0.024	±	241		-	498	± 25	487	± 48	65
16.1	neoblast	5	0	0.08	0.51	-0.08077	±	6382	0.0090	±	1299	0.08102	±	784	0.009	±	1333		-	502	± 47	185	± 265	-
17.1	neoblast	28	0	0.00	4.04	0.02308	±	2265	-0.0097	±	770	0.08067	±	415	-0.228	±	18567		-	500	± 25		-	45
18.1	mantle	49	18	0.37	0.01	0.04886	±	395	0.1007	±	562	0.08287	±	239	0.022	±	145	141	± 180	513	± 14	448	± 29	87
19.1	neoblast	52	9	0.17	0.09	0.04454	±	542	0.0522	±	451	0.08108	±	180	0.024	±	220		-	503	± 11	485	± 43	81
20.1	neoblast	40	9	0.22	0.50	0.04490	±	591	0.0637	±	526	0.07860	±	303	0.023	±	218		-	488	± 18	461	± 43	82
21.1	neoblast	308	0	0.00	0.16	0.05632	±	125	-0.0014	±	109	0.08091	±	173	-0.250	±	19873	465	± 50	502	± 10		-	99
22.1	neoblast	311	373	1.20	0.14	0.05550	±	140	0.3714	±	220	0.08122	±	127	0.025	±	47	432	± 57	503	± 8	503	± 9	97
23.1	mantle	155	10	0.06	0.11	0.05889	±	73	0.0200	±	212	0.08276	±	169	0.025	±	279	563	± 27	513	± 10	508	± 55	102
23.2	rim	14	1	0.05	0.04	0.02957	±	879	0.0221	±	847	0.08307	±	300	-0.083	±	3908		-	531	± 18		-	-
24.1	neoblast	17	5	0.28	0.27	0.02637	±	1617	0.0841	±	857	0.08498	±	456	0.026	±	312		-	526	± 27	510	± 62	50
25.1	neoblast	40	8	0.19	1.47	0.04368	±	1052	0.0251	±	297	0.08003	±	183	0.025	±	297		-	496	± 11	501	± 59	79
25.2	neoblast	16	1	0.03	2.40	-0.15688	±	3501	0.0934	±	3060	0.08423	±	739	0.093	±	3060		-	521	± 44	1804	± 574	-

26.1	neoblast	247	50	0.20	0.21	0.05657	±	236	0.0243	±	121	0.08197	±	137	0.024	±	121	475	± 95	508	± 8	485	± 24	99
27.1	neoblast	3	0	0.14	6.10	-0.02055	±	13029	0.0251	±	2136	0.08444	±	771	0.025	±	2136		-	523	± 46	501	± 426	-
27.2	neoblast	57	14	0.25	1.66	0.06232	±	757	0.0255	±	298	0.08169	±	208	0.025	±	298	685	± 283	506	± 12	508	± 59	107
28.1	neoblast	5	0	0.02	10.49	0.00811	±	8704	0.1381	±	12635	0.08043	±	536	0.138	±	12635		-	499	± 32	2615	± 2378	17
29.1	neoblast	108	46	0.42	0.37	0.04822	±	425	0.0263	±	181	0.08057	±	371	0.026	±	181	110	± 196	500	± 22	524	± 36	86
30.1	neoblast	16	1	0.07	1.12	0.01149	±	1889	0.0291	±	912	0.07925	±	235	0.029	±	912		-	492	± 14	580	± 180	23
31.1	neoblast	84	49	0.60	0.21	0.05568	±	147	0.1802	±	465	0.07889	±	132	0.023	±	69	439	± 59	490	± 8	465	± 14	88
32.1	mantle	180	10	0.06	0.03	0.05486	±	106	0.0176	±	360	0.08228	±	101	0.015	±	334	407	± 43	511	± 6	308	± 66	74
33.1	mantle	138	9	0.06	0.00	0.05775	±	62	0.0204	±	371	0.08375	±	119	0.026	±	112	520	± 24	518	± 7	525	± 22	100
34.1	mantle	181	9	0.05	0.03	0.05694	±	114	0.0155	±	412	0.08499	±	106	0.022	±	246	489	± 44	526	± 6	447	± 49	92
35.1	mantle	140	8	0.06	0.07	0.05347	±	139	0.0195	±	369	0.08278	±	116	0.013	±	436	349	± 59	515	± 7	255	± 87	51
36.1	mantle	208	10	0.05	0.02	0.05638	±	78	0.0150	±	340	0.08298	±	98	0.020	±	245	467	± 31	515	± 6	400	± 49	90
37.1	mantle	172	17	0.10	-0.12	0.05232	±	122	0.0356	±	348	0.08283	±	102	0.018	±	232	299	± 53	516	± 6	369	± 46	26
38.1	mantle	183	12	0.07	0.53	0.05695	±	128	0.0235	±	354	0.08266	±	104	0.028	±	362	490	± 49	512	± 6	548	± 71	95
39.1	rim	10	0	0.03	2.77	0.02556	±	1341	0.0172	±	1405	0.08036	±	427	-0.567	±	19603		-	545	± 24		-	-
40.1	mantle	226	23	0.10	-0.04	0.05617	±	73	0.0298	±	335	0.08466	±	99	0.021	±	126	459	± 29	525	± 6	417	± 25	85

Errors are 1σ estimates. All the isotopic compositions were calculated using the ^{207}common Pb correction method except for $^{207}Pb^{*}/^{206}Pb^{*}$ ratios corrected by ^{204}Pb. Pb^{*} denotes radiogenic Pb. Concordance was calculated from $^{207}Pb/^{235}U$ and $^{206}Pb/^{238}U$ ages.

to define two age groups. Seventeen spot dates from the mantles and neoblasts vary from 529 ± 13 Ma (1σ) to 508 ± 8 Ma (1σ), and their weighted mean $^{206}Pb/^{238}U$ age is 515 ± 4 Ma (*t*σ; MSWD = 0.82; Figure II-14b). The Th/U ratios of this zircon are in the range 0.05–0.37, with a median value of 0.07. On the other hand, the youngest six spot dates from neoblasts range from 503 ± 8 Ma (1σ) to 488 ± 18 Ma (1σ), and yield a weighted mean $^{206}Pb/^{238}U$ age of 498 ± 11 Ma (*t*σ; MSWD = 0.36; Figure II-14c). The Th/U ratios of this zircon are in the range 0.00–0.60 (0.22 for median value) except for a spot 22.1.

DISCUSSION

The *P–T* evolution of the Lanterman Range eclogite is typified by three distinct episodes: (a) M_1 and M_2 represent the progressive first-stage subduction taking place at eclogite facies conditions; (b) M_3 corresponds to the second-stage subduction which caused one or two pulses of grossular-rich garnet overgrowth and finally (c) M_4 is assigned to the sub-solidus decompression to (lower–)middle crustal depths (Figures II-9 and II-10). In the following sections, I first discuss tectonometamorphic evolution of the Lanterman Range eclogite based on *P–T* estimations for individual episodes, M_1–M_4, and then compare the petrological and geochronological results with those of previous studies to discuss on their bearing for the subduction zone processes.

P–T evolution of the Lanterman Range eclogite

The prograde *P–T* path of the barroisite eclogites consists of two segments: $M_{1–2}$ followed by M_3 (Figure II-10). The evidence for pre-M_1 recrystallization is scarce but hinted by the presence of relict albite and titanite together with intergrown paragonite–Mg-pargasite in the garnet core (Figure II-3d). The *P–T* conditions of M_1 were estimated at ~15–20 kbar and 520–570 °C, primarily based on the *P–T* pseudosection together with compositional isopleths of the M_1 garnet (Figure II-10b); this result is consistent with the occurrence of hydrous mineral inclusions such as barroisite/Mg-pargasite, epidote and paragonite (e.g. de Sigoyer et al., 1997; Massonne and Kopp, 2005; Poli, 1993; Schmidt and Poli, 1998). The M_2 assemblage consists of anhydrous phases except for barroisite and minor phengite, representing post-M_1 burial and heating at ~22–25 kbar and 630–650 °C (Figure II-10d). The latter is corroborated by temperatures estimated from the Zr-in-rutile thermometry (e.g. Miller et al., 2007; Zack et al., 2002; Zhang et al., 2009). Taken together, the M_1 and M_2 assemblages represent a prograde *P–T* path associated with the first-stage subduction to ~50–65 km and ~70–80 km depths respectively.

A zoning pattern of garnet typified by the outward decrease in Ca/Mg ratio such as the M_2 garnet (Figure II-4) has been reported from many eclogite occurrences, including the Lanterman Range of NVL, Antarctica (Di Vincenzo et al., 2016) as well as other medium-*T*/high-*P* terranes such as Tso Morari, Himalaya (e.g. de Sigoyer et al., 1997; Konrad-

Schmolke et al., 2008; St-Onge et al., 2013), Dabie–Sulu belt, China (e.g. Wang et al., 1992; Zhang et al., 2005) and other orogens (e.g. Krogh, 1982; O'Brien, 1997; Page et al., 2007; Štípská and Powell, 2005). These medium-*T* eclogites consist of garnet, omphacite, quartz/coesite and rutile together with variable amounts of kyanite, phengite, sodic-calcic amphibole and (clino-)zoisite/epidote. The outward depletion of grossular in outer domains of garnet has been attributed to prograde growth under the eclogite facies conditions (e.g. Konrad-Schmolke et al., 2008; O'Brien, 1997). In particular, this zonal pattern is accounted for by the change in major reactants from calcic (epidote and Mg-pargasite of M_1) to sodic-calcic (barroisite of M_2) phases during the prograde metamorphism (e.g. Konrad-Schmolke et al., 2008).

The second stage of prograde evolution in the Lanterman Range eclogite is represented by the M_{3B} garnet growth at ~26 ± 3 kbar and 720 ± 80 °C, indicating further burial or subduction to ~85–95 km depths (Figure II-10d). Although the *P*–*T* conditions and dehydration reactions responsible for the M_2 and M_{3B} garnet growth are identical within uncertainties, both episodes are most likely intervened by a separate episode M_{3A} accompanying the disequilibrium growth of garnet (Figure II-4b). The *P*–*T* results of the $M_{1–2}$ and M_3 trajectories of barroisite eclogites attest to low thermal gradients (~5–10 °C /km) typical for a cold, thus fast subduction (Agard et al., 2009; Ernst, 2001). The apparent increase in average thermal gradient from ~5–7 °C /km (M_1–M_2) to ~7–10 °C/km (M_2–M_3) is accounted

for either by a decrease in the subduction rate (e.g. Brown, 2007; Groppo et al., 2009; Groppo and Castelli, 2010) or thermal relaxation, possibly related to the docking of a relatively buoyant crustal block (Bowers Terrane) onto the Wilson Terrane after the inter-terrane ocean closure (e.g. Groppo et al., 2009; Rosenbaum et al., 2002). Alternatively, the M_2–M_3 evolution could be a product of recycled subduction and exhumation at the convergent margin (e.g. Kabir and Takasu, 2010; Li and Gerya, 2009; Liati et al., 2016; Rubatto et al., 2011; Stöckhert and Gerya, 2005).

Retrograde evolution along the $M_{3–4}$ path was not studied in detail simply because I focused on prograde assemblages of the barroisite eclogite. Nevertheless, the maximum pressure of the M_4 was estimated to be lower than ~11 kbar on the basis of the jadeite content of vermicular diopside in symplectites (Figure II-9). Local occurrences of epidote xenoblasts associated with thin fractures are indicative of metasomatic replacement of eclogitic minerals governed by limited fluid infiltration (e.g. Massonne, 2012). In addition, no evidence for melting is apparent in the barroisite eclogite, suggesting that M_4 took place below the wet solidus curve of basalt/gabbro (Figure II-10d; Lambert and Wyllie, 1972).

The prograde M_1–M_3 path of the barroisite eclogites is compatible with that of the ‘tepid’ eclogite (Di Vincenzo et al., 2016). In particular, the quartz-stable M_2 and M_{3B} conditions are apparently similar to the peak conditions of ~17–24 kbar and 700 °C, estimated by Di Vincenzo et al. (2016). The ‘tepid’ eclogite and my barroisite eclogite samples share similar

petrological features: (a) the similar trend in Ca/Mg ratios of garnet correlatable among individual metamorphic domains of different textural types (Figure II-4); (b) the presence of barroisite at the peak stage and (c) the Zr content of rutile. On the other hand, the 'hot' eclogite only records the retrograde *P*–*T* evolution; the X_{Fe} values of garnet increase towards the rim (Di Vincenzo et al., 1997). Previous studies further envisaged different *P*–*T* evolution histories between high-*P* mafic blocks and garnet–phengite-bearing pelitic schists/gneisses in the Lanterman Range, primarily on the basis of the absence or presence of decompressional melting product (Di Vincenzo et al., 1997; Palmeri et al., 2003). Such a variation in *P*–*T* paths of individual high-*P* lithologies would be attributable to the corner flow in the mantle wedge yielding different depths for the return and final emplacement (e.g. Stöckhert and Gerya, 2005). Multiple burial-exhumation modes in the subduction channel, together with the absence of arc granitoids (Talarico et al., 1998) as well as variable geochemical affinities of high-*P* mafic blocks in the Lanterman Range (Di Vincenzo et al., 1997, 2016), may support the tectonic mélange model of Ricci and Tessensohn (2003).

Episodic zircon growth and cyclic subduction-exhumation

The SHRIMP geochronology of metamorphic zircon from the barroisite eclogite yielded apparent $^{206}Pb/^{238}U$ spot dates ranging from 529 ± 13 Ma (1σ) to 488 ± 18 Ma (1σ). A similar age range (*c.* 530–500 Ma) of zircon lacking in a negative Eu anomaly and heavy rare earth elements has

been recently reported from the 'tepid' eclogite (Di Vincenzo et al., 2016). It is thus likely that the Lanterman Range eclogite has undergone metamorphic growth and/or recrystallization at eclogite facies conditions during the middle to late Cambrian (Di Vincenzo et al., 1997, 2016). A 'protracted' zircon recrystallization under eclogite facies conditions was further proposed on the basis of the *c.* 30 Ma age range of zircon by Di Vincenzo et al. (2016). The timing and duration of eclogite facies metamorphism could vary at different settings in a single orogen (e.g. Fotoohi Rad et al., 2005; McClelland et al., 2006), and in particular, recent studies based on high-precision U-Pb zircon and Lu-Hf garnet geochronology revealed a wide range of mineral ages, leading to the suggestion that high- to ultrahigh-*P* metamorphism could be long-lived for several tens of million years (Cheng et al., 2016; Hacker et al., 2006; Lapen et al., 2003; Liu et al., 2006; Mattinson et al., 2006; McClelland et al., 2006; Wan et al., 2005; Zhang et al., 2010). The barroisite eclogites underwent a limited retrogression and preserve distinctive zones in zircon grains, which yielded two statistically different $^{206}Pb/^{238}U$ ages of 515 ± 4 Ma ($t\sigma$) and 498 ± 11 Ma ($t\sigma$) for the mantle and rim domains respectively. Thus, I suggest that: (a) the metamorphic zircon growth and/or recrystallization in the eclogite took place episodically at two distinct stages rather than continuously for a prolonged period of *c.* 15–30 Ma and (b) mantle-rim overgrowth domains of zircon are most likely related to the $M_{1–2}$ and M_3, that is, two discrete events of subduction burial. This temporal scheme of

the Lanterman Range eclogite is broadly consistent with the major pulses of pre- to syn-collisional calcalkaline granitoid emplacement (*c.* 520–490 Ma for the Granite Harbour Intrusives; Allibone and Wysoczanski, 2002; Bomparola et al., 2007; Giacomini et al., 2007) and the maximum depositional ages (*c.* 600–530 Ma) of the Wilson metasedimentary rocks (Adams et al., 2014; Estrada et al., 2016; Gibson et al., 2011; Kim et al., 2017; Paulsen et al., 2016; Rocchi et al., Vezzoni, 2015). The timing of younger, peak eclogite facies metamorphism (*c.* 500 Ma) suggests that the final closure of an intervening ocean between the Wilson and Bowers terranes took place in the late Cambrian (e.g. Crispini et al., 2007; Di Vincenzo et al., 1997, 2014; Kleinschmidt and Tessensohn, 1987; Rocchi et al., 2011).

Two distinctive age populations of episodically grown high-*P* zircon permit to calculate an average burial rate during the prograde evolution of barroisite eclogites. The *c.* 15 Ma time gap between the M_2 and M_3 gave a vertical burial rate of <2 mm/year. Such a slow rate of subduction, however, is incompatible with calculated thermal gradient (~5–10 °C/km) and theoretical perspective that a long residence time (>15 Ma) at mantle depths would easily trigger partial melting (cf. Anderson, 2007; Penniston-Dorland et al., 2015). The apparent longevity of high-*P* metamorphism is better accounted for by multiple subduction-exhumation cycles; the so-called yo-yo tectonics within *c.* 10–20 Ma time frames that have been envisaged in ancient convergent margins such as the Sanbagawa belt, Japan (Kabir and

Takasu, 2010) and western Alps, Italy (Liati et al., 2016; Rubatto et al., 2011), and numerical-modelling studies as well (e.g. Li and Gerya, 2009; Stöckhert and Gerya, 2005). Therefore, I suggest that a transient exhumation took place between the first- ($M_{1–2}$) and the second-stage (M_3) burials in the Lanterman Range, Antarctica; as a corollary, a quasi-continuous subduction or a protracted residence of pristine eclogite block at the mantle depths is unlikely (cf. Di Vincenzo et al., 2016).

CONCLUSIONS

I determined a quantitative *P–T* path in the eclogite facies field, where epidote and sodic-calcic amphibole are stable, from the barroisite eclogites in the Lanterman Range, NVL, Antarctica. The prograde *P–T* evolution consisting of three metamorphic stages (M_1–M_3) attests to low thermal gradient (~5–10 °C/km), suggesting that the cold subduction regime governed the Cambrian suture zone. The prograde *P–T* path is consistent with that of the 'tepid' eclogite determined by Di Vincenzo et al. (2016) but incompatible with the retrograde path of the 'hot' eclogite (Di Vincenzo et al., 1997). The prograde segments, $M_{1–2}$ and M_3, represent two distinctive stages of burial dated at 515 ± 4 Ma ($t\sigma$) and 498 ± 11 Ma ($t\sigma$) respectively. Thus, zircon growth at high pressures was episodic and most likely linked to two distinct subduction episodes. The times of eclogite facies metamorphism are broadly coeval with the *c.* 520–490 Ma arc magmatism and the *c.* 530 Ma cessation of sedimentary deposition in the Wilson

Terrane, linked to the accretion of the Bowers Terrane onto the Wilson Terrane, NVL. Because an average burial rate (<2 mm/year) estimated for the M_2–M_3 progression is unrealistically low for eclogites, an interim exhumation stage is most likely to be present during the prolonged subduction regime. Taken together, I suggest that the eclogites in the Lanterman Range of the Ross orogen have experienced two cycles of subduction and exhumation during the Cambrian.

REFERENCES

Adams, C.J., Bradshaw, J.D., & Ireland, T.R. (2014). Provenance connections between late Neoproterozoic and early Palaeozoic sedimentary basins of the Ross Sea region, Antarctica, south-east Australia and southern Zealandia. *Antarctic Science*, 26, 173–182.

Agard, P., Yamato, P., Jolivet, L., & Burov, E. (2009). Exhumation of oceanic blueschists and eclogites in subduction zones: Timing and mechanisms. *Earth-Science Reviews*, 92, 53–79.

Ahn, J.H., Peacor, D.R., & Essene, E.J. (1985). Coexisting paragonite–phengite in blueschist eclogite: a TEM study. *American Mineralogist*, 70, 1193–1204.

Allibone, A., & Wysoczanski, R. (2002). Initiation of magmatism during the Cambrian–Ordovician Ross orogeny in southern Victoria Land, Antarctica. *Geological Society of America Bulletin*, 114, 1007–1018.

Anderson, D.L. (2007). *New theory of the earth*. New York, NY: Cambridge University Press. 384 pp.

Bacon, C.R. (1989). Crystallization of accessory phases in magmas by local saturation adjacent to phenocrysts. *Geochimica et Cosmochimica Acta*, 53, 1055–1066.

Baldwin, J.A., Powell, R., Brown, M., Moraes, R., & Fuck, R.A. (2005). Modelling of mineral equilibria in ultrahigh-temperature metamorphic

rocks from the Anápolis-Itauçu Complex, central Brazil. *Journal of Metamorphic Geology*, 23, 511–531.

Baldwin, S.L., Monteleone, B.D., Webb, L.E., Fitzgerald, P.G., Grove, M., & Hill, E.J. (2004). Pliocene eclogite exhumation at plate tectonic rates in eastern Papua New Guinea. *Nature*, 431, 263–267.

Bebout, G.E. (2007). Metamorphic chemical geodynamics of subduction zones. *Earth and Planetary Science Letters*, 260, 373–393.

Bingen, B., Austrheim, H., Whitehouse, M.J., & Davis, W.J. (2004). Trace element signature and U–Pb geochronology of eclogite-facies zircon, Bergen Arcs, Caledonides of W Norway. *Contributions to Mineralogy and Petrology*, 147, 671–683.

Boger, S.D. (2011). Antarctica – Before and after Gondwana. *Gondwana Research*, 19, 335–371.

Bomparola, R.M., Ghezzo, C., Belousova, E., Griffin, W.L., & O'Reilly, S.Y. (2007). Resetting of the U–Pb zircon system in Cambro-Ordovician intrusives of the Deep Freeze Range, Northern Victoria Land, Antarctica. *Journal of Petrology*, 48, 327–364.

Borg, S.G., & Stump, E. (1987). Paleozoic magmatism and associated tectonic problems of northern Victoria Land, Antarctica. In G.D. McKenzie (Ed.), *Gondwana six: Structure, tectonics and geophysics.* American Geophysical Union (AGU) Geophysical Monograph Series (vol. 40, pp. 67–75). Washington, DC: AGU.

Bradshaw, J.D., & Laird, M.G. (1983). Pre-Beacon geology of northern Victoria Land: A review. In R.L. Oliver, P.R. James, & J.B. Jago (Eds.), *Antarctic earth sciences* (pp. 98–101). Canberra: Australian Academy of Science.

Brown, M. (2007). Metamorphic conditions in orogenic belts: A record of secular change. *International Geology Review*, 49, 193–234.

Capponi, G., Castelli, D., Fioretti, A.M., & Oggiano, G. (1997). Geological mapping and field relationships of eclogites from the Lanterman Range (Northern Victoria Land, Antarctica). In C.A. Ricci (Ed.), *The Antarctic region: Geological evolution and processes* (pp. 219–225). Siena: Terra Antartica Publication.

Capponi, G., Crispini, L., & Meccheri, M. (1999). Structural history and tectonic evolution of the boundary between the Wilson and Bowers terranes, Lanterman Range, northern Victoria Land, Antarctica. *Tectonophysics*, 312, 249–266.

Carswell, D.A. (1990). *Eclogite facies rocks.* New York, NY: Chapman & Hall. 396 pp.

Castro, A.E., & Spear, F.S. (2017). Reaction overstepping and re-evaluation of peak P–T conditions of the blueschist unit Sifnos, Greece: implications for the Cyclades subduction zone. *International Geology Review*, 59, 548–562.

Cawood, P.A. (2005). Terra Australis Orogen: Rodinia breakup and development of the Pacific and Iapetus margins of Gondwana during the Neoproterozoic and Paleozoic. *Earth-Science Reviews*, 69, 249–279.

Chen, Y., Ye, K., Wu, T.F., & Guo, S. (2013). Exhumation of oceanic eclogites: thermodynamic constraints on pressure, temperature, bulk composition and density. *Journal of Metamorphic Geology*, 31, 549–570.

Cheng, H., Liu, X.C., Vervoort, J.D., Wilford, D., & Cao, D.D. (2016). Micro-sampling Lu–Hf geochronology reveals episodic garnet growth and multiple high-*P* metamorphic events. *Journal of Metamorphic Geology*, 34, 336–377.

Cheong, W., Cho, M., & Kim, Y. (2013). An efficient method for zircon separation using the gold pan. *Journal of the Petrological Society of Korea*, 22, 63–70 (in Korean with English abstract).

Chernoff, C.B., & Carlson, W.D. (1997). Disequilibrium for Ca during growth of pelitic garnet. *Journal of Metamorphic Geology*, 15, 421–438.

Chopin, C. (1984). Coesite and pure pyrope in high-grade blueschists of the Western Alps: a first record and some consequences. *Contributions to Mineralogy and Petrology*, 86, 107–118.

Chopin, C. (2003). Ultrahigh-pressure metamorphism: tracing continental crust into the mantle. *Earth and Planetary Science Letters*, 212, 1–14.

Claoué-Long, J.C., Compston, W., Roberts, J., & Fanning, C.M. (1995). Two Carboniferous ages: A comparison of SHRIMP zircon dating with conventional zircon ages and $^{40}Ar/^{39}Ar$ analysis. In W.A. Berggren, D.V.

Kent, M.-P. Aubry, & J. Hardenbol (Eds.), *Geochronology, time scales and global stratigraphic correlation*, Society for Sedimentary Geology (SEPM) Special Publication (vol. 54(4), pp. 3–21). Tulsa, OK.: SEPM.

Coggon, R., & Holland, T.J.B. (2002). Mixing properties of phengitic micas and revised garnet-phengite thermobarometers. *Journal of Metamorphic Geology*, 20, 683–696.

Cottrell, E., & Kelly, K.A. (2011). The oxidation state of Fe in MORB glasses and the oxygen fugacity of the upper mantle. *Earth and Planetary Science Letters*, 305, 270–282.

Crispini, L., Di Vincenzo, G., & Palmeri, R. (2007). Petrology and ^{40}Ar–^{39}Ar dating of shear zones in the Lanterman Range (northern Victoria Land, Antarctica): implications for the metamorphic and temporal evolution at terrane boundaries. *Mineralogy and Petrology*, 89, 217–249.

Cumming, G.L., & Richards, J.R. (1975). Ore lead isotope ratios in a continuously changing earth. *Earth and Planetary Science Letters*, 28, 155–171.

Dallmeyer, R.D., & Wright, T.O. (1992). Diachronous cleavage development in the Robertson Bay terrane, Northern Victoria Land, Antarctica: Tectonic implications. *Tectonics*, 11, 437–448.

de Capitani, C., & Petrakakis, K. (2010). The computation of equilibrium assemblage diagrams with Theriak/Domino software. *American Mineralogist*, 95, 1006–1016.

de Sigoyer, J., Guillot, S., Lardeaux, J.M., & Mascle, G. (1997). Glaucophane-bearing eclogites in the Tso Morari dome (eastern Ladakh, NW Himalaya). *European Journal of Mineralogy*, 9, 1073–1083.

Desmons, J., & Smulikowski, W. (2007). A systematic nomenclature for metamorphic rocks: 4. High P/T metamorphic rocks. *Recommendations by the IUGS Subcommission on the Systematics of Metamorphic Rocks*. Recommendations, web version of 01.02.2007 (https://www.bgs.ac.uk/scmr/products.html).

Diener, J.F.A., & Powell, R. (2012). Revised activity–composition models for clinopyroxene and amphibole. *Journal of Metamorphic Geology*, 30, 131–142.

Di Vincenzo, G., Ghiribelli, B., Giorgetti, G., & Palmeri, R. (2001). Evidence of a close link between petrology and isotope records: constraints from SEM, EMP, TEM and in situ ^{40}Ar–^{39}Ar laser analyses on multiple generations of white micas (Lanterman Range, Antarctica). *Earth and Planetary Science Letters*, 192, 398–405.

Di Vincenzo, G., Grande, A., & Rossetti, F. (2014). Paleozoic siliciclastic rocks from northern Victoria Land (Antarctica): Provenance, timing of deformation, and implications for the Antarctica-Australia connection. *Geological Society of America Bulletin*, 126, 1416–1438.

Di Vincenzo, G., Horton, F., & Palmeri, R. (2016). Protracted (~30 Ma) eclogite-facies metamorphism in northern Victoria Land (Antarctica): Implications for the geodynamics of the Ross/Delamerian Orogen. *Gondwana Research*, 40, 91–106.

Di Vincenzo, G., & Palmeri, R. (2001). An ^{40}Ar–^{39}Ar investigation of high-pressure metamorphism and the retrogressive history of mafic eclogites from the Lanterman Range (Antarctica): evidence against a simple temperature control on argon transport in amphibole. *Contributions to Mineralogy and Petrology*, 141, 15–35.

Di Vincenzo, G., Palmeri, R., Talarico, F., Andriessen, P.A., & Ricci, C.A. (1997). Petrology and geochronology of eclogites from the Lanterman Range, Antarctica. *Journal of Petrology*, 38, 1391–1417.

Du, J.X., Zhang, L.F., Bader, T., Chen, Z.Y., & Lü, Z. (2014). Metamorphic evolution of relict lawsonite-bearing eclogites from the (U) HP metamorphic belt in the Chinese southwestern Tianshan. *Journal of Metamorphic Geology*, 32, 575–598.

Duchêne, S., Blichert-Toft, J., Luais, B., Télouk, P., Lardeaux, J.-M., & Albarède, F. (1997). The Lu–Hf dating of garnets and the ages of the Alpine high-pressure metamorphism. *Nature*, 387, 586–589.

Engi, M. (2017). Petrochronology based on REE-minerals: Monazite, allanite, xenotime, apatite. In M.J. Kohn, M. Engi, & P. Lanari (Eds.), *Petrochrnology: Methods and applications*, Reviews in Mineralogy and Geochemistry (v. 83, pp. 365–418). Chantilly, VA: The Mineralogical Society of America.

Ernst, W.G. (2001). Subduction, ultrahigh-pressure metamorphism, and regurgitation of buoyant crustal slices — implications for arcs and continental growth. *Physics of the Earth and Planetary Interiors*, 127, 253–275.

Ernst, W.G., Maruyama, S., & Wallis, S. (1997). Buoyancy-driven, rapid exhumation of ultrahigh-pressure metamorphosed continental crust. *Proceedings of the National Academy of Sciences of the United States of America*, 94, 9532–9537.

Essene, E.M. (1989). The current status of thermobarometry in metamorphic rocks. In J.S. Daly, R. Cliff, & B.W.D. Yardley (Eds.), *Evolution of metamorphic belts*, Geological Society, London, Special Publications (vol. 43, pp. 1–44). London: The Geological Society of London.

Estrada, S., Läufer, A., Eckelmann, K., Hofmann, M., Gärtner, A., & Linnemann, U. (2016). Continuous Neoproterozoic to Ordovician sedimentation at the East Gondwana margin – Implications from detrital zircons of the Ross Orogen in northern Victoria Land, Antarctica. *Gondwana Research*, 37, 426–448.

Federico, L., Crispini, L., & Capponi, G. (2010). Fault–slip analysis and transpressional tectonics: A study of Paleozoic structures in northern Victoria Land, Antarctica. *Journal of Structural Geology*, 32, 667–684.

Field, B.D., & Findlay, R.H. (1983). The sedimentology of the Robertson Bay Group, north Victoria Land. In R.L. Oliver, P.R. James, & J.B. Jago (Eds.), *Antarctic earth sciences* (pp. 102–106). Canberra: Australian Academy of Science.

Fotoohi Rad, G.R., Droop, G.T.R., Amini, S., & Moazzen, M. (2005). Eclogites and blueschists of the Sistan Suture Zone, eastern Iran: A comparison of *P–T* histories from a subduction mélange. *Lithos*, 84, 1–24.

Gaidies, F., de Capitani, C., & Abart, R. (2008). THERIA_G: a software program to numerically model prograde garnet growth. *Contributions to Mineralogy and Petrology*, 155, 657–671.

GANOVEX team (1987). *German Antarctic North Victoria Land Expedition 1982/83: GANOVEX III (vol. 2)*, edited by F. Tessensohn & N.W.

Roland, Geologisches Jahrbuch (vol. B66). Hannover: Bundesanstalt für Geowissenschaften und Rohstoffe. 324 pp.

Ghiribelli, B., Frezzotti, M.L., & Palmeri, R. (2002). Coesite in eclogites of the Lanterman Range (Antarctica): Evidence from textural and Raman studies. *European Journal of Mineralogy*, 14, 355–360.

Giacomini, F., Tiepolo, M., Dallai, L., & Ghezzo, C. (2007). On the onset and evolution of the Ross-orogeny magmatism in North Victoria Land — Antarctica. *Chemical Geology*, 240, 103–128.

Gibson, G.M., Morse, M.P., Ireland, T.R., & Nayak, G.K. (2011). Arc–continent collision and orogenesis in western Tasmanides: Insights from reactivated basement structures and formation of an ocean–continent transform boundary off western Tasmania. *Gondwana Research*, 19, 608–627.

Gilotti, J.A., Nutman, A.P., & Brueckner, H.K. (2004). Devonian to Carboniferous collision in the Greenland Caledonides: U-Pb zircon and Sm-Nd ages of high-pressure and ultrahigh-pressure metamorphism. *Contributions to Mineralogy and Petrology*, 148, 216–235.

Giorgetti, G., Tropper, P., Essene, E.J., & Peacor, D.R. (2000). Characterization of non-equilibrium and equilibrium occurrences of paragonite/muscovite intergrowths in an eclogite from the Sesia–Lanzo Zone (Western Alps, Italy). *Contributions to Mineralogy and Petrology*, 138, 326–336.

Glodny, J., Ring, U., Kühn, A., Gleissner, P., & Franz, G. (2005). Crystallization and very rapid exhumation of the youngest Alpine eclogites (Tauern Window, Eastern Alps) from Rb/Sr mineral assemblage analysis. *Contributions to Mineralogy and Petrology*, 149, 699–712.

Goodge, J.W., & Dallmeyer, R.D. (1996). Contrasting thermal evolution within the Ross orogen, Antarctica: evidence from mineral $^{40}Ar/^{39}Ar$ ages. *Journal of Geology*, 104, 435–458.

Green, E., Holland, T.J.B., & Powell, R. (2007). An order-disorder model for omphacitic pyroxenes in the system jadeite-diopside-hedenbergite-acmite, with applications to eclogitic rocks. *American Mineralogist*, 92, 1181–1189.

Groppo, C., Beltrando, M., & Compagnoni, R. (2009). The *P–T* path of the ultra-high pressure Lago Di Cignana and adjoining high-pressure meta-ophiolitic units: insights into the evolution of the subducting Tethyan slab. *Journal of Metamorphic Geology*, 27, 207–231.

Groppo, C., & Castelli, D. (2010). Prograde *P–T* evolution of a lawsonite eclogite from the Monviso meta-ophiolite (Western Alps): Dehydration and redox reactions during subduction of oceanic FeTi-oxide gabbro. *Journal of Petrology*, 51, 2489–2514.

Hacker, B.R., Ratschbacher, L., Webb, L., Ireland, T., Walker, D., & Shuwen, D. (1998). U/Pb zircon ages constrain the architecture of the ultrahigh-pressure Qinling–Dabie Orogen, China. *Earth and Planetary Science Letters*, 161, 215–230.

Hacker, B.R., Wallis, S.R., Ratschbacher, L., Grove, M., & Gehrels, G. (2006). High-temperature geochronology constraints on the tectonic history and architecture of the ultrahigh-pressure Dabie-Sulu Orogen. *Tectonics*, 25, TC5006.

Holland, T., Baker, J., & Powell, R. (1998). Mixing properties and activity-composition and relationships of chlorites in the system MgO-FeO-Al_2O_3-SiO_2-H_2O. *European Journal of Mineralogy*, 10, 395–406.

Holland, T.J.B. (1980). The reaction albite = jadeite + quartz determined experimentally in the range 600–1200 °C. *American Mineralogist*, 65, 129–134.

Holland T.J.B. (1983). The experimental determination of activities in disordered and short-range ordered jadeitic pyroxenes. *Contributions to Mineralogy and Petrology*, 82, 214–220.

Holland, T.J.B., & Powell, R. (1998). An internally consistent data set for phases of petrological interest. *Journal of Metamorphic Geology*, 16, 309–343.

Holland, T.J.B., & Powell, R. (2011). An improved and extended internally consistent thermodynamic dataset for phases of petrological interest, involving a new equation of state for solids. *Journal of Metamorphic Geology*, 29, 333–383.

Inger, S., & Cliff, R.A. (1994). Timing of metamorphism in the Tauern Window, Eastern Alps: Rb–Sr ages and fabric formation. *Journal of Metamorphic Geology*, 12, 695–707.

Kabir, M.F., & Takasu, A. (2010). Evidence for multiple burial–partial exhumation cycles from the Onodani eclogites in the Sambagawa metamorphic belt, central Shikoku, Japan. *Journal of Metamorphic Geology*, 28, 873–893.

Kaneko, Y., Katayama, I., Yamamoto, H., Misawa, K., Ishikawa, M., Rehman, H.U., … Shiraishi, K. (2003). Timing of Himalayan ultrahigh-pressure metamorphism: sinking rate and subduction angle of the Indian continental crust beneath Asia. *Journal of Metamorphic Geology*, 21, 589–599.

Katayama, I., Parkinson, C.D., Okamoto, K., Nakajima, Y., & Maruyama, S. (2000). Supersilicic clinopyroxene and silica exsolution in UHPM eclogite and pelitic gneiss from the Kokchetav massif, Kazakhstan. *American Mineralogist*, 85, 1368–1374.

Kim, Y., & Cho, M. (2008). Two-stage growth of porphyroblastic biotite and garnet in the Barrovian metapelites of the Imjingang belt, central Korea. *Journal of Metamorphic Geology*, 26, 385–399.

Kim, Y., Kim, T., Lee, J.I., & Kim, S. J. (2017). SHRIMP U-Pb ages of zircon from banded gneisses and a leucocratic dyke in the Wilson Terrane, northern Victoria Land, Antarctica. *Journal of the Geological Society of Korea*, 53, 489–507 (in Korean with English abstract).

Kleinschmidt, G., Roland, N.W., & Schubert, W. (1984). The Metamorphic basement complex in the Mountaineer Range, North Victoria Land, Antarctica. In N.W. Roland (Ed.), *German Antarctic North Victoria Land Expedition 1982/83, GANOVEX III (vol. 1),* Geologisches Jahrbuch (vol. B60, pp. 213–251). Hannover: Bundesanstalt für Geowissenschaften und Rohstoffe.

Kleinschmidt, G., & Tessensohn, F. (1987). Early Paleozoic westward directed subduction at the Pacific margin of Antarctica. In G.D. McKenzie (Ed.), *Gondwana six: Structure, tectonics and geophysics.* American Geophysical Union (AGU) Geophysical Monograph Series (vol. 40, pp. 89–105). Washington, DC: AGU.

Kohn, M.J., Corrie, S.L., & Markley, C. (2015). The fall and rise of metamorphic zircon. *American Mineralogist*, 100, 897–908.

Konrad-Schmolke, M., O'Brien, P.J., de Capitani, C., & Carswell, D.A. (2008). Garnet growth at high- and ultra-high pressure conditions and the effect of element fractionation on mineral modes and composition. *Lithos*, 103, 309–332.

Krogh, E.J. (1982). Metamorphic evolution of Norwegian country-rock eclogites, as deduced from mineral inclusions and compositional zoning in garnets. *Lithos*, 15, 305–321.

Lambert, I.B., & Wyllie, P.J. (1972). Melting of gabbro (quartz eclogite) with excess water to 35 kilobars, with geological applications. *Journal of Geology*, 80, 693–708.

Lapen, T.J., Johnson, C.M., Baumgartner, L.P., Mahlen, N.J., Beard, B.L., & Amato, J.M. (2003). Burial rates during prograde metamorphism of an ultra-high-pressure terrane: an example from Lago di Cignana, western Alps, Italy. *Earth and Planetary Science Letters*, 215, 57–72.

Läufer, A., Lisker, F., & Phillips, G. (2011). Late Ross-orogenic deformation of basement rocks in the northern Deep Freeze Range, Victoria Land, Antarctica: the Lichen Hills Shear Zone. *Polarforschung*, 80, 60–70.

Leake, B.E., Woolley, A.R., Arps, C.E.S., Brich, W.D., Gilbert, M.C., Grice, J.D., ... Youzhi, G. (1997). Nomenclature of amphiboles: Report of the Subcommittee on amphiboles of the International Mineralogical Association Commission on New Minerals and Mineral Names. *European Journal of Mineralogy*, 9, 623–651.

Li, Z., & Gerya, T.V. (2009). Polyphase formation and exhumation of high- to ultrahigh-pressure rocks in continental subduction zone: Numerical modeling and application to the Sulu ultrahigh-pressure terrane in eastern China. *Journal of Geophysical Research*, 114, B09406.

Liati, A., & Gebauer, D. (1999). Constraining the prograde and retrograde *P-T-t* path of Eocene H*P* rocks by SHRIMP dating of different zircon domains: inferred rates of heating, burial, cooling and exhumation for central Rhodope, northern Greece. *Contributions to Mineralogy and Petrology*, 135, 340–354.

Liati, A., Theye, T., Fanning, C.M., Gebauer, D., & Rayner, N. (2016). Multiple subduction cycles in the Alpine orogeny, as recorded in single zircon crystals (Rhodope zone, Greece). *Gondwana Research*, 29, 199–207.

Liou, J.G., Zhang, R., Liu, F., Zhang, Z., & Ernst, W.G. (2012). Mineralogy, petrology, U-Pb geochronology, and geologic evolution of the Dabie-Sulu classic ultrahigh-pressure metamorphic terrane, East-Central China. *American Mineralogist*, 97, 1533–1543.

Lister, G.S., & Forster, M.A. (2016). White mica $^{40}Ar/^{39}Ar$ age spectra and the timing of multiple episodes of high-*P* metamorphic mineral growth in the Cycladic eclogite–blueschist belt, Syros, Aegean Sea, Greece. *Journal of Metamorphic Geology*, 34, 401–421.

Liu, D., Jian, P., Kröner, A., & Xu, S. (2006). Dating of prograde metamorphic events deciphered from episodic zircon growth in rocks of the Dabie–Sulu UHP complex, China. *Earth and Planetary Science Letters*, 250, 650–666.

Liu, F.L., & Liou, J.G. (2011). Zircon as the best mineral for *P–T*–time history of UHP metamorphism: A review on mineral inclusions and U–Pb SHRIMP ages of zircons from the Dabie–Sulu UHP rocks. *Journal of Asian Earth Sciences*, 40, 1–39.

Liu, J., Bohlen, S.R., & Ernst, W.G. (1996). Stability of hydrous phases in subducting oceanic crust. *Earth and Planetary Science Letters*, 143, 161–171.

Ludwig, K.R. (2008). *User's manual for Isoplot 3.6: A geochronological toolkit for Microsoft Excel*, Berkeley Geochronology Center Special Publication (no. 4). Berkeley: Berkeley Geochronology Center. 77 pp.

Massonne, H.-J. (2012). Formation of amphibole and clinozoisite–epidote in eclogite owing to fluid infiltration during exhumation in a subduction channel. *Journal of Petrology*, 53, 1969–1998.

Massonne, H.-J., & Kopp, J. (2005). A low-variance mineral assemblage with talc and phengite in an eclogite from the Saxonian Erzgebirge, central Europe, and its *P–T* evolution. *Journal of Petrology*, 46, 355–375.

Mattinson, C.G., Wooden, J.L., Liou, J.G., Bird, D.K., & Wu, C.L. (2006). Age and duration of eclogite-facies metamorphism, North Qaidam HP/UHP terrane, Western China. *American Journal of Science*, 306, 683–711.

McClelland, W.C., Power, S.E., Gilotti, J.A., Mazdab, F.K., & Wopenka, B. (2006). U-Pb SHRIMP geochronology and trace-element geochemistry of coesite-bearing zircons, North-East Greenland Caledonides. In B.R. Hacker, W.C. McClelland, & J.G. Liou (Eds.), *Ultrahigh-pressure metamorphism: Deep continental subduction*, Geological Society of America Special Paper (vol. 403, pp. 23–43). Boulder, CO.: The Geological Society of America.

Miller, C., Zanetti, A., Thöni, M., & Konzett, J. (2007). Eclogitisation of gabbroic rocks: Redistribution of trace elements and Zr in rutile thermometry in an Eo-Alpine subduction zone (Eastern Alps). *Chemical Geology*, 239, 96–123.

Morimoto, N., Fabries, J., Ferguson, A.K., Ginzburg, I.V., Ross, M., Seifert, F.A., ... Gottardi, G. (1988). Nomenclature of pyroxenes. *Mineralogical Magazine*, 52, 535–550.

Mysen, B., & Griffin, W.L. (1973). Pyroxene stoichiometry and the breakdown of omphacite. *American Mineralogist*, 58, 60–63.

Nakamura, D., & Hirajima, T. (2000). Granulite-facies overprinting of ultrahigh-pressure metamorphic rocks, northeastern Su-Lu region, eastern China. *Journal of Petrology*, 41, 563–582.

O'Brien, P.J. (1997). Garnet zoning and reaction textures in overprinted eclogites, Bohemian Massif, European Variscides: A record of their thermal history during exhumation. *Lithos*, 41, 119–133.

Paces, J.B., & Miller, J.D. (1993). Precise U-Pb ages of Duluth Complex and related mafic intrusions, northeastern Minnesota: Geochronological insights to physical, petrogenetic, paleomagnetic, and tectonomagmatic processes associated with the 1.1 Ga Midcontinent Rift system. *Journal of Geophysical Research*, 98, 13997–14013.

Page, F.Z., Armstrong, L.S., Essene, E.J., & Mukasa, S.B. (2007). Prograde and retrograde history of the Junction School eclogite, California, and

an evaluation of garnet–phengite–clinopyroxene thermobarometry: *Contributions to Mineralogy and Petrology*, 153, 533–555.

Palin, R.M., Reuber, G.S., White, R.W., Kaus, B.J.P., & Weller, O.M. (2017). Subduction metamorphism in the Himalayan ultrahigh-pressure Tso Morari massif: An integrated geodynamic and petrological modelling approach. *Earth and Planetary Science Letters*, 467, 108–119.

Palmeri, R., Frezzotti, M.L., Godard, G., & Davies, R.J. (2009). Pressure-induced incipient amorphization of α-quartz and transition to coesite in an eclogite from Antarctica: a first record and some consequences. *Journal of Metamorphic Geology*, 27, 685–705.

Palmeri, R., Ghiribelli, B., Ranalli, G., Talarico, F., & Ricci, C.A. (2007). Ultrahigh-pressure metamorphism and exhumation of garnet-bearing ultramafic rocks from the Lanterman Range (northern Victoria Land, Antarctica). *Journal of Metamorphic Geology*, 25, 225–243.

Palmeri, R., Ghiribelli, B., Talarico, F., & Ricci, C.A. (2003). Ultra-high pressure metamorphism in felsic rocks: the garnet-phengite gneisses and quartzites from the Lanterman Range, Antarctica. *European Journal of Mineralogy*, 15, 513–525.

Palmeri, R., Talarico, F.M., & Ricci, C.A. (2011). Ultrahigh-pressure metamorphism at the Lanterman Range (northern Victoria Land, Antarctica). *Geological Journal*, 46, 126–136.

Paulsen, T.S., Deering, C., Sliwinski, J., Bachmann, O., & Guillong, M. (2016). Detrital zircon ages from the Ross Supergroup, north Victoria Land, Antarctica: Implications for the tectonostratigraphic evolution of the Pacific-Gondwana margin. *Gondwana Research*, 35, 79–96.

Peacock, S.M. (1996). Thermal and petrologic structures of subduction zones. In J.P. Platt (Ed.), *Subduction: Top to bottom*. American Geophysical Union (AGU) Geophysical Monograph Series (vol. 96, pp. 119–133). Washington, DC: AGU.

Penniston-Dorland, S.C., Kohn, M.J., & Manning, C.E. (2015). The global range of subduction zone thermal structures from exhumed blueschists and eclogites: Rocks are hotter than models. *Earth and Planetary Science Letters*, 428, 243–254.

Poli, S. (1993). The amphibolite-eclogite transformation: an experimental study on basalt. *American Journal of Science*, 293, 1061–1107.

Ravna, E.J.K., & Paquin, J. (2003). Thermobarometric methodologies applicable to eclogites and garnet ultrabasites. In D.A. Carswell, & R. Compagnoni (Eds.), *Ultrahigh pressure metamorphism*, European Mineralogical Union Notes in Mineralogy (vol. 5, pp. 229–259). Budapest: Eötvös University Press.

Ravna, E.J.K., & Terry, M.P. (2004). Geothermobarometry of UHP and HP eclogites and schists – an evaluation of equilibria among garnet–clinopyroxene–kyanite–phengite–coesite/quartz. *Journal of Metamorphic Geology*, 22, 579–592.

Rebay, G., Powell, R., & Diener, J.F.A. (2010). Calculated phase equilibria for a MORB composition in a *P–T* range, 450–650 °C and 18–28 kbar: the stability of eclogite. *Journal of Metamorphic Geology*, 28, 635–645.

Ricci, C.A., Talarico, F., Palmeri, R., Di Vincenzo, G., & Pertusati, P.C. (1996). Eclogite at the Antarctic palaeo-Pacific active margin of Gondwana (Lanterman Range, northern Victoria Land, Antarctica). *Antarctic Science*, 8, 277–280.

Ricci, C.A., & Tessensohn, F. (2003). The Lanterman-Mariner suture: Antarctic evidence for active margin tectonics in Paleozoic Gondwana. In F. Tessensohn, & C.A. Ricci (Eds.), *Aspects of a suture zone: The Mariner Glacier area, Antarctica*, Geologisches Jahrbuch (vol. B85, pp. 305–332). Hannover: Bundesanstalt für Geowissenschaften und Rohstoffe.

Rocchi, S., Bracciali, L., Di Vincenzo, G., Gemelli, M., & Ghezzo, C. (2011). Arc accretion to the early Paleozoic Antarctic margin of Gondwana in Victoria Land. *Gondwana Research*, 19, 594–607.

Rocchi, S., Di Vincenzo, G., Dini, A., Petrelli, M., & Vezzoni, S. (2015). Time–space focused intrusion of genetically unrelated arc magmas in the early Paleozoic Ross–Delamerian Orogen (Morozumi Range, Antarctica). *Lithos*, 232, 84–99.

Roland, R.W., Gibson, G.M., Kleinschmidt, G., & Schubert, W. (1984). Metamorphism and structural relations of the Lanterman Metamorphics, North Victoria Land, Antarctica. In N.W. Roland (Ed.), *German*

Antarctic North Victoria Land Expedition 1982/83, GANOVEX III (vol. 1), Geologisches Jahrbuch (vol. B60, pp. 319–361). Hannover: Bundesanstalt für Geowissenschaften und Rohstoffe.

Root, D.B., Hacker, B.R., Mattinson, J.M., & Wooden, J.L. (2004). Zircon geochronology and ca. 400 Ma exhumation of Norwegian ultrahigh-pressure rocks: an ion microprobe and chemical abrasion study. *Earth and Planetary Science Letters*, 228, 325–342.

Rosenbaum, G., Lister, G.S., & Duboz, C. (2002). Relative motions of Africa, Iberia and Europe during Alpine orogeny. *Tectonophysics*, 359, 117–129.

Rubatto, D. (2002). Zircon trace element geochemistry: partitioning with garnet and the link between U–Pb ages and metamorphism. *Chemical Geology*, 184, 123–138.

Rubatto, D., Gebauer, D., & Compagnoni, R. (1999). Dating of eclogite-facies zircons: the age of Alpine metamorphism in the Sesia–Lanzo Zone (Western Alps). *Earth and Planetary Science Letters*, 167, 141–158.

Rubatto, D., & Hermann, J. (2003). Zircon formation during fluid circulation in eclogites (Monviso, Western Alps): implications for Zr and Hf budget in subduction zones. *Geochimica et Cosmochimica Acta*, 67, 2173–2187.

Rubatto, D., & Hermann, J. (2007). Experimental zircon/melt and zircon/garnet trace element partitioning and implications for the geochronology of crustal rocks. *Chemical Geology*, 241, 38–61.

Rubatto, D., Regis, D., Hermann, J., Boston, K., Engi, M., Beltrando, M., ... McAlpine, S.R.B. (2011). Yo-yo subduction recorded by accessory minerals in the Italian Western Alps. *Nature Geoscience*, 4, 338–342.

Rubie, D.C. (1990). Role of kinetics in the formation and preservation of eclogites. In D.A. Carswell (Ed.), *Eclogite facies rocks* (pp. 111–140). New York, NY: Chapman & Hall.

Ruffet, G., Gruau, M., Ballèvre, M., Féraud, G., & Philippot, P. (1997). Rb–Sr and ^{40}Ar–^{39}Ar laser probe dating of high-pressure phengites from the Sesia zone (Western Alps): underscoring of excess argon and new age

constraints on the high-pressure metamorphism. *Chemical Geology*, 141, 1–18.

Sawyer, E.W. (2008). *Atlas of migmatites*. The Canadian Mineralogist, Special Publication (vol. 9). Ontario: NRC Research Press. 371 pp.

Scherer, E.E., Cameron, K.L., & Blichert-Toft, J. (2000). Lu–Hf garnet geochronology: Closure temperature relative to the Sm–Nd system and the effects of trace mineral inclusions. *Geochimica et Cosmochimica Acta*, 64, 3413–3432.

Schmidt, M.W., & Poli, S. (1998). Experimentally based water budgets for dehydrating slabs and consequences for arc magma generation. *Earth and Planetary Science Letters*, 163, 361–379.

Smith, D.C. (1988). *Eclogites and eclogite-facies rocks*, Developments in Petrology (vol. 12). New York, NY: Elsevier. 524 pp.

Štípská, P., & Powell, R. (2005). Constraining the *P–T* path of a MORB-type eclogite using pseudosections, garnet zoning and garnet-clinopyroxene thermometry: an example from the Bohemian Massif. *Journal of Metamorphic Geology*, 23, 725–743.

Stöckhert, B., & Gerya, T.V. (2005). Pre-collisional high pressure metamorphism and nappe tectonics at active continental margins: A numerical simulation. *Terra Nova*, 17, 102–110.

St-Onge, M.R., Rayner, N., Palin, R.M., Searle, M.P., & Waters, D.J. (2013). Integrated pressure-temperature-time constraints for the Tso Morari dome (Northwest India): implications for the burial and exhumation path of UHP units in the western Himalaya. *Journal of Metamorphic Geology*, 31, 469–504.

Stump, E. (1995). *The Ross Orogen of the Transantarctic Mountains*, Cambridge: Cambridge University Press. 284 pp.

Talarico, F., Ghiribelli, B., Siddoway, C.S., Palmeri, R., & Ricci, C.A. (1998). The northern Victoria Land segment of the Antarctic paleo-Pacific margin of eastern Gondwana: new constraints from the Lanterman and Mountaineer Ranges. *Terra Antartica*, 5, 245–252.

Talarico, F.M., Palmeri, R., & Ricci, C.A. (2004). Regional metamorphism and P-T evolution of the Ross Orogen in northern Victoria Land (Antarctica): a review. *Periodico di Mineralogica*, 73, 185–196.

Tatsumi, Y. (1989). Migration of fluid phases and genesis of basalt magmas in subduction zones. *Journal of Geophysical Research*, 94, 4697–4707.

Timmermann, H., Štědrá, V., Gerdes, A., Noble, S.R., Parrish, R.R., & Dörr, W. (2004). The problem of dating high-pressure metamorphism: a U–Pb isotope and geochemical study on eclogites and related rocks of the Mariánské Lázně Complex, Czech Republic. *Journal of Petrology*, 45, 1311–1338.

Tomaschek, F., Kennedy, A.K., Villa, I.M., Lagos, M., & Ballhaus, C. (2003). Zircons from Syros, Cyclades, Greece—recrystallization and mobilization of zircon during high-pressure metamorphism. *Journal of Petrology*, 44, 1977–2002.

Tomkins, H.S., Powell, R., & Ellis, D.J. (2007). The pressure dependence of the zirconium-in-rutile thermometer. *Journal of Metamorphic Geology*, 25, 703–713.

Tsujimori, T., Sisson, V.B., Liou, J.G., Harlow, G.E., & Sorensen, S.S. (2006). Petrologic characterization of Guatemalan lawsonite eclogite: Eclogitization of subducted oceanic crust in a cold subduction zone. In B.R. Hacker, W.C. McClelland, & J.G. Liou (Eds.), *Ultrahigh-pressure metamorphism: Deep continental subduction*, Geological Society of America Special Paper (vol. 403, pp. 147–168). Boulder, CO.: The Geological Society of America.

Wan, Y., Li, R., Wilde, S.A., Liu, D., Chen, Z., Yan, L., ... Yin, X. (2005). UHP metamorphism and exhumation of the Dabie Orogen, China: Evidence from SHRIMP dating of zircon and monazite from a UHP granitic gneiss cobble from the Hefei Basin. *Geochimica et Cosmochimica Acta*, 69, 4333–4348.

Wang, X., Liou, J.G., & Maruyama, S. (1992). Coesite-bearing eclogites from the Dabie Mountains, central China: Petrogenesis, *P-T* Paths, and implications for regional tectonics. *Journal of Geology*, 100, 231–250.

Weaver, S.D., Bradshaw, J.D., & Laird, M.G. (1984). Geochemistry of Cambrian volcanics of the Bowers Supergroup and implications for the Early Palaeozoic tectonic evolution of northern Victoria Land, Antarctica. *Earth and Planetary Science Letters*, 68, 128–140.

Wei, C.J., & Clark, G.L. (2011). Calculated phase equilibria for MORB compositions: a reappraisal of the metamorphic evolution of lawsonite eclogite. *Journal of Metamorphic Geology*, 29, 939–952.

Weller, O.M., St-Onge, M.R., Rayner, N., Waters, D.J., Searle, M.P., & Palin, R.M. (2016). U–Pb zircon geochronology and phase equilibria modelling of a mafic eclogite from the Sumdo complex of south-east Tibet: Insights into prograde zircon growth and the assembly of the Tibetan plateau. *Lithos*, 262, 729–741.

White, R.W., Powell, R., & Holland, T.J.B. (2007). Progress relating to calculation of partial melting equilibria for metapelites. *Journal of Metamorphic Geology*, 25, 511–527.

White, R.W., Powell, R., Holland, T.J.B., & Worley, B.A. (2000). The effect of TiO_2 and Fe_2O_3 on metapelitic assemblages at greenschist and amphibolite facies conditions: mineral equilibria calculations in the system K_2O–FeO–MgO–Al_2O_3–SiO_2–H_2O–TiO_2–Fe_2O_3. *Journal of Metamorphic Geology*, 18, 497–511.

Whitney, D.L., & Evans, B.W. (2010). Abbreviations for names of rock-forming minerals. *American Mineralogist*, 95, 185–187.

Williams, I.S. (1998). U-Th-Pb geochronology by ion microprobe. In M.A. McKibben, W.C. Shanks III, & W.I. Ridley (Eds.), *Applications of microanalytical techniques to understanding mineralizing processes,* Reviews in Economic Geology (v. 7, pp. 1–35). Littleton, CO: Society of Economic Geologists.

Zack, T., Kronz, A., Foley, S.F., & Rivers, T. (2002). Trace element abundances in rutiles from eclogites and associated garnet mica schists. *Chemical Geology*, 184, 97–122.

Zack, T., Moraes, R., & Kronz, A. (2004). Temperature dependence of Zr in rutile: empirical calibration of a rutile thermometer. *Contributions to Mineralogy and Petrology*, 148, 471–488.

Zhang, J.X., Mattinson, C.G., Yu, S.Y., Li, J.P., & Meng, F.C. (2010). U–Pb zircon geochronology of coesite-bearing eclogites from the southern Dulan area of the North Qaidam UHP terrane, northwestern China: spatially and temporally extensive UHP metamorphism during continental subduction. *Journal of Metamorphic Geology*, 28, 955–978.

Zhang, R.Y., Iizuka, Y., Ernst, W.G., Liou, J.G., Xu, Z.Q., Tsujimori, T., ... Jahn, B.M. (2009). Metamorphic *P–T* conditions and thermal structure of Chinese Continental Scientific Drilling main hole eclogites: Fe–Mg partitioning thermometer *vs.* Zr-in-rutile thermometer. *Journal of Metamorphic Geology*, 27, 757–772.

Zhang, Z., Xiao, Y., Liu, F., Liou, J.G., & Hoefs, J. (2005). Petrogenesis of UHP metamorphic rocks from Qinglongshan, southern Sulu, east-central China. *Lithos*, 81, 189–207.

Zheng, Y.F. (2012). Metamorphic chemical geodynamics in continental subduction zones. *Chemical Geology*, 328, 5–48.

CHAPTER III

Mafic magmatism at *c.* 590 Ma in the Ross orogen, Antarctica: The Ediacaran missing link for continental rifting and detrital zircon source along the East Gondwana margin

ABSTRACT

Paleogeographic linkage between Australia and Antarctica has played a key role for reconstruction of the East Gondwana during the Neoproterozoic, but some uncertainties remain particularly for the presence of Ediacaran rifting event along the East Antarctic margin. In this study, I report the finding of such a rift-related mafic magmatism preserved in Cambrian eclogites of the Ross orogen in northern Victoria Land, Transantarctic Mountains. The inherited zircon core ages (591 ± 8 Ma and 603 ± 4 Ma, *t*σ) and mildly alkalic, within-plate to continental basalt-like geochemistry of the eclogites as well as adjacent metasedimentary rocks of dominantly siliciclastic composition suggest that their gabbroic protoliths should be a spatial-temporal equivalent to *c.* 600–580 Ma rift to passive margin magmatic rocks of the Tasmanides in eastern Australia. Concerning that the onset of the Ross orogeny in northern Victoria Land took place at early Cambrian (*c.* 540–530 Ma), my results are in contrast to the Cryogenian (*c.* 670–650 Ma) rifting followed by Ediacaran (*c.* 590–570 Ma) arc initiation. Taken together, I suggest two discrete tectonic inversion events along the Australian and Antarctic margins. These late Neoproterozoic continental rifting events might be responsible for the Pacific-Gondwana zircon population in the Paleozoic Gondwana 'mud-pile'.

Keywords: late Neoproterozoic rifting, igneous zircon ages, Ross orogen, Tasmanides, Pacific-Gondwana zircon, East Gondwana margin

INTRODUCTION

The paleo-continental margins of East Gondwana along the paleo-Pacific Ocean broadly shared common tectonic history during the Neoproterozoic (e.g. Cawood, 2005; Boger, 2011), and the Australia–Antarctica connection played a pivotal role in many paleogeographic reconstructions of the Rodinia supercontinent (Dalziel, 1991; Hoffman, 1991; Moores, 1991; Goodge et al., 2008). The Cryogenian–Ediacaran siliciclastic sedimentary sequences and rift-related igneous rocks in association with the post-Rodinia rifting are well preserved in the Delamerian and Thomson orogens of the Tasmanides, eastern Australia (Preiss, 2000; Fergusson et al., 2009), but these lithologies are hardly exposed in the coeval Ross orogen of the Transantarctic Mountains (TAM; Goodge et al., 2002, 2004). In particular, the Ediacaran (*c.* 600–580 Ma) rift-related lithology is so far unknown in the TAM. This absence led to a hypothesis for Ediacaran (*c.* 590–570 Ma) onset of the Ross orogeny in the TAM (Goodge et al., 2012; Hagen-Peter et al., 2016), which is problematic for correlation with *c.* 520–490 Ma Delamerian orogeny (e.g. Foden et al., 2006; Cooper et al., 2011).

The dearth of Neoproterozoic geological records in the TAM brought another issue regarding the source rocks of *c.* 700–500 Ma detrital Pacific-Gondwana zircon (Ireland et al., 1998; Sircombe, 1999; Martin et al., 2017). This zircon population is distinctive and widespread in the Cambrian to Triassic (meta)sedimentary strata of the Tasmanides (Figure III-1;

Figure III-1. Orogenic belts in the Australian-Antarctic continents, adapted from Boger (2011), Fergusson et al. (2017) and Martin et al. (2017). Blue (1,2) and green (3–6) circles denote the locales of available U-Pb zircon ages (in Ma) of the late Neoproterozoic rift-related magmatism in Antarctica and Australia, respectively. Blue star represents the location of eclogite sample from northern Victoria Land (NVL). Locations of the Tasman line (Fergusson et al., 2007) and the rift boundary of Antarctica (Goodge and Finn, 2010) are also shown. 1—Cotton Plateau gabbro, central Transantarctic Mountains (CTM; Goodge et al., 2002); 2—rhyolite clast of the Skelton group, southern Victoria Land (SVL; Cooper et al., 2011); 3—rhyodacite of the Togari group, western Tasmania (Calver et al., 2004); 4—intermediate sill of the Grassy group, King Island (Calver et al., 2004); 5—ash fall tuff of the Adelaide rift complex (A; Cox et al., 2018); 6—alkali rhyolite of the Koonenberry belt (KB; 6a, Crawford et al., 1997; 6b, Greenfield et al., 2011); B—Bowers terrane; C—Curnamona craton; D—Delamerian orogen; GSM—Gamburtsev Subglacial Mountains; GV—George V coast; K—Kuunga orogen; L—Lachland orogen; M—Mossman orogen; N—New England orogen; P-G—Pacific-Gondwanan; RB—Robertson Bay terrane; T—Thomson orogen; W—Wilson terrane.

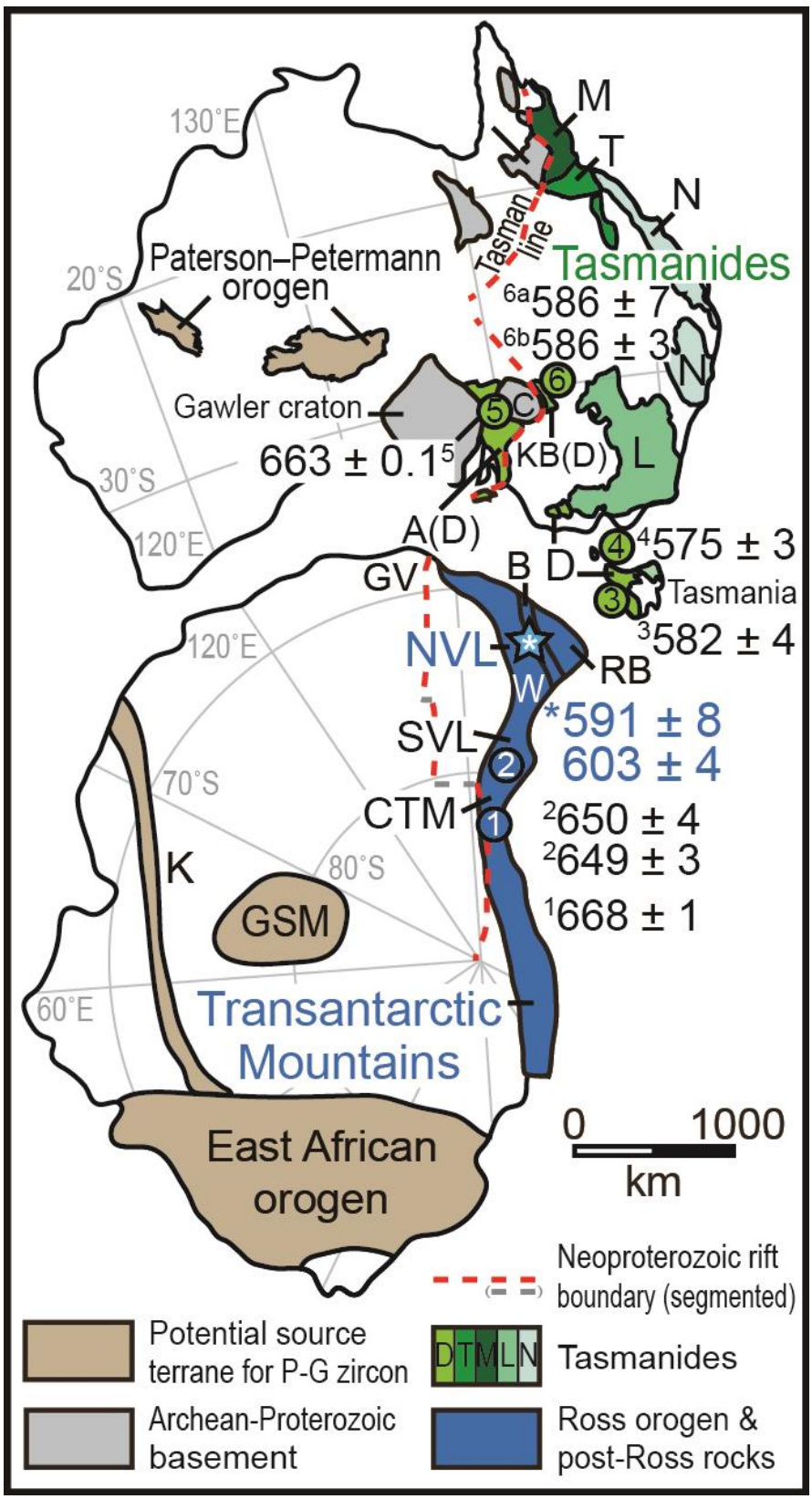
130°E
20°S
30°S
120°E
120°E
70°S
80°S
60°E
M
T
N
Tasman line
Tasmanides
Paterson–Petermann orogen
6a586 ± 7
6b586 ± 3
N
Gawler craton
5
C
6
663 ± 0.1[5]
K
KB(D)
L
A(D)
4575 ± 3
GV
B
D
4
Tasmania
3
3582 ± 4
NVL
RB
W
*591 ± 8
603 ± 4
SVL
2
CTM
1
2650 ± 4
2649 ± 3
1668 ± 1
K
GSM
Transantarctic Mountains
East African orogen
0
1000
km
Neoproterozoic rift boundary (segmented)
Potential source terrane for P-G zircon
DTMLN
Tasmanides
Archean-Proterozoic basement
Ross orogen & post-Ross rocks

Fergusson et al., 2017 and references therein) and their Antarctic equivalents along the TAM (Goodge et al., 2004; Elliot et al., 2015; Estrada et al., 2016; Paulsen et al., 2016; Kim et al., 2017). Primary sources for the Cambrian (*c.* 540–500 Ma) component of the population are most likely proximal igneous and metamorphic rocks of the Ross orogen, but those for the Neoproterozoic component remain controversial. Potential provenances may include: (1) ice-covered inboard arc of the early Ross age (e.g. Goodge et al., 2012; Fergusson et al., 2017; Glen et al., 2017); (2) East Antarctic craton region (e.g. Sircombe, 1999; Veevers and Saeed, 2008); (3) East African orogen (e.g. Squire et al., 2006); (4) Paterson orogen of western Australia (Martin et al., 2017); and (5) late Neoproterozoic rift system (e.g. Fergusson et al., 2007; Cooper et al., 2011).

In this study, I report the Ediacaran rift-related mafic magmatism in the Ross orogen for the first time to my knowledge, based on the whole-rock geochemistry and zircon U-Pb ages of eclogites in the Lanterman Range, northern Victoria Land (NVL), Antarctica (Figure III-1). I then discuss tectonic-sedimentary implications of my discovery: (1) regional correlation of these Ediacaran protoliths of the eclogites to rift-related equivalents in the Tasmanides; (2) diachronous rift-to-arc tectonic inversion events along the the East Gondwana margin; and (3) sedimentary provenance of the Pacific-Gondwana zircon population in the Paleozoic Gondwana ‘mud-pile’.

GEOLOGICAL BACKGROUND

The Paleozoic Delamerian, Thomson, Lachlan, Mossman and New England orogens in eastern Australia are collectively termed as the Tasmanides (Figure III-1; for example, Glen et al., 2017). The former two orogens together with the Ross orogen in the TAM culminated at the Cambrian to Ordovician, forming a branch of the gigantic, accretionary Terra Australis orogen along the paleo-Pacific Ocean (Cawood, 2005). The Ross orogen consists of central TAM, southern Victoria Land (SVL), and NVL (Figure III-1). NVL comprises three fault-bounded blocks of the Wilson, Bowers and Robertson Bay terranes from onshore to offshore (e.g. Weaver et al., 1984; Figure III-1). The Wilson terrane represents a continental arc complex primarily consisting of quartzofeldspathic metasedimentary rocks and syn- to post-orogenic plutons (Kleinschmidt and Tessensohn, 1987). The volcanic-sedimentary Bowers oceanic arc complex and the Robertson Bay turbiditic sequence accreted via the westward subduction during the Ross orogeny (e.g. Di Vincenzo et al., 2014). Along the suture boundary between the Wilson and Bowers terranes, a medium- to high-pressure belt is present and typified by the occurrence of eclogite-facies mafic–ultramafic rocks in the Lanterman Range (Di Vincenzo et al., 1997; Kim et al., 2019).

Geological and geochronological evidence for the Cryogenian rifting in the TAM is rare and fragmentary, only preserved in some siliciclastic successions and magmatic rocks of the Beardmore Group, CTM (*c.* 670 Ma;

Goodge et al., 2002, 2004) and the Skelton Group, SVL (*c.* 650 Ma; Cooper et al., 2011). but virtually absent in NVL. A series of Neoproterozoic continental rifting events are documented in the Adelaide rift complex of the Delamerian orogen, eastern Australia (Figure III-1; Preiss, 2000). The early stage of rifting, including mantle plume activities, was responsible for the formation of extensional basins and mafic dike swarms at *c.* 830–780 Ma (Wingate et al., 1998; Preiss, 2000; Holm et al., 2003). Continued extension of the rifted margin has evolved into passive margin sedimentation accompanied by intracontinental volcanism at *c.* 660 Ma (Preiss, 2000; Cox et al., 2018). The late stage rifting took place at *c.* 600–580 Ma and thick mafic lavas erupted along the eastern Australian margin (Figure III-1; Crawford et al., 1997; Direen and Crawford, 2003a; Gibson et al., 2015). This Ediacaran rifting together with thick siliciclastic deposition is also recognized in the Thomson orogen (Fergusson et al., 2009).

GEOCHEMICAL AND GEOCHRONOLOGICAL RESULTS

Sample description

The analyzed eclogite samples (E-1a and E-1c) were collected from the Lanterman Range (Figure III-1; Di Vincenzo et al., 1997; Kim et al., 2019), where the eclogites are commonly boudinaged and associated with phengite-bearing schists/gneisses. Mineral assemblages of the eclogite consist of garnet + omphacite + calcic/sodic-calcic amphibole + epidote +

phengite + paragonite + rutile + quartz; further details are available in Kim et al. (2019).

Whole-rock geochemistry

Major and trace elements concentrations of two eclogite samples were analyzed using the inductively-coupled plasma optical emission spectrometry and mass spectrometry, respectively, at the Actlabs (Ontario, Canada; Table III-1). The result is shown in Figure III-2, along with geochemical data of other Neoproterozoic rift/passive-margin igneous rocks in the TAM and Tasmanides. Both samples belong to the subalkaline basalt field in the Zr/TiO_2–Nb/Y diagram (Figure III-2a; Winchester and Floyd, 1977). Multi-element spider diagram of the samples, normalized to normal-mid ocean ridge basalt (N-MORB), show the enriched (E)-MORB-like trend as well as weak negative Nb and positive Ta anomalies (Figure III-2b). This result is compatible with the E-MORB to within-plate tholeiitic/volcanic arc basalt setting deduced from the Nb–Zr–Y discrimination diagram (Figure III-2c; Meschede, 1986), and the E-MORB to continental basalt setting from the Y–La–Nb diagram (Figure III-2d; Cabanis and Lecolle, 1989).

Zircon geochronology

Zircon grains were separated from an eclogite samples (E-1a and E-1c), using a conventional technique (Kim et al., 2019), and were mounted in

Table III-1. Whole-rock geochemistry of late Neoproterozoic rift-related mafic rocks along the Transantarctic Mountains and Tasmanides

	Northern Victoria Land (Transantarctic Mountains)		Southern Victoria Land (Transantarctic Mountains)				
	Lanterman Range (this study)		Skelton Group (Cooper et al., 2011)				
	eclogite		Baronick Formation metavolcanic rocks				
Major elements (wt%)	E-1a	E-1c	OU79842 Trachy-andesite	OU79847 Trachy-basalt	OU79856 Trachy-andesite	OU79868 Basalt	OU79876 Basalt
SiO_2	45.94	45.83	59.42	48.43	56.69	49.91	46.79
TiO_2	1.74	1.82	0.55	1.71	1.31	1.72	3.37
Al_2O_3	14.61	14.63	19.44	17.15	17.70	16.83	15.36
Fe_2O_3(T)	14.33	14.06	5.53	14.49	9.35	14.07	13.66
MnO	0.80	0.83	0.02	0.05	0.04	0.04	0.12
MgO	9.11	8.86	2.26	4.43	2.65	3.58	2.99
CaO	11.08	11.22	4.73	4.67	2.92	4.51	7.25
Na_2O	2.66	2.63	5.43	4.61	6.45	5.02	4.50
K_2O	0.10	0.06	0.78	1.21	1.06	1.53	1.22
P_2O_5	0.03	0.05	0.17	1.23	0.35	1.23	0.49
LOI	0.23	0.22	1.23	1.52	0.77	1.23	3.70
Total	100.60	100.20	99.56	99.50	99.29	99.67	99.45
Trace elements (ppm)							
Cs	< 0.5	< 0.5					

Rb	4	3	9.7	16.2	16.6	8.4	20.2
Ba	10	7	351.4	252.3	253.3	77.4	216.9
Th	4.4	5.7					
U	0.6	0.9					
K	837	504					
Nb	17	15	46.2	62.3	61.2	66	17.8
Ta	1.2	1.1	2.99	3.59	3.52	3.91	1.12
La	14	17.3	31.16	58.96	52.82	48.31	25.56
Ce	34.6	41.8	61.46	116.51	96.96	86.75	54.57
Pb	5	6					
Pr	4.01	4.82	7.15	14.24	11.19	9.48	7.33
Sr	105	123	492.5	400.8	481.7	188.4	418.7
P	131	221					
Nd	15.9	19.9	29.86	63.43	48.04	37.92	35.88
Zr	153	141	496.2	608	567	595.9	272.9
Hf	3.4	3	9.9	11.64	11.91	13.32	6.38
Sm	3.6	4.4	5.93	13.4	10.25	7.88	8.95
Eu	1.03	1.25	2	3.45	2.55	1.4	2.45
Ti	10430	10934	3047	9379	7254	2607	18546
Dy	6.6	6.9	4.36	10.88	10.44	7.97	9.01
Y	35	36	19.8	55.9	51.8	41.3	47.3
Ho	1.4	1.5	0.81	2.23	2.04	1.62	1.84
Er	3.8	4.1	2.13	5.87	5.62	4.62	4.93
Yb	3.9	3.6	2.18	5.62	5.8	5.12	4.15
Lu	0.57	0.56	0.3	0.8	0.81	0.73	0.59

Table III-1. Continued.

	Southern Victoria Land (Transantarctic Mountains)						
	Skelton Group (Cook, 2007)						
Major elements (wt%)	Highway Suite						
SiO_2	48.44	48.50	47.48	50.85	48.65	45.28	48.62
TiO_2	2.81	1.47	2.58	2.15	2.60	2.18	2.92
Al_2O_3	15.90	16.14	15.97	14.25	16.94	15.29	15.70
Fe_2O_3(T)	13.69	11.13	13.71	17.36	12.35	15.48	13.27
MnO	0.21	0.17	0.20	0.29	0.15	0.23	0.22
MgO	7.04	7.44	6.97	2.15	3.89	8.11	6.63
CaO	9.74	11.75	9.40	6.96	8.84	7.62	9.76
Na_2O	1.00	2.95	2.63	3.46	4.54	2.74	2.46
K_2O	0.78	0.28	0.71	1.35	1.57	2.66	0.04
P_2O_5	0.39	0.17	0.35	0.73	0.47	0.41	0.37
LOI				0.40			
Total	100.00	100.00	100.00	99.55	100.00	100.00	99.99
Trace elements (ppm)							
Cs							
Rb	11	18	19	56	32	65	0
Ba	137	165	242	470	254	286	15
Th							
U							

K							
Nb	15	14	13	17	27	25	13
Ta							
La	10	14	17	32	24	12	0
Ce	31	28	33	61	48	42	28
Pb	2	8	7	19	12	3	7
Pr							
Sr	390	367	433	882	687	470	402
P							
Nd	23	25	28	36	29	29	23
Zr	212	204	198	173	260	246	191
Hf							
Sm							
Eu							
Ti							
Dy							
Y	42	42	40	45	35	30	41
Ho							
Er							
Yb							
Lu							

Table III-1. Continued.

	Southern Victoria Land (Transantarctic Mountains)											
	Skelton Group (Cook, 2007)											
	Baronick Formation mafic rocks											
Major elements (wt%)	Layers		Tuffs				Clasts					
SiO_2	58.30	53.78	51.48	49.81	50.14	50.64	52.32	50.32	58.17	46.44	44.66	45.35
TiO_2	2.07	2.20	2.40	2.21	2.15	2.18	3.20	2.57	1.58	3.77	2.95	3.47
Al_2O_3	13.04	13.08	18.56	17.97	18.53	19.15	17.68	17.50	18.67	20.13	16.83	16.72
Fe_2O_3(T)	14.11	15.29	14.33	12.30	11.57	11.34	11.58	10.33	6.48	11.66	16.54	14.11
MnO	0.01	0.02	0.08	0.08	0.17	0.45	0.04	0.06	0.02	0.02	0.06	0.16
MgO	2.87	4.23	4.05	3.96	3.26	3.20	2.55	1.52	1.24	1.70	2.18	3.88
CaO	3.52	5.31	5.13	6.98	4.64	5.69	5.30	11.19	6.10	6.35	10.17	8.09
Na_2O	4.53	4.55	3.04	4.00	4.75	4.18	4.88	4.73	4.68	5.66	4.51	6.47
K_2O	1.18	1.08	0.48	2.36	2.00	1.61	1.93	1.25	2.32	1.78	1.64	0.80
P_2O_5	0.38	0.46	0.43	0.33	0.35	0.38	0.52	0.53	0.74	0.95	0.46	0.97
LOI					1.49	1.57				0.99		
Total	100.01	100.00	99.98	100.00	97.56	98.82	100.00	100.00	100.00	98.46	100.00	100.02
Trace elements (ppm)												
Cs												
Rb	26	29	11	46	43	33	28	23	36	30	28	16
Ba	125	119	92	247	280	216	146	231	438	267	293	232
Th												

U												
K												
Nb	18	20		19	17	18	19		21	31	11	43
Ta												
La	10	6	11	7	9	8	17	24	11	54	17	30
Ce	31	31	37	22	35	30	41	46	29	53	43	71
Pb		5					1	7	18	10	5	10
Pr												
Sr	267	242	566	567	577	648	424	657	632	600	560	575
P												
Nd	14	18	22	19	22	20	23	30	19	34	30	48
Zr	128	124	154	141	147	156	189	222	105	268	198	274
Hf												
Sm												
Eu												
Ti												
Dy												
Y	14	15	27	25	20	22	32	19	22	30	20	41
Ho												
Er												
Yb												
Lu												

Table III-1. Continued.

	Thomson orogen (Tasmanides)									
	Anakie Inlier (Fergusson et al., 2009)									
	Mafic schists of the Bathampton Metamorphics									
Major elements (wt%)	PCW23	PCW24	PCW25	PCW29	PCW30	PCW34	PCW27	PCW31	PCW32	PCW35
SiO_2	51.78	46.13	46.97	44.96	43.02	44.11	48.66	42.83	39.79	48.05
TiO_2	2.32	1.17	1.41	1.28	1.06	1.30	1.14	1.03	0.80	1.13
Al_2O_3	14.86	13.05	13.85	14.63	12.07	14.13	15.43	12.42	14.22	15.54
Fe_2O_3(T)	14.03	10.81	11.43	11.68	9.08	12.04	10.24	9.75	7.49	10.53
MnO	0.15	0.15	0.17	0.14	0.14	0.21	0.15	0.15	0.13	0.14
MgO	3.32	6.76	3.93	5.14	5.52	6.02	8.65	5.49	2.82	5.40
CaO	5.19	8.37	16.88	7.37	12.92	14.94	9.48	12.18	18.73	18.11
Na_2O	4.47	3.27	1.71	3.73	3.34	2.55	3.18	2.63	2.18	0.43
K_2O	0.63	0.08	0.12	0.81	0.21	0.14	0.13	0.23	1.24	0.04
P_2O_5	0.25	0.10	0.17	0.16	0.08	0.16	0.10	0.10	0.11	0.11
LOI										
Total	97.00	89.89	96.64	89.90	87.44	95.60	97.16	86.81	87.51	99.48
Trace elements (ppm)										
Cs										
Rb	10	3.83	3	40	16.1	1	1.5	12	47.2	0.99
Ba	100	198	15	70	15	5	10.7	4.99	151	4.99

Th	1	0.89	<1	0.28	<0.2	<1	<0.2	0.28	<0.2	<0.2
U	<1	0.06	<1	<1	0.045	<1	0.072	<1	0.09	<1
K										
Nb	8	1.2	2	<2	1.09	<2	1.5	<2	1.4	<2
Ta		0.08		<0.2	<0.2		<0.2	<0.2	<0.2	0.43
La	1.67			2.22	1.53		2.23	1.72	1.5	1.39
Ce	5.69			5.81	5.16		5.99	5.16	4.91	3.88
Pb	<2	0.758	2	<2	1.15	<2	0.73	<2	0.746	2
Pr	1.14				1.02		1.23		0.962	
Sr	89	58.9	207	66	110.6	62	83	64	67.7	58
P	1139	491	776	786		739	453			487
Nd	6.4			6.39	5.59		6.61	4.8	5.33	4.22
Zr	150	60	84	64	58	76	58	56	60	54
Hf				1.66	1.39		1.69	1.57	1.02	1.38
Sm	2.51			2.58	2.07		2.44	2.01	2.02	1.9
Eu	0.952			0.98	0.765		0.781	0.78	0.773	0.68
Ti	13907	7013	8452	7673	6354	7793	6834	6174	4796	6774
Dy	4.53				3.55		4.17		3.81	
Y	35	25.5	30	28	22.1	26	26	20	25.4	20
Ho	1.01			0.96	0.795		0.923	0.76	0.867	0.72
Er										
Yb										
Lu	0.377			0.44	0.311		0.332	0.35	0.331	0.32

Table III-1. Continued.

	Delamerian orogen (Tasmanides)									
	Glenelg River Complex (Gibson et al., 2015)									
	Wando Vale region									
Major elements (wt%)	2129812 Tholeiite	2129822 Tholeiite	2129823 Tholeiite	2130040 Tholeiite	2129813 Tholeiite	2129815 Tholeiite	2129817 Tholeiite	2129816 Alkali (?) basalt	2129821 Alkali (?) basalt	2130041 High-Fe (?) basalt
SiO_2	50.00	50.60	46.50	49.80	48.50	45.40	46.20	44.50	45.10	52.70
TiO_2	1.83	1.30	1.24	0.80	1.05	1.30	1.42	2.32	2.45	2.66
Al_2O_3	15.50	14.51	16.02	14.07	16.39	16.25	17.18	14.82	16.57	11.68
Fe_2O_3(T)	12.14	12.36	13.20	10.75	7.87	9.82	9.87	13.84	16.66	21.97
MnO	0.21	0.19	0.20	0.18	0.14	0.16	0.20	0.17	0.30	0.32
MgO	6.53	7.24	7.88	8.47	10.16	10.02	9.08	9.13	6.88	1.47
CaO	9.86	10.88	12.26	12.40	13.90	14.63	13.03	9.18	2.32	5.59
Na_2O	3.31	3.04	1.91	2.48	1.39	1.06	1.95	3.24	3.72	3.76
K_2O	0.43	0.25	0.29	0.09	0.17	0.13	0.15	0.46	0.06	0.08
P_2O_5	0.22	0.12	0.10	0.07	0.14	0.16	0.20	0.29	1.69	0.24
LOI										
Total	100.03	100.49	99.60	99.11	99.71	98.93	99.28	97.95	95.75	100.47
Trace elements (ppm)										
Cs	1.2	0.2	1.4	0	0.3	0.2	0.1	2.5	0.2	0.6
Rb	13.7	3.1	6.9	0.6	3	1.5	2.7	15.3	1.4	0.9
Ba	201.1	31.1	24.9	9.2	82.8	24.1	30.7	52.7	100.9	18.9

Th	1.2	0.2	0.2	0.1	0.9	0.9	1.4	1.7	5.7	0.5
U	0.3	0.1	0	0.1	0.2	0.2	0.5	0.4	1.2	0.1
K										
Nb	16.5	2.5	2.3	2.1	12.4	12.7	15.6	20.6	96.5	8.6
Ta	1	0.2	0.1	0.2	0.8	0.8	1	1.3	5.3	0.5
La	10.1	2.6	2.8	2.2	7.2	8.3	10	15.6	70.3	5.7
Ce	21	7.8	7.8	5.5	15.4	17.9	22	36.5	152	17.2
Pb	3.3	1.1	1.1	0.4	2.4	1.4	2.3	6.6	4.6	1.4
Pr	3.1	1.5	1.5	0.9	2.1	2.5	3.1	4.9	19.6	3.2
Sr	238.6	168.2	65.3	100.6	311.7	120.3	276.5	286.4	189.1	84.2
P	970	527	443	311	617	712	887	1309	7824	1063
Nd	15.4	7.9	8.2	5.1	9.4	11.7	13.6	20.8	80.8	17.2
Zr	107	76	69	40	64	90	95	162	414	136
Hf	3	2.1	1.9	1.1	1.7	2.3	2.5	4.1	9.2	3.5
Sm	4.33	3.42	3.52	1.76	2.6	3.17	3.6	5.5	14.9	5.9
Eu	1.76	1.14	1.27	0.7	0.92	1.56	1.3	1.9	5.3	2.4
Ti	10970	7793	7433	4796	6294	7793	8512	13907	14686	15945
Dy	6.52	5.61	5.57	2.83	3.28	4.36	4.68	4.9	10.0	9.8
Y	36.9	33	34	16.7	16.7	24.9	26	23.7	47.5	62.3
Ho	1.35	1.19	1.15	0.62	0.67	0.94	0.97	0.9	1.9	2.1
Er	3.99	3.35	3.4	1.84	1.77	2.54	2.87	2.4	4.8	6.1
Yb	3.81	3.44	3.34	1.73	1.62	2.41	2.66	1.8	3.7	5.8
Lu	0.55	0.49	0.5	0.28	0.24	0.37	0.37	0.3	0.5	0.8

Table III-1. Continued.

	Delamerian orogen (Tasmanides)										
	Mt. Arrowsmith volcanics (Crawford et al., 1997)										
Major elements (wt%)	AR6 Ocean island basalt	AR9 Ocean island basalt	AR7 Ocean island basalt	AR12 Trachy-basalt	AR1 Trachy-basalt	AR1A Trachyte	ED51 Micro-gabbro (Edwards, 1980)	NU19 Ocean island basalt	NU29 Trachy-basalt	NU28 Trachy-basalt	MW26 Ocean island basalt
SiO_2	45.60	49.20	47.80	48.30	51.50	53.20	44.30	55.60	49.20	48.50	48.90
TiO_2	3.11	2.89	2.69	2.43	3.49	0.80	3.03	1.52	2.34	3.39	1.65
Al_2O_3	14.20	16.70	15.40	14.80	15.60	18.30	14.70	17.80	17.50	14.70	15.20
Fe_2O_3(T)	12.65	13.75	11.78	11.37	11.59	13.83	13.82	10.29	16.22	14.67	11.05
MnO	0.20	0.10	0.14	0.17	0.18	0.16	0.17	0.15	0.16	0.19	0.17
MgO	6.13	6.08	4.48	4.12	2.96	2.18	7.97	4.11	3.40	2.15	6.97
CaO	12.82	4.69	10.74	11.88	7.66	3.19	11.18	2.67	2.42	7.99	11.12
Na_2O	4.25	5.19	5.73	5.36	4.40	7.13	2.84	5.73	6.24	6.38	4.48
K_2O	0.59	0.52	0.67	1.00	1.78	0.41	1.57	1.56	0.93	1.03	0.22
P_2O_5	0.45	0.88	0.57	0.58	0.86	0.77	0.39	0.57	1.61	1.06	0.20
LOI	6.24	4.21	6.46	6.44	8.22	4.74	5.77	4.90	3.49	5.18	1.13
Total	100.00	100.00	100.00	100.01	100.02	99.97	99.97	100.00	100.02	100.06	99.96
Trace elements (ppm)											
Cs											
Rb	8	9	7	18	29	6	37	35	14	9	3
Ba	120	258	173	232	710	176	630	531	465	431	337

Th	2.6	6.6	4.5	3.1	5.5	8.9	21	12.1	4.7	3	0.7
U											
K											
Nb	35	64	43	39	60	133	31	22	62	48	13
Ta											
La											
Ce											
Pb											
Pr											
Sr	419	1176	374	613	567	248	602	285	278	588	342
P											
Nd											
Zr	224	387	245	205	339	641	158	275	380	354	115
Hf											
Sm											
Eu											
Ti											
Dy											
Y	27	29	25	26	35	47	21	35	57	44	37
Ho											
Er											
Yb											
Lu											

Table III-1. Continued.

	Delamerian orogen (Tasmanides)									
	Mt. Arrowsmith volcanics (Crawford et al., 1997)									
Major elements (wt%)	MW95 Ocean island basalt	MW40 Trachy-basalt	MW20C Trachy-basalt	MW21A Trachy-basalt	MW34 Trachy-basalt	MW149A Trachyte	MW5 Trachyte	MW74 Dolerite	MW20D Micro-dolerite	MW14 Dolerite
SiO_2	42.10	48.60	48.90	51.20	49.20	60.10	55.70	46.00	48.00	56.10
TiO_2	3.04	2.34	2.98	1.59	3.45	2.32	2.65	1.83	3.18	1.04
Al_2O_3	12.80	14.30	15.70	15.80	14.00	12.50	14.60	19.50	13.70	15.50
Fe_2O_3(T)	15.87	11.73	13.28	12.71	13.99	15.25	16.23	9.78	13.80	11.45
MnO	0.29	0.15	0.21	0.13	0.15	0.06	0.04	0.15	0.21	0.08
MgO	6.09	4.62	3.72	2.91	2.38	0.71	0.24	5.04	4.01	1.16
CaO	15.10	13.11	8.29	6.86	9.42	1.67	1.74	12.50	11.30	6.03
Na_2O	3.76	3.12	5.08	7.44	5.73	5.84	7.23	2.63	5.12	8.44
K_2O	0.47	1.64	1.48	0.14	0.97	0.58	0.50	2.41	0.25	0.12
P_2O_5	0.46	0.31	0.40	1.28	0.62	1.05	1.17	0.24	0.42	0.34
LOI	10.95	3.87	5.95	5.60	6.18	1.71	1.10	5.18	6.69	5.54
Total	99.98	99.92	100.04	100.06	99.91	100.08	100.10	100.08	99.99	100.26
Trace elements (ppm)										
Cs										
Rb	10	17	20	3	12	15	11	59	4	3
Ba	110	622	519	96	293	88	11	482	139	45

Th	2	1.7	1.1	5.8	2.7	4.2	5.83	0.1	2.4	6.37
U										
K										
Nb	33	18	26	67	38	49	54	13	29	74
Ta										
La										
Ce										
Pb										
Pr										
Sr	417	249	522	174	355	152	122	606	237	165
P										
Nd										
Zr	259	158	211	468	284	433	460	119	231	570
Hf										
Sm										
Eu										
Ti										
Dy										
Y	41	27	29	50	48	56	57	20	33	51
Ho										
Er										
Yb										
Lu										

Table III-1. Continued.

	Delamerian orogen (Tasmanides; Tasmania)									
	Arthur Lineament (Holm et al., 2003)									
	Eastern Ahrberg Group									
Major elements (wt%)	75938 Farm Track amphibolite	149372 Nancy Formation	69096 Nancy Formation	149308 Lucy Formation	149301 Lucy Formation	149220 Paradise amphibolite	149344 Paradise amphibolite	149394 Hoyle amphibolite	149313 Frenchman amphibolite	149403 Frenchman amphibolite
SiO_2	55.28	50.14	56.11	50.20	51.46	48.18	52.24	53.24	47.20	48.77
TiO_2	2.09	1.42	1.49	1.75	2.12	2.19	2.41	2.13	3.09	2.02
Al_2O_3	14.36	15.43	12.56	15.18	14.17	14.48	13.45	14.34	14.67	13.89
Fe_2O_3(T)	15.17	11.79	14.16	14.16	17.34	17.26	17.65	20.80	16.88	16.19
MnO	0.15	0.21	0.14	0.24	0.25	0.14	0.23	0.22	0.21	0.25
MgO	6.56	6.81	5.58	6.90	6.28	7.89	5.53	6.17	7.08	5.26
CaO	3.15	12.25	8.95	10.32	7.40	8.18	5.76	1.02	8.14	13.28
Na_2O	4.29	2.72	3.13	2.38	2.38	2.76	3.96	3.27	4.06	1.62
K_2O	0.13	0.28	0.20	0.13	0.14	0.47	0.23	0.58	0.06	0.14
P_2O_5	0.34	0.14	0.09	0.17	0.21	0.18	0.31	0.31	0.29	0.21
LOI		1.92			3.14	2.74	1.83	6.48	2.80	2.06
Total	101.52	101.19	102.41	101.43	101.75	101.73	101.77	102.08	101.68	101.63
	(Wilson, 1991)		(Turner&Crawford, 1993)							
Trace elements (ppm)										
Cs										

Rb	3	7	5	1	2	1	5	1	2	2
Ba	45	46	21	35	31	35	20	178	3	15
Th		2		1	1	0	1	3	2	2
U										
K										
Nb	10	4	5	6	9	9	10	10	13	9
Ta		0.39		0.43			0.64			
La		6		5	16	9	7	22	12	9
Ce		14		16	31	21	26	46	30	22
Pb	4	9	1	22	12	0	3	7	21	3
Pr	5.11	1.54	2.2	1.9	4.4	3.37	2.94			
Sr	25	173	78	156	116	123	75	18	0	302
P										
Nd		12		10	21	18	20	23	21	14
Zr	142	91	90	108	149	134	182	147	183	127
Hf										
Sm	4.71	2.91	3.06	3.43	5.55	5.01	5.74			
Eu	1.3	1.08	1.2	1.23	1.77	2.07	1.71			
Ti	12506	8499	8829	10471	12681	13101	14416	12736	18487	12084
Dy	3.68	3.92	4.47	4.4	7.18	6.35	8.86			
Y	16	31	24	29	43	27	57	25	25	32
Ho	0.77	0.78		0.87	1.57	1.29	1.87			
Er	2.18	2.22	2.66	2.45	4.38	3.46	5.54			
Yb	2.33	1.88	2.18	2.15	3.72	2.9	4.95			
Lu	0.36	0.26	0.3	0.49	0.38	0.71	0.83			

Table III-1. Continued.

	Delamerian orogen (Tasmanides; Tasmania)								
	Arthur Lineament (Holm et al., 2003)								
	Eastern Ahrberg Group								
Major elements (wt%)	149401 Frenchman amphibolite	149395 Farm Track amphibolite	149374 Nancy Formation	149303 Lucy Formation	149370 Lucy Formation	149369 Lucy Formation	149307 Lucy Formation	149237 Paradise amphibolite	149228 Paradise amphibolite
SiO_2	50.70	52.40	51.01	51.26	51.35	51.27	50.32	51.68	49.07
TiO_2	2.10	0.41	2.01	2.73	2.03	1.97	2.30	3.72	2.13
Al_2O_3	13.71	15.58	14.12	13.06	13.91	14.36	14.33	12.87	14.52
Fe_2O_3(T)	15.69	10.49	15.04	18.58	15.05	15.14	15.61	15.41	14.64
MnO	0.23	0.12	0.22	0.30	0.24	0.23	0.26	0.13	0.21
MgO	6.06	12.25	5.67	4.86	6.26	6.20	5.49	4.76	6.86
CaO	10.29	6.29	10.64	8.21	9.98	8.92	9.81	6.60	11.09
Na_2O	2.07	3.34	2.39	2.23	2.06	2.74	3.09	4.65	2.67
K_2O	0.51	0.08	0.23	0.38	0.43	0.49	0.12	1.10	0.07
P_2O_5	0.22	0.08	0.20	0.25	0.21	0.19	0.21	0.60	0.21
LOI	2.30	4.38	2.00	2.33	2.46	2.82	2.14	1.30	2.42
Total	101.58	101.04	101.53	101.86	101.52	101.51	101.54	101.52	101.47
Trace elements (ppm)									
Cs									
Rb	12	18	4	8	9	34	16	2	1

Ba	112	22	22	67	104	96	12	151	<4
Th	2	5	1	3	2	5	0	0	1
U									
K									
Nb	8	6	8	11	9	8	7	39	9
Ta									
La	10	7	10	13	10	12	7	40	9
Ce	28	17	25	33	25	26	20	89	20
Pb	3	10	3	44	11	4	4	3	5
Pr									
Sr	157	101	156	157	148	166	214	183	188
P									
Nd	18	7	14	20	17	17	15	50	17
Zr	134	52	132	159	133	134	115	283	127
Hf									
Sm									
Eu									
Ti	12563	2455	12025	16329	12146	11789	13764	22263	12746
Dy									
Y	31	33	31	38	32	40	26	22	31
Ho									
Er									
Yb									
Lu									

Table III-1. Continued.

	Delamerian orogen (Tasmanides; Tasmania)							
	Arthur Lineament (Holm et al., 2003)							
	Western Ahrberg Group							
Major elements (wt%)	149283 Bernafai Volcanics	69090 Bernafai Volcanics	149362 Tunnelrace Volcanics	69098 Tunnelrace Volcanics	894848 Tunnelrace Volcanics	149378 Bernafai Volcanics	149295 Bernafai Volcanics	149383 Tunnelrace Volcanics
SiO_2	51.23	50.00	50.41	49.18	48.02	48.66	50.53	53.17
TiO_2	0.25	1.84	1.62	2.09	4.60	1.87	1.64	1.70
Al_2O_3	14.74	16.13	14.73	14.73	16.43	16.42	14.93	13.77
Fe_2O_3(T)	9.91	14.40	13.34	16.27	21.15	14.41	13.83	14.34
MnO	0.15	0.23	0.25	0.20	0.03	0.22	0.23	0.20
MgO	13.32	6.73	7.87	4.93	2.73	8.11	7.01	5.90
CaO	8.03	10.05	9.90	9.86	0.52	8.37	10.62	7.01
Na_2O	2.71	1.68	2.80	3.50	6.19	3.12	2.30	5.09
K_2O	0.59	0.22	0.24	0.65	1.97	0.06	0.09	0.08
P_2O_5	0.05	0.15	0.19	0.22	0.48	0.19	0.19	0.19
LOI	3.88		3.27			3.93	2.94	1.89
Total	100.98	101.43 (Turner&Crawford, 1993)	101.35	101.63 (Turner&Crawford, 1993)	102.12 (Turner&Crawford, 1993)	101.43	101.37	101.45
Trace elements (ppm)								
Cs								
Rb	12	3	23	10	38	6	1	9

Ba	350	55	20	193	105	<4	21	19
Th	1		0			0	1	1
U								
K								
Nb	2	6	6	9	40	6	7	10
Ta	0.19		0.37					
La	2		5			7	8	10
Ce	11		18			15	18	27
Pb	6	2	2	2	11	5	0	2
Pr	0.89	2.22	1.69	3.52	11.27			
Sr	90	215	78	118	20	131	200	298
P								
Nd	6		13			13	11	18
Zr	31	88	93	129	440	105	97	126
Hf								
Sm	0.99	3.3	3.15	4.68	10.86			
Eu	0.34	1.37	1.14	1.61	3.44			
Ti	1497	11012	9695	12504	27505	11191	9817	10172
Dy	2.12	4.26	3.91	5.56	9.09			
Y	15	22	37	28	44	24	23	32
Ho	0.5		0.78	1.13	1.9			
Er	1.64	2.46	2.18	3.05	5.54			
Yb	1.69	1.89	1.86	2.57	5.46			
Lu		0.26	0.32	0.78				

Table III-1. Continued.

	Delamerian orogen (Tasmanides; King Island)													
	Grassy Group (Meffre et al., 2004)													
	Grimes Intrusive Suites					City of Melbourne Volcanics					Bold Head Volcanics			
Major elements (wt%)	K167	K168	K152	K153	K3	K203	K111	K109	K128	K127	K55	K50	K226	K58
SiO_2	44.96	49.03	57.53	60.28	64.10	52.52	52.01	50.89	53.07	53.00	46.80	47.42	52.34	49.28
TiO_2	0.22	0.27	0.99	0.70	0.73	0.52	0.78	0.79	0.79	0.77	1.41	1.70	1.57	1.77
Al_2O_3	8.51	14.58	14.39	16.22	15.80	14.36	13.82	13.35	13.57	13.53	15.32	15.94	17.14	13.74
Fe_2O_3(T)	12.13	9.25	7.82	7.27	6.69	10.58	14.26	15.89	14.39	14.30	12.70	13.48	13.05	15.13
MnO	0.14	0.15	0.15	0.12	0.17	0.18	0.21	0.25	0.21	0.20	0.20	0.22	0.13	0.22
MgO	29.90	15.64	6.03	6.71	5.51	8.10	6.92	6.81	6.50	6.09	10.49	7.14	6.04	6.77
CaO	3.63	9.15	7.41	1.62	0.66	9.00	6.67	6.76	5.96	6.50	9.52	9.84	4.77	8.38
Na_2O	0.29	1.22	2.19	3.55	4.10	4.51	5.14	4.90	5.38	5.44	3.27	3.38	3.10	4.29
K_2O	0.12	0.69	3.35	3.43	2.10	0.17	0.11	0.27	0.05	0.09	0.13	0.61	1.67	0.25
P_2O_5	0.09	0.03	0.12	0.12	0.12	0.04	0.08	0.09	0.07	0.08	0.17	0.28	0.20	0.16
LOI	9.31	5.19	2.44	4.02	3.42	2.32	2.16	2.41	1.72	1.40	3.57	2.47	6.53	1.69
Total	100.00	100.00	100.00	100.00	100.00	100.00	100.00	100.00	100.00	100.00	100.00	100.00	100.00	100.00
Trace elements (ppm)														
Cs		1.47		1.69	3.13		0.48		0.22	0.57		1.38	2.65	0.15
Rb	9.2	29.4	85.9	66.1	34.6	4.7	1.9	5.2	0.9	2.7	4.3	22.6	50.2	6.4

Ba	16	132	506	637	795	117	102	124	90	94	88	271	681	148
Th		1.77	7.9	10.3	11.6		1.96	2.7	1.36	1.96	2.7	2.76	3.90	0.65
U		0.50	2.3	3.03	3.40	1.5	0.64		0.45	0.49		0.61	0.664	0.15
K														
Nb	2.3	3.90	12.7	13.9	15.3	3.1	4.84	5.5	5.92	4.79	19.1	34.5	33.5	7.06
Ta		0.30		1.03	1.14		0.30			0.28		2.07	1.77	0.48
La	4.1	5.25	22.3	29.0	34.6	3.9	7.68	8.1	4.46	7.17	17.6	24.9	28.8	7.21
Ce	5.39	12.45	56.64	62.48	72.23	9.41	15.25	18.33	9.86	15.24	41.36	43.91	60.31	17.94
Pb	2.2	<1.5	5.0	3.2	18.1	2.7	2.5		2.0	2.9		1.8	4.1	1.0
Pr		1.57		7.38	8.75		1.88		1.37	1.85		5.03	7.30	2.69
Sr	7	82	185	86	93	65	138	80	69	64	240	222	203	156
P														
Nd	2.03	6.18	28.42	28.45	33.90	5.4	8.32	8.39	5.61	8.22	17.63	19.62	26.27	13.64
Zr	24	35	150	179	198	35	52	61	54	52	93	97	156	102
Hf		0.97		4.94	5.50		1.61		1.31	1.62		2.43	4.11	2.71
Sm		1.45		5.91	6.83		2.53		1.76	2.55		4.08	5.21	4.07
Eu		0.39		1.16	1.24		0.93		0.50	0.87		1.43	1.98	1.45
Ti	1345	1606	5963	4243	4378	3150	4738	4792	4816	4654	8544	10337	9514	10755
Dy		1.92		5.58	5.86		5.60		3.61	5.74		4.36	5.25	5.36
Y	7.9	10.9	34	32.2	32.2	23.1	35.9	40.5	31.9	36.3	21.7	23.3	30.2	30
Ho		0.43		1.19	1.23		1.33		0.82	1.36		0.90	1.12	1.12
Er		1.26		3.47	3.56		4.10		2.55	4.14		2.51	3.23	3.13
Yb		1.3		3.5	3.6		4.0		2.6	4.2		2.3	3.2	2.8
Lu		0.20		0.53	0.54		0.62		0.42	0.64		0.33	0.48	0.40

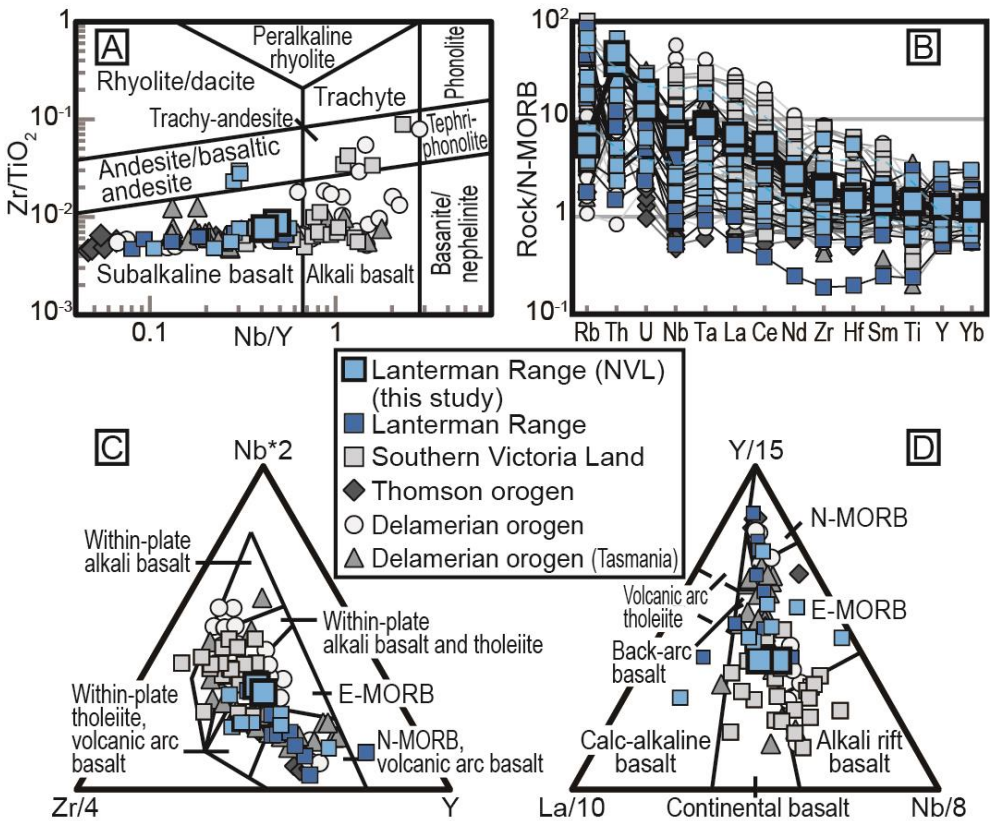

Figure III-2. Whole-rock geochemical data of late Neoproterozoic mafic rocks from the Transantarctic Mountains and Tasmanides. A: Zr/TiO_2 versus Nb/Y diagram (Winchester and Floyd, 1977). B: Normal-mid ocean ridge basalt (N-MORB)–normalized trace element diagram. C: Nb–Zr–Y diagram (Meschede, 1986). D: Y–La–Nb diagram (Cabanis and Lecolle, 1989). Data compiled from the literature: Lanterman Range of northern Victoria Land (NVL) after Di Vinecnzo et al. (1997, 2016), southern Victoria Land after Cook (2007) and Cooper et al. (2011), Thomson orogen after Fergusson et al. (2009), Delamerian orogen in Australia mainland after Crawford et al. (1997) and Gibson et al. (2015) and Delamerian orogen in Tasmania after Holm et al. (2003) and Meffre et al. (2004). E—enriched.

epoxy disc with SL13 and FC-1 standard zircon crystals. The former was used for measuring the U concentration (238 ppm; Claoué-Long et al., 1995), and the latter for calibrating $^{206}Pb/^{238}U$ ratios ($^{206}Pb^{*}/^{238}U$ = 0.1859; Paces and Miller, 1993). The cathodoluminescence (CL) images of zircon crystals were obtained using a JEOL JSM-6610LV scanning electron microscope housed at the Korea Basic Science Institute (KBSI). The U-Th-Pb isotopic compositions of zircon were measured using the KBSI SHRIMP-IIe. The analytical protocol followed that of Williams (1998). All isotopes were measured using a primary O_2^- beam with ~3–5 nA and ~25 μm diameter spot. Common Pb contributions to total Pb counts were corrected using the ^{207}Pb correction method based on the Pb/U concordance and model common Pb composition (Cumming and Richards, 1975; Williams, 1998). The isotopic data were reduced using the Prawn/Lead 6.5.5 software (written communication, T. Ireland, 1996), and were plotted using the program Isoplot/Ex (Ludwig, 2008).

Sample E-1a

The CL images of zircons show distinctive core–mantle–rim growth zones (Figure III-3). The cores showing intermediate CL intensities with subtle oscillatory zonation commonly contain acicular apatite, whereas the mantle and rim are typified by eclogite-facies mineral inclusions. The weighted mean $^{206}Pb/^{238}U$ ages of the mantle and rim are 515 ± 4 Ma ($t\sigma$) and 498 ± 11 Ma ($t\sigma$), respectively (Kim et al., 2019). Fourteen spot

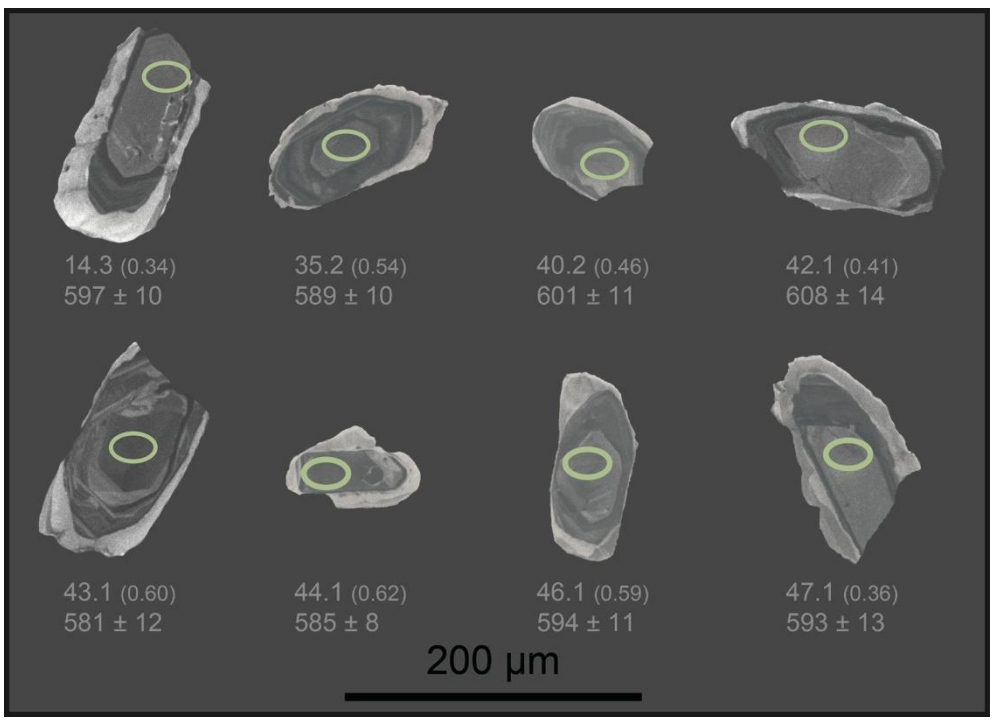

Figure III-3. Representative cathodoluminescence images of zircon from a barroisite eclogite (sample E-1a). Spot numbers for the U-Th-Pb analysis listed in Table III-2 are shown for individual zircon grains, followed by their Th/U ratios in parentheses. The bottom lines list the $^{206}Pb/^{238}U$ dates (in Ma) with 1σ errors. Ellipses denote the analytical spots.

Table III-2. The SHRIMP U-Th-Pb isotopic compositions of zircon from the eclogite

Spot no.	U (ppm)	Th (ppm)	Th/U	Common ^{206}Pb (%)	$^{207}Pb^*/^{206}Pb^*$	$^{208}Pb^*/^{206}Pb^*$	$^{206}Pb^*/^{238}U$	$^{208}Pb^*/^{232}Th$	$^{207}Pb/^{206}Pb$ age (Ma)	$^{206}Pb/^{238}U$ age (Ma)	$^{208}Pb/^{232}Th$ age (Ma)	Concordance (%)
Sample E-1a												
1.3	60	31	0.51	0.24	0.04927 ± 566	0.1613 ± 755	0.09807 ± 337	0.031 ± 193	161 ± 249	603 ± 20	618 ± 38	-189
2.2	68	29	0.42	0.17	0.05445 ± 305	0.1271 ± 782	0.10085 ± 264	0.031 ± 210	390 ± 131	619 ± 15	608 ± 41	38
6.3	8	0	0.03	0.11	0.05618 ± 1256	-0.0038 ± 1768	0.08889 ± 600	-0.012 ± 5786	460 ± 460	549 ± 36	-	80
14.3	77	25	0.34	0.10	0.05684 ± 156	0.1003 ± 446	0.09655 ± 160	0.026 ± 121	485 ± 61	597 ± 10	526 ± 24	77
34.2	80	39	0.50	0.21	0.05323 ± 209	0.1588 ± 475	0.09398 ± 173	0.027 ± 116	339 ± 89	582 ± 11	544 ± 23	26
35.2	95	50	0.54	0.09	0.05715 ± 138	0.1660 ± 454	0.09534 ± 162	0.028 ± 85	497 ± 53	589 ± 10	562 ± 17	81
40.2	82	36	0.46	-0.13	0.05809 ± 102	0.1470 ± 464	0.09775 ± 170	0.030 ± 86	533 ± 38	601 ± 11	600 ± 17	87
42.1	52	22	0.41	0.23	0.05662 ± 258	0.1285 ± 353	0.09887 ± 241	0.031 ± 125	477 ± 104	608 ± 14	611 ± 24	71
43.1	132	80	0.60	0.80	0.05628 ± 194	0.1818 ± 263	0.09425 ± 201	0.028 ± 80	463 ± 78	581 ± 12	565 ± 16	74
44.1	189	113	0.62	0.17	0.05648 ± 109	0.1859 ± 371	0.09436 ± 123	0.027 ± 60	471 ± 43	585 ± 8	546 ± 12	76
45.1	60	28	0.48	0.18	0.05259 ± 257	0.1397 ± 675	0.09506 ± 204	0.024 ± 158	311 ± 111	592 ± 13	487 ± 31	8
46.1	96	55	0.59	0.12	0.05884 ± 115	0.1898 ± 455	0.09681 ± 163	0.031 ± 80	561 ± 43	594 ± 11	613 ± 16	94
47.1	52	18	0.36	0.35	0.06030 ± 162	0.1066 ± 543	0.09635 ± 210	0.029 ± 127	614 ± 58	594 ± 13	574 ± 25	104
48.1	29	19	0.67	0.37	0.04079 ± 557	0.1999 ± 1283	0.08097 ± 229	0.020 ± 204	-301 ± 349	513 ± 15	392 ± 40	378

Errors are 1σ estimates. All the isotopic compositions were calculated using the ^{207}common Pb correction method except for $^{207}Pb^*/^{206}Pb^*$ ratios corrected by ^{204}Pb. Pb^* denotes radiogenic Pb. Concordance was calculated from $^{207}Pb/^{235}U$ and $^{206}Pb/^{238}U$ ages.

Table III-2. Continued.

Spot no.	U (ppm)	Th (ppm)	Th/U	Common ^{206}Pb (%)	$^{207}Pb^*/^{206}Pb^*$	$^{208}Pb^*/^{206}Pb^*$	$^{206}Pb^*/^{238}U$	$^{208}Pb^*/^{232}Th$	$^{207}Pb/^{206}Pb$ age (Ma)	$^{206}Pb/^{238}U$ age (Ma)	$^{208}Pb/^{232}Th$ age (Ma)	Concordance (%)
Sample E-1c												
6.1	65	34	0.54	-0.36	0.05257 ± 615	0.1672 ± 779	0.09824 ± 101	0.0307 ± 167	310 ± 266	604 ± 19	610 ± 33	3
7.1	116	75	0.67	-0.05	0.05660 ± 406	0.2055 ± 651	0.09929 ± 86	0.0306 ± 125	476 ± 159	610 ± 16	610 ± 24	71
8.1	90	54	0.62	0.28	0.05705 ± 468	0.1915 ± 736	0.09856 ± 91	0.0305 ± 141	493 ± 181	606 ± 17	607 ± 28	77
10.1	334	322	0.99	0.05	0.06010 ± 131	0.3018 ± 437	0.09797 ± 64	0.0297 ± 76	607 ± 47	602 ± 12	592 ± 15	101
11.1	87	43	0.50	-0.08	0.06213 ± 480	0.1538 ± 685	0.09882 ± 91	0.0302 ± 151	679 ± 165	607 ± 17	601 ± 30	111
12.1	86	45	0.54	0.08	0.05111 ± 487	0.1672 ± 712	0.09974 ± 95	0.0307 ± 151	246 ± 219	613 ± 17	611 ± 30	-54
13.1	98	49	0.52	0.11	0.05782 ± 428	0.1565 ± 679	0.09479 ± 87	0.0286 ± 139	523 ± 162	584 ± 16	570 ± 27	88
14.1	106	60	0.58	-0.16	0.05723 ± 441	0.1771 ± 859	0.09829 ± 87	0.0299 ± 169	501 ± 170	604 ± 16	596 ± 33	79
17.1	128	76	0.61	-0.04	0.05666 ± 295	0.1882 ± 556	0.10078 ± 73	0.0310 ± 112	478 ± 115	619 ± 13	618 ± 22	70
20.1	113	58	0.53	0.00	0.05749 ± 359	0.1729 ± 710	0.09312 ± 71	0.0305 ± 146	511 ± 137	574 ± 13	607 ± 29	87
21.1	96	43	0.46	-0.22	0.05631 ± 474	0.1487 ± 630	0.10055 ± 82	0.0323 ± 152	465 ± 186	618 ± 15	642 ± 30	66
22.1	123	50	0.42	0.15	0.06056 ± 347	0.1299 ± 555	0.09884 ± 75	0.0307 ± 137	624 ± 124	608 ± 14	612 ± 27	103

Errors are 1σ estimates. All the isotopic compositions were calculated using the ^{207}common Pb correction method except for $^{207}Pb^*/^{206}Pb^*$ ratios corrected by ^{204}Pb. Pb^* denotes radiogenic Pb. Concordance was calculated from $^{207}Pb/^{235}U$ and $^{206}Pb/^{238}U$ ages.

analyses on the cores yielded fairly low concentrations of U (29–189 ppm) and Th (18–113 ppm), except for one spot analysis with much lower U and Th (spot 6.3; U = 8 ppm and Th = 0.2 ppm) (Table III-2). The proportion of common ^{206}Pb is low (<0.8%). The Th/U ratios of the cores are in the range 0.34–0.67, except for the spot 6.3 (Th/U = 0.03) with bright CL intensity, which was ignored in the mean age calculation. Five analyses (spots 1.3, 2.2, 34.2, 45.1 and 48.1) were discarded because of low concordance (<40%) due to Pb overcorrection and possible mixed analysis. Apparent ^{206}Pb/^{238}U ages of the remaining 8 analyses range from 608 ± 14 Ma (1σ) to 581 ± 12 Ma (1σ), yielding the weighted mean ^{206}Pb/^{238}U age of 590.8 ± 8.3 Ma (*tσ*; MSWD = 0.80; Figure III-4).

Sample E-1c

The CL images of zircons show strikingly similar textures to those of the sample E-1a, consisting of distinctive core-mantle-rim growth zones. The cores commonly show intermediate CL intensities with subtle oscillatory zonation, whereas the mantle and rim are typified by low and high CL intensities, respectively. Twelve spot analyses on the cores yielded fairly low concentrations of U (65–128 ppm) and Th (34–76 ppm), except for one analysis high in U and Th (spot 10.1; U = 334 ppm and Th = 322 ppm) (Table III-2). The proportion of common ^{206}Pb is low (<0.3%). The Th/U ratios of the cores are in the range 0.42–0.67, excluding one spot 10.1 (Th/U = 0.99). Four analyses (spots 6.1, 12.1, 17.1 and 21.1) were ignored

because of low concordance (<70%) due to Pb overcorrection and possible mixed analysis. The remaining 8 spot dates vary from 610 ± 16 Ma (1σ) to 574 ± 13 Ma (1σ). When rejecting one youngest outlier (spot 20.1), their weighted mean $^{206}Pb/^{238}U$ age is 603.2 ± 4.4 Ma (*tσ*; MSWD = 3.05; Figure III-5).

DISCUSSION

Microstructural and geochemical lines of evidence such as acicular apatite inclusion, oscillatory zonation, and high Th/U ratio (0.34–0.67) of the analyzed zircon cores support plutonic origin of the eclogite protolith (Corfu et al., 2003). The E-MORB geochemical affinity of the gabbroic protolith without xenocrystic zircon further suggests its emplacement into an extended and thinned continental crust with negligible crustal assimilation (e.g. Ernst et al., 2005). The *c.* 590 Ma crystallization of zircon core in the eclogite is thus a product of rift-related mafic magmatism in the NVL. Such an Ediacaran activity has never been reported in the TAM, in contrast to the Cryogenian (*c.* 670–650 Ma) rift-related magmatism (Goodge et al., 2002, Cooper et al., 2011).

The time for the Ediacaran rifting along the East Gondwana margin has been mainly constrained from volcanic rocks intercalated with the shelf to shoreline and shallow marine siliciclastic (meta)sediments in the Delamerian orogen (Figure III-1). They include: (1) alkali rhyolite (*c.* 586 Ma) of the Koonenberry belt (Crawford et al., 1997; Greenfield et al., 2011);

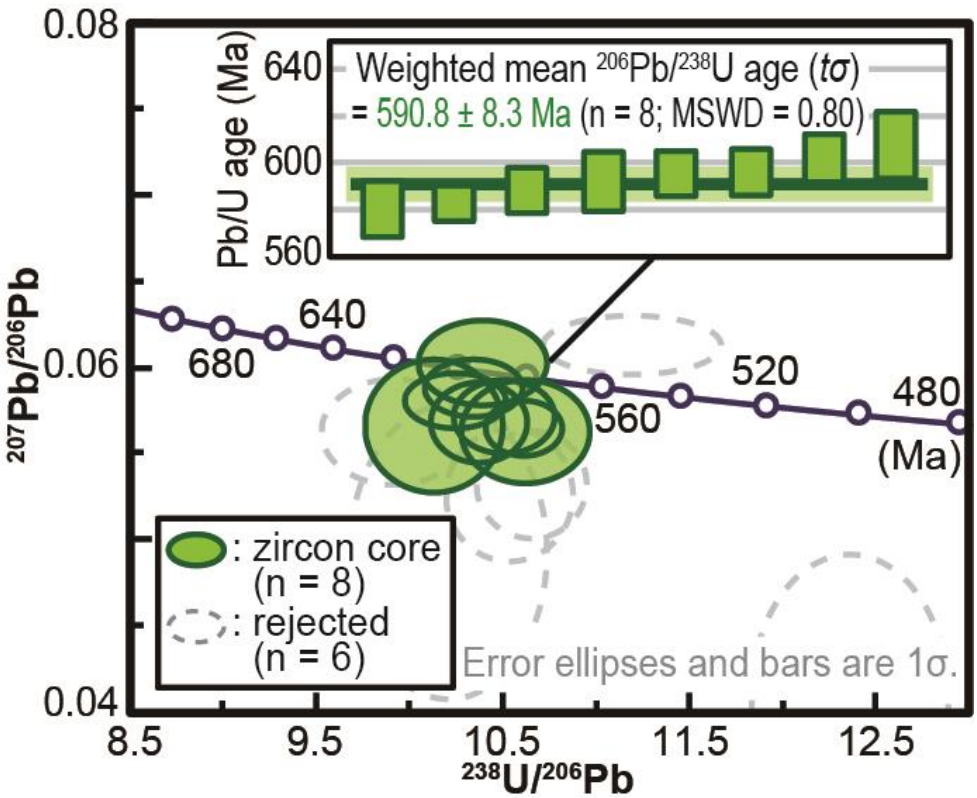

Figure III-4. Tera-Wasserburg concordia diagram for the U-Pb spot analyses of zircon from the eclogite sample (E-1a). Broken ellipses denote the spots excluded in the weighted mean age calculation. Inset diagram shows the error bars of $^{206}Pb/^{238}U$ dates considered for the age calculation. All ages were calculated using the constants recommended by the IUGS Subcommission on Geochronology (Steiger and Jäger, 1977) with 95% confidence limits ($t\sigma$). MSWD—mean square of weighted deviates.

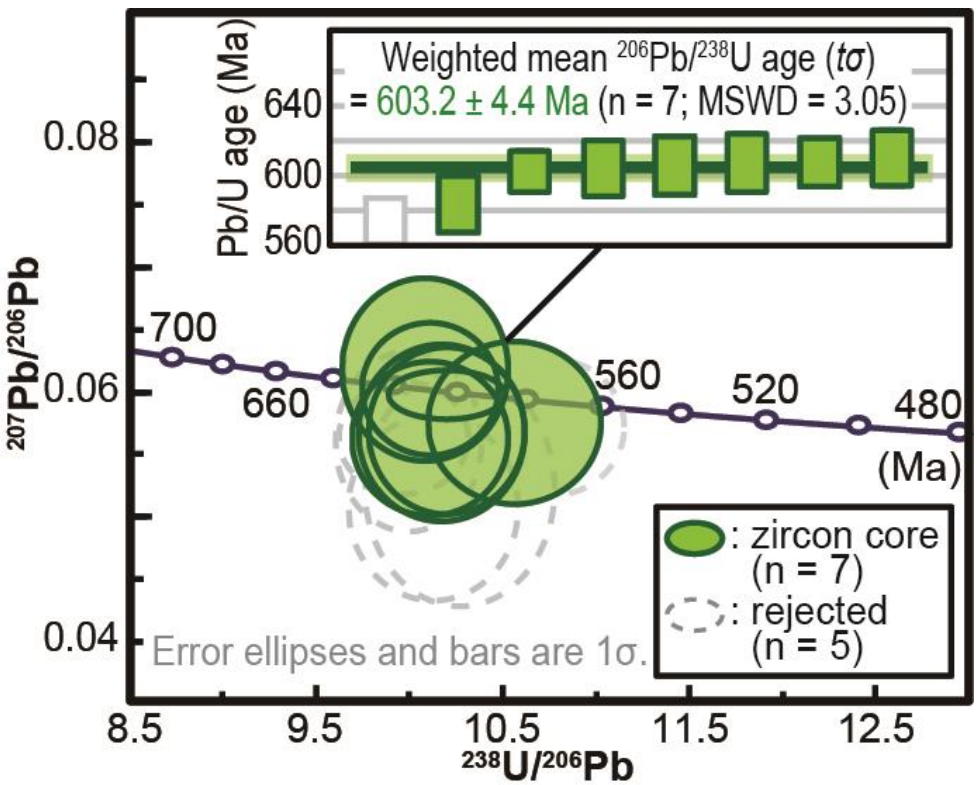

Figure III-5. Tera-Wasserburg concordia diagram for the U-Pb spot analyses of zircon from the eclogite sample (E-1c). Broken ellipses denote the spots excluded in the weighted mean age calculation. Inset diagram shows the error bars of $^{206}Pb/^{238}U$ dates considered for the age calculation. All ages were calculated using the constants recommended by the IUGS Subcommission on Geochronology (Steiger and Jäger, 1977) with 95% confidence limits ($t\sigma$). MSWD—mean square of weighted deviates.

(2) andesitic sill (*c.* 575 Ma) of the Grassy group, King Island (Calver et al., 2004; Meffre et al., 2004); and (3) rhyodacite (*c.* 582 Ma) of the Togari group, northwestern Tasmania (Calver et al., 2004). These volcanic rocks might be the extrusive equivalent of gabbroic protolith of the Lanterman Range eclogite. Direen and Crawford (2003a) also suggested the formation of volcanic passive margin at *c.* 600–580 Ma, on the basis of seaward-dipping reflectors associated with shallow marine sedimentary rocks widespread along the southeastern coast of Australia; in contrast, magma-poor passive margin dominated by quartzose turbidites developed in the Thomson orogen (Fergusson et al., 2009). The closure of passive margins in the region took place during the Cambrian-Ordovician Ross–Delamerian orogeny (e.g. Boger, 2011). All the above geological features suggest that NVL experienced a tectonic evolution identical to that of the Delamerian orogen during the Ediacaran to Ordovician time.

The Cryogenian rifting event has been discovered less commonly in the Adelaide rift complex, Australia as well as SVL and CTM, Antarctica: (1) ash fall tuff (*c.* 663 Ma) within the Wilyerpa formation of the Adelaide rift complex (Cox et al., 2018); (2) a gabbro body (*c.* 668) in association with shoreline to shelf sediments of the Beardmore group, CTM (Goodge et al., 2002); and (3) alkali rhyolite clasts (*c.* 650 Ma) in metaconglomerate of the Skelton group, SVL (Cooper et al., 2011). On the basis of the Cryogenian rift-margin magmatism, the Ediacaran arc-related igneous clasts (*c.* 590–560 Ma) from glacial tills in the ice-covered CTM interior and the

George V coast of Wilkes Land were regarded as an important piece of evidence for the tectonic inversion to convergent regime along the Antarctic paleo-Pacific margin (Figure III-1; Goodge and Fanning, 2010; Goodge et al., 2012). The Barrovian garnet-bearing assemblage of metamorphic rocks in SVL, where the garnet Lu-Hf and monazite U-Pb ages range *c.* 590–570 Ma, was also referred to as outcrop evidence for the Ediacaran convergent margin (Hagen-Peter et al., 2016). Thus, the onset of the Ross orogeny is considered to be *c.* 590 Ma (Goodge et al., 2012; Hagen-Peter et al., 2016), in contrast to *c.* 600–580 Ma rifting in the eastern Australian margin (Direen and Crawford, 2003a; Fergusson et al., 2009). My result, however, suggests that the rifting was also active at *c.* 590 Ma in NVL, suggesting that tectonic inversion to convergent margin probably took place not earlier than *c.* 540 Ma, corresponding to the oldest granite (Black and Sheraton, 1990). This interpretation is compatible with the time of arc-related magmatism known to be *c.* 540 Ma (Turner et al., 2009) or even younger at *c.* 514 Ma in the Delamerian orogen (Foden et al., 2006). Hence, I suggest that the Australia–Antarctic margin of East Gondwana share a common late Neoproterozoic evolution history characterized by twofold rifting events at the Cryogenian (*c.* 670–650 Ma) and Ediacaran (*c.* 600–580 Ma) (cf. Cooper et al., 2011). The loci of two rifting events are spatially bounded in eastern Australia; the rifting events at the Cryogenian and Ediacaran took place to the west and east of the so-called Tasman line, respectively (Figure III-1). The Tasman line, the boundary between the craton and supracrustal fold-thrust belts in

the Tasmanides (e.g. Direen and Crawford, 2003b), could be extended through the Neoproterozoic rift margin of the TAM (Figure III-1; Goodge and Finn, 2010). The timing of onset of arc-related magmatism and metamorphism along the East Gondwana margin is also variable: (1) the early to middle Cambrian in eastern Australia and NVL (*c.* 520–500 Ma; Foden et al., 2006; Rocchi et al., 2011; Kim et al., 2019); and (2) the Ediacaran in SVL and CTM (*c.* 590–570 Ma; Goodge et al., 2012; Hagen-Peter et al., 2016). Therefore, the propagation of rifting from Cryogenian to Ediacaran took place synchronously along the East Gondwana margin, and support diachronous inversion into convergent tectonic regime (e.g. Foden et al., 2006).

Our U-Pb age of zircon cores may also shed light on the provenance of the Pacific-Gondwana zircon population (*c.* 700–500 Ma) which is widespread not only in the Cambrian to Triassic siliciclastic (meta)sedimentary rocks along the TAM and Tasmanides (e.g. Ireland et al., 1998; Estrada et al., 2016; Paulsen et al., 2016; Fergusson et al., 2017; Glen et al., 2017), but also in the Eocene glacial deposits (Licht and Palmer, 2013) and beach sands (Sircombe, 1999). In particular, the origin of its subgroup clustering at *c.* 600–580 Ma is highly debatable (e.g. Fergusson et al., 2007; Cooper et al., 2011; Goodge et al., 2012). I suggest that the rift-related magmatism at *c.* 600–580 Ma prior to the Ross orogeny could provide the first-cycle detritus for the Ediacaran component of detrital Pacific-Gondwana zircon. The Ediacaran rift-related magmatism also produced

cogenetic felsic to intermediate igneous rocks (e.g. Crawford et al., 1997; Meffre et al., 2004). The deficiency of the rock exposures could be accounted for by their poor preservation potential (Hawkesworth et al., 2009; Cawood et al., 2012), and the Ediacaran detrital zircon thus had deposited and recycled as post-600 Ma sediments along the East Gondwana margin.

CONCLUSIONS

I discovered for the first time the Ediacaran (*c.* 590 Ma) rift-related magmatism in the TAM, using whole-rock geochemistry and zircon U-Pb ages in the eclogites of the Ross orogen. This gabbroic emplacement is tectonically correlated to mafic igneous rocks (*c.* 600–580 Ma) of rift/passive-margin environments in the eastern Australian Tasmanides. Distinct tectonic evolution of late Neoproterozoic rifting and its diachronous transition into convergent tectonics was proposed in the context of rift-center propagation: i.e., the Cryogenian rifting–Ediacaran arc in SVL and CTM versus the Ediacaran rifting–Cambrian inversion in NVL and the Delamerian–Thomson orogens. The eastern Australian linkage of NVL is also compatible with regional correlations among relevant terranes. The Ediacaran rift magmatism could be the first-order source of the omnipresent age peak of detrital zircon, i.e. the Pacific-Gondwana population (*c.* 700–500 Ma).

REFERENCES

Adams, C.J., Bradshaw, J.D., & Ireland, T.R. (2014). Provenance connections between late Neoproterozoic and early Palaeozoic sedimentary basins of the Ross Sea region, Antarctica, south-east Australia and southern Zealandia. *Antarctic Science*, 26, 173–182.

Black, L.P., & Sheraton, J.W. (1990). The influence of Precambrian source components on the U-Pb zircon age of a Palaeozoic granite from northern Victoria Land, Antarctica. *Precambrian Research*, 46, 275–293.

Boger, S.D. (2011). Antarctica – Before and after Gondwana. *Gondwana Research*, 19, 335–371.

Cabanis, B., & Lecolle, M. (1989). Le diagramme La/10-Y/15-Nb/8: Un outil pour la discrimination des series volcaniques et lamise en evidence des processus demelange et/ou de contamination crustale. Compte Rendus de I'Académie des Sciences Series II, 309, 2023–2029.

Calver, C.R., Black, L.P., Everard, J.L., & Seymour, D.B. (2004). U-Pb zircon age constraints on late Neoproterozoic glaciation in Tasmania. *Geology*, 32, 893–896.

Cawood, P.A. (2005). Terra Australis Orogen: Rodinia breakup and development of the Pacific and Iapetus margins of Gondwana during the Neoproterozoic and Paleozoic. *Earth-Science Reviews*, 69, 249–279.

Cawood, P.A., Hawkesworth, C.J., & Dhuime, B. (2012). Detrital zircon record and tectonic setting. *Geology*, 40, 875–878.

Claoué-Long, J.C., Compston, W., Roberts, J., & Fanning, C.M. (1995). Two Carboniferous ages: A comparison of SHRIMP zircon dating with conventional zircon ages and $^{40}Ar/^{39}Ar$ analysis. In W.A. Berggren, D.V. Kent, M.-P. Aubry, and J. Hardenbol (Eds.), *Geochronology, time scales and global stratigraphic correlation*, Society for Sedimentary Geology (SEPM) Special Publication (vol. 54(4), pp. 3–21). Tulsa, OK.: SEPM.

Cooper, A.F., Maas, R., Scott, J.M., & Barber, A.J.W. (2011). Dating of volcanism and sedimentation in the Skelton Group, Transantarctic

Mountains: Implications for the Rodinia-Gondwana transition in southern Victoria Land, Antarctica. *Geological Society of America Bulletin*, 123, 681–702.

Corfu, F., Hanchar, J.M., Hoskin, P.W.O., & Kinny, P. (2003). Atlas of zircon textures. *Reviews in Mineralogy and Geochemistry*, 53, 469–500.

Cox, G.M., Isakson, V., Hoffman, P.F., Gernon, T.M., Schmitz, M.D., Shahin, S., Collins, A.S., Preiss, W., Blades, M.L., Mitchell, R.N., & Nordsvan, A. (2018). South Australian U-Pb zircon (CA-ID-TIMS) age supports globally synchronous Sturtian deglaciation. *Precambrian Research*, 315, 257–263.

Crawford, A.J., Stevens, B.P.J., & Fanning, M. (1997). Geochemistry and tectonic setting of some Neoproterozoic and Early Cambrian volcanics in western New South Wales. *Australian Journal of Earth Sciences*, 44, 831–852.

Cumming, G.L., & Richards, J.R. (1975). Ore lead isotope ratios in a continuously changing earth. *Earth and Planetary Science Letters*, 28, 155–171.

Dalziel, I.W.D. (1991). Pacific margins of Laurentia and East Antarctica-Australia as a conjugate rift pair: Evidence and implications for an Eocambrian supercontinent. *Geology*, 19, 598–601.

Direen, N.G., & Crawford, A.J. (2003a). Fossil seaward-dipping reflector sequences preserved in southeastern Australia: a 600 Ma volcanic passive margin in eastern Gondwanaland. *Journal of the Geological Society [London]*, 160, 985–990.

Direen, N.G., & Crawford, A.J. (2003b). The Tasman line: where is it, what is it, and is it Australia's Rodinian breakup boundary?. *Australian Journal of Earth Sciences*, 50, 491–502.

Di Vincenzo, G., Grande, A., & Rossetti, F. (2014). Paleozoic siliciclastic rocks from northern Victoria Land (Antarctica): Provenance, timing of deformation, and implications for the Antarctica-Australia connection. *Geological Society of America Bulletin*, 126, 1416–1438.

Di Vincenzo, G., Horton, F., & Palmeri, R. (2016). Protracted (~30 Ma) eclogite-facies metamorphism in northern Victoria Land (Antarctica): Implications for the geodynamics of the Ross/Delamerian Orogen. *Gondwana Research*, 40, 91–106.

Di Vincenzo, G., Palmeri, R., Talarico, F., Andriessen, P.A., & Ricci, C.A. (1997). Petrology and geochronology of eclogites from the Lanterman Range, Antarctica. *Journal of Petrology*, 38, 1391–1417.

Elliot, D.H., Fanning, C.M., & Hulett, S.R.W. (2015). Age provinces in the Antarctic craton: Evidence from detrital zircons in Permian strata from the Beardmore Glacier region, Antarctica. *Gondwana Research*, 28, 152–164.

Ernst, R.E., Buchan, K.L., & Campbell, I.H. (2005). Frontiers in large igneous province research. *Lithos*, 79, 271–297.

Estrada, S., Läufer, A., Eckelmann, K., Hofmann, M., Gärtner, A., & Linnemann, U. (2016). Continuous Neoproterozoic to Ordovician sedimentation at the East Gondwana margin – Implications from detrital zircons of the Ross Orogen in northern Victoria Land, Antarctica. *Gondwana Research*, 37, 426–448.

Fergusson, C.L., Henderson, R.A., Fanning, C.M., & Withnall, I.W. (2007). Detrital zircon ages in Neoproterozoic to Ordovician siliciclastic rocks, northeastern Australia: implications for the tectonic history of the East Gondwana continental margin. *Journal of the Geological Society [London]*, 164, 215–225.

Fergusson, C.L., Henderson, R.A., & Offler, R. (2017). Late Neoproterozoic to early Mesozoic sedimentary rocks of the Tasmanides, eastern Australia, in Mazumder, R., ed., Sediment provenance: Influences on compositional change from source to sink, Amsterdam, Elsevier, p. 325–369.

Fergusson, C.L., Offler, R., & Green, T.J. (2009). Late Neoproterozoic passive margin of East Gondwana: Geochemical constraints from the

Anakie Inlier, central Queensland, Australia. *Precambrian Research*, 168, 301–312.

Foden, J., Elburg, M.A., Dougherty-Page, J., & Burtt, A. (2006). The timing and duration of the Delamerian orogeny: Correlation with the Ross orogen and implications for Gondwana assembly. *Journal of Geology*, 114, 189–210.

Gibson, G.M., Champion, D.C., & Ireland, T.R. (2015). Preservation of a fragmented late Neoproterozoic–earliest Cambrian hyper-extended continental-margin sequence in the Australian Delamerian Orogen, in Gibson, G.M., Roure, F., & Manatschal, G., eds., *Sedimentary basins and crustal processes at continental margins: From modern hyper-extended margins to deformed ancient analogues*: London, Geological Society [London] Special Publication, 413, p. 269–299.

Glen, R.A., Fitzsimons, I.C.W., Griffin, W.L., & Saeed, A. (2017). East Antarctic sources of extensive Lower–Middle Ordovician turbidites in the Lachlan Orogen, southern Tasmanides, eastern Australia. *Australian Journal of Earth Sciences*, 64, 143–224.

Goodge, J.W., & Fanning, C.M. (2010). Composition and age of the East Antarctic Shield in eastern Wilkes Land determined by proxy from Oligocene-Pleistocene glaciomarine sediment and Beacon Supergroup sandstones, Antarctica. *Geological Society of America Bulletin*, 122, 1135–1159.

Goodge, J.W., Fanning, C.M., Norman, M.D., & Bennett, V.C. (2012). Temporal, isotopic and spatial relations of early Paleozoic Gondwana-margin arc magmatism, central Transantarctic Mountains, Antarctica. *Journal of Petrology*, 53, 2027–2065.

Goodge, J.W., & Finn, C.A. (2010). Glimpses of East Antarctica: Aeromagnetic and satellite magnetic view from the central Transantarctic Mountains of East Antarctica. *Journal of Geophysical Research*, 115, B09103.

Goodge, J.W., Myrow, P., Phillips, D., Fanning, C.M., & Williams, I.S. (2004). Siliciclastic record of rapid denudation in response to convergent-margin orogenesis, Ross Orogen, Antarctica, in Bernet, M., & Spiegel, C., eds., *Detrital thermochronology—Provenance analysis, exhumation, and landscape evolution of mountain belts*: Boulder, Colorado, Geological Society of America Special Paper 378, p. 105–126.

Goodge, J.W., Myrow, P., Williams, I.S., & Bowring, S. (2002). Age and provenance of the Beardmore Group, Antarctica: Constraints on Rodinia supercontinent breakup. *Journal of Geology*, 110, 393–406.

Goodge, J.W., Vervoort, J.D., Fanning, C.M., Brecke, D.M., Farmer, G.L., Williams, I.S., Myrow, P.M., & DePaolo, D.J. (2008). A positive test of East Antarctica–Laurentia juxtaposition within the Rodinia supercontinent. *Science*, 321, 235–240.

Goodge, J.W., Williams, I.S., & Myrow, P. (2004). Provenance of Neoproterozoic and lower Paleozoic siliciclastic rocks of the central Ross orogen, Antarctica: detrital record of rift-, passive-, and active-margin sedimentation. *Geological Society of America Bulletin*, 116, 1253–1279.

Greenfield, J.E., Musgrave, R.J., Bruce, M.C., Gilmore, P.J., & Mills, K.J. (2011). The Mount Wright Arc: A Cambrian subduction system developed on the continental margin of East Gondwana, Koonenberry Belt, eastern Australia. *Gondwana Research*, 19, 650–669.

Hagen-Peter, G., Cottle, J.M., Smit, M., & Cooper, A.F. (2016). Coupled garnet Lu–Hf and monazite U–Pb geochronology constrain early convergent margin dynamics in the Ross orogen, Antarctica. *Journal of Metamorphic Geology*, 34, 293–319.

Hawkesworth, C., Cawood, P., Kemp, T., Storey, C., & Dhuime, B. (2009). A matter of preservation. *Science*, 323, 49–50.

Hoffman, P.F. (1991). Did the breakout of Laurentia turn Gondwanaland inside-out?. *Science*, 252, 1409–1412.

Holm, O.H., Crawford, A.J., & Berry, R.F. (2003). Geochemistry and tectonic settings of meta-igneous rocks in the Arthur Lineament and surrounding area, northwest Tasmania. *Australian Journal of Earth Sciences*, 50, 903–918.

Ireland, T.R., Flöttmann, T., Fanning, C.M., Gibson, G.M., & Preiss, W.V. (1998). Development of the early Paleozoic Pacific margin of Gondwana from detrital-zircon ages across the Delamerian orogen. *Geology*, 26, 243–246.

Kim, T., Kim, Y., Cho, M., & Lee, J.I. (2019). *P–T* evolution and episodic zircon growth in barroisite eclogites of the Lanterman Range, northern Victoria Land, Antarctica. *Journal of Metamorphic Geology*, 37, 509–537.

Kim, Y., Kim, T., Lee, J.I., & Kim, S.J. (2017). SHRIMP U-Pb ages of zircon from banded gneisses and a leucocratic dyke in the Wilson Terrane, northern Victoria Land, Antarctica. *Journal of the Geological Society of Korea*, 53, 489–507 (in Korean with English abstract).

Kleinschmidt, G., & Tessensohn, F. (1987). Early Paleozoic westward directed subduction at the Pacific margin of Antarctica, in McKenzie, G.D., ed., *Gondwana six: Structure, tectonics and geophysics*: Washington, D.C., American Geophysical Union (AGU) Geophysical Monograph Series 40, p. 89–105.

Licht, K.J., & Palmer, E.F. (2013). Erosion and transport by Byrd Glacier, Antarctica during the Last Glacial Maximum. *Quaternary Science Reveiws*, 62, 32–48.

Ludwig, K.R. (2008). *User's manual for Isoplot 3.6: A geochronological toolkit for Microsoft Excel*, Berkeley Geochronology Center Special Publication (no. 4). Berkeley: Berkeley Geochronology Center. 77 pp.

Martin, E.L., Collins, W.J., & Kirkland, C.L. (2017). An Australian source for Pacific-Gondwanan zircons: Implications for the assembly of northeastern Gondwana. *Geology*, 45, 699–702.

Meffre, S., Direen, N.G., Crawford, A.J., & Kamenetsky, V. (2004). Mafic volcanic rocks on King Island, Tasmania: evidence for 579 Ma break-up in east Gondwana. *Precambrian Research*, 135, 177–191.

Meschede, M. (1986). A method of discriminating between different types of mid-ocean ridge basalts and continental tholeiites with the Nb–Zr–Y diagram. *Chemical Geology*, 56, 207–218.

Moores, E.M. (1991). Southwest U.S.-East Antarctic (SWEAT) connection: A hypothesis. *Geology*, 19, 425–428.

Paces, J.B., & Miller, J.D. (1993). Precise U-Pb ages of Duluth Complex and related mafic intrusions, northeastern Minnesota: Geochronological insights to physical, petrogenetic, paleomagnetic, and tectonomagmatic processes associated with the 1.1 Ga Midcontinent Rift system. *Journal of Geophysical Research*, 98, 13997–14013.

Paulsen, T.S., Deering, C., Sliwinski, J., Bachmann, O., & Guillong, M. (2016). Detrital zircon ages from the Ross Supergroup, north Victoria Land, Antarctica: Implications for the tectonostratigraphic evolution of the Pacific-Gondwana margin. *Gondwana Research*, 35, 79–96.

Preiss, W.V. (2000). The Adelaide Geosyncline of South Australia and its significance in Neoproterozoic continental reconstruction. *Precambrian Research*, 100, 21–63.

Rocchi, S., Bracciali, L., Di Vincenzo, G., Gemelli, M., & Ghezzo, G. (2011). Arc accretion to the early Paleozoic Antarctic margin of Gondwana in Victoria Land. *Gondwana Research*, 19, 594–607.

Sircombe, K.N. (1999). Tracing provenance through the isotope ages of littoral and sedimentary detrital zircon, eastern Australia. *Sedimentary Geology*, 124, 47–67.

Squire, R., Campbell, I., Allen, C., & Wilson, C. (2006). Did the Transgondwanan Supermountain trigger the explosive radiation of animals on Earth?. *Earth and Planetary Science Letters*, 250, 116–133.

Steiger, R.H., & Jäger, E. (1977). Subcommission on geochronology: Convention on the use of decay constants in geo- and cosmochronology. *Earth and Planetary Science Letters*, 36, 359–362.

Sun, S.s., & McDonough, W.F. (1989). Chemical and isotopic systematics of oceanic basalts: implications for mantle composition and processes, in Saunders, A.D., & Norry, M.J., eds., *Magmatism in the ocean basins*. Geological Society [London] Special Publication, 42, p. 313–345.

Turner, S., Haines, P., Foster, D., Powell, R., Sandiford, M., & Offler, R. (2009). Did the Delamerian orogeny start in the Neoproterozoic?. *Journal of Geology*, 117, 575–583.

Veevers, J.J., & Saeed, A. (2008). Gamburtsev Subglacial Mountains provenance of Permian–Triassic sandstones in the Prince Charles Mountains and offshore Prydz Bay: Integrated U–Pb and TDM ages and host-rock affinity from detrital zircons. *Gondwana Research*, 14, 316–342.

Weaver, S.D., Bradshaw, J.D., & Laird, M.G. (1984). Geochemistry of Cambrian volcanics of the Bowers Supergroup and implications for the Early Palaeozoic tectonic evolution of northern Victoria Land, Antarctica. *Earth and Planetary Science Letters*, 68, 128–140.

Williams, I.S. (1998). U-Th-Pb geochronology by ion microprobe. In M.A. McKibben, W.C. Shanks III, & W.I. Ridley (Eds.), *Applications of microanalytical techniques to understanding mineralizing processes,* Reviews in Economic Geology (v. 7, pp. 1–35). Littleton, CO: Society of Economic Geologists.

Winchester, J.A., & Floyd, P.A. (1977). Geochemical discrimination of different magma series and their differentiation products using immobile elements. *Chemical Geology*, 20, 325–343.

Wingate, M.T.D., Campbell, I.H., Compston, W., & Gibson, G.M. (1998). Ion microprobe U–Pb ages for Neoproterozoic basaltic magmatism in south-central Australia and implications for the breakup of Rodinia. *Precambrian Research*, 87, 135–159.

CHAPTER IV

Petrogenesis of manganiferous quartzite in the Lanterman Range, northern Victoria Land, Antarctica

ABSTRACT

Manganiferous quartzitic schist rarely occurs as thin layer intercalated within garnet–phengite quartzofeldspathic schists and gneisses enclosing the eclogites and garnet amphibolites in the Lanterman Range, northern Victoria Land, Antarctica. This peculiar rock was derived from chert-like pelagic sediment. Its positive Ce anomaly confirmed incorporation of ferromanganese deposits. On the basis of a close spatial relationship and similar times of deposition with the surrounding garnet–phengite metasedimentary rocks, the protolith of the manganiferous quartzite formed in continental slope to shelf of possible passive margin setting. Mineral assemblages represented by spessartine-rich garnet, piemontite-allanite-rich epidote, high-Si phengite, magnetite and quartz suggested greenschist to blueschist facies conditions, where the relatively high oxygen fugacity was maintained to preserve relict piemontite. Passive margin sedimentary packages were metamorphosed at middle Cambrian time in the context of the Ross orogeny.

Keywords: manganiferous quartzite, piemontite-allanite-epidote, deep sea sediment, high oxygen fugacity, high-*P* metamorphism, Ross orogeny

INTRODUCTION

Deep sea sediments enriched in manganese have been commonly reported as protoliths of spessartine-rich garnet-bearing quartzites worldwide. Among the manganiferous quartzites, fine-grained, yellowish lithologies mainly consisting of spessartine, mica and quartz have been extensively quarried for whetstone in the Stavelot Massif of Belgian Ardennes since 18th century because of their capability in polishing (Goemaere et al., 2016). These Belgian quartzites of Ordovician protolith age have been historically called as “coticule”. Recent review on the formation of coticule protolith in the Belgian type locality (Herbosch et al., 2016) suggested deep sea environments such as continental shelf and slope on the basis of their common intercalation within turbiditic sediments. Therefore, similar origin from oceanic environment is possibly applicable to other quartzite with high manganese concentration. Since the original description in Belgium, the occurrences of coticule have been extended to other regions with various age and metamorphic grade. The metamorphic grade of coticule varies from very low grade in anchizonal to epizonal regime, to granulite (Thomson, 2001) and eclogite facies (Reinecke, 1998). Hereafter, the manganiferous quartzites or quartzitic schists are preferred to the descriptive term coticule.

Geological setting, sedimentary environment and formation process of the manganiferous quartzite protolith is widely debated (e.g. Izadyar et al., 2003). Manganese could easily become mobile when water-rock interaction

such as that of mid-ocean ridge basalts leads Mn and Fe soluble in hydrothermal fluids (Edmond et al., 1982). Ferromanganese nodules or crusts containing hydrothermal Mn could be a direct source of enrichment in pelagic sediments (Reinecke et al., 1985). Origin of silica in the manganiferous silica-rich rocks has been generally considered to be biogenic (e.g. Mottana, 1986), but continental input of variable amounts of siliciclastics also contributes to the formation of manganiferous rocks (Coombs et al., 1985; Reinecke et al., 1985; Mottana, 1986). Therefore, the manganese enrichment should depend on the distance from the hydrothermal source such as spreading ridges, the amount of incorporation of the deep sea manganese deposits and the degree of dilution by sediments of biogenic and terrigenous origins (Edmond et al., 1982; Mottana, 1986). Thus, the manganiferous silica-rich rocks primarily consist of terrigenous, biogenic, hydrothermal and hydrogenous components (Coombs et al., 1985; Reinecke et al., 1985; Mottana, 1986; Huebner et al., 1992).

The manganiferous quartzites have been reported from well-known high-*P* terranes associated with subduction of oceanic materials; the Otago schist, New Zealand (Coombs et al., 1985), European Alps (Reinecke, 1998) and Sanbagawa belt, Japan (Izadyar et al., 2003). Mineral assemblages of this peculiar rock type commonly consist of a variety of Mn-bearing phases, such as braunite ($MnMn^{3+}{}_6SiO_{12}$), rhodochrosite ($MnCO_3$), sursassite ($MnAl_3Si_3O_{11}(OH)_3$), tephroite (Mn_2SiO_4), carpholite ($MnAl_2Si_2O_6(OH)_4$), piemontite ($Ca_2Al_2Mn^{3+}Si_3O_{12}(OH)$) and spessartine ($Mn_3Al_2Si_3O_{12}$).

Piemontite-bearing quartzitic schists have attracted much attention because of their unusual mineral associations such as talc–phengite assemblage, which is now considered as an indicator of high-*P* metamorphism (Abraham and Schreyer, 1976; Schreyer, 1985; Massonne and Schreyer, 1989). Even ultrahigh-*P* conditions were confirmed in the manganiferous quartzite layer at Lago di Cignana, the Zermatt-Saas zone of western Alps (Reinecke, 1991, 1998). In addition, the preservation of high-*P*-*T* manganian (Mn^{3+}-bearing) silicate assemblages requires high oxygen fugacity (f_{O2}) during the entire metamorphic cycle (e.g. Abs-Wurmbach and Peters, 1999; Jöns and Schenk, 2004). Because of their rare occurrence and minor amounts, metamorphic and tectonic evolution of the manganiferous quartzites is largely unknown.

In the Lanterman Range of northern Victoria Land, Antarctica, manganiferous quartzite containing piemontite occurs as layer alternating with garnet-phengite-bearing metasedimentary rocks. In order to unravel evolutionary history of this manganiferous quartzite, whole-rock geochemistry, thermobarometry and sensitive high-resolution ion microprobe (SHRIMP) U-Pb geochronology were investigated. In particular, epidote group minerals and their zonation in Mn^{3+} and rare earth element (REE) contents were analyzed. The aims of this study are: (1) to prove deep sea sediment origin of the protolith and cause of manganese enrichment, (2) to constrain possible terrigenous input to the pelagic sediment and its provenance and (3) to unravel metamorphic evolution associated with the Ross orogeny.

GEOLOGICAL BACKGROUND

Northern Victoria Land, occupying the Pacific end of the Transantarctic Mountains, is a part of the late Neoproterozoic–early Paleozoic Ross orogen (Figure IV-1a). The onset of convergent tectonics was near-synchronous with the waning stage of the Gondwana formation (*c.* 570–530 Ma; for example, Cawood, 2005; Boger, 2011). During the westward subduction of paleo-Pacific plate, three fault-bounded blocks, the Wilson, Bowers and Robertson Bay terranes from onshore to offshore, were amalagamated to form of NVL (Figure IV-1b; GANOVEX Team, 1987; Kleinschmidt and Tessensohn, 1987). The Wilson Terrane forms a crystalline basement of continental arc setting, and comprises metasedimentary rocks of the Wilson Metamorphic Complex (WMC) primarily derived from siliciclastic lithologies of a former passive margin (e.g. Estrada et al., 2016 Paulsen et al., 2016), and intruding syn- to post-orogenic plutons of middle Cambrian to Early Ordovician age, the Granite Harbour Intrusives (Borg and Stump, 1987; Bomparola et al., 2007). The Bowers Terrane is an elongate belt (~20–50 km wide) of middle to late Cambrian volcanic-sedimentary sequences (Weaver et al., 1984). The Robertson Bay Terrane comprises variably folded, late Cambrian–Early Ordovician turbiditic sequences thicker than 3,000 m (Dallmeyer and Wright, 1992).

The manganiferous quartzite occurs in the Lanterman Range, which occupies the boundary between the Wilson and Bowers terranes (Figure IV-

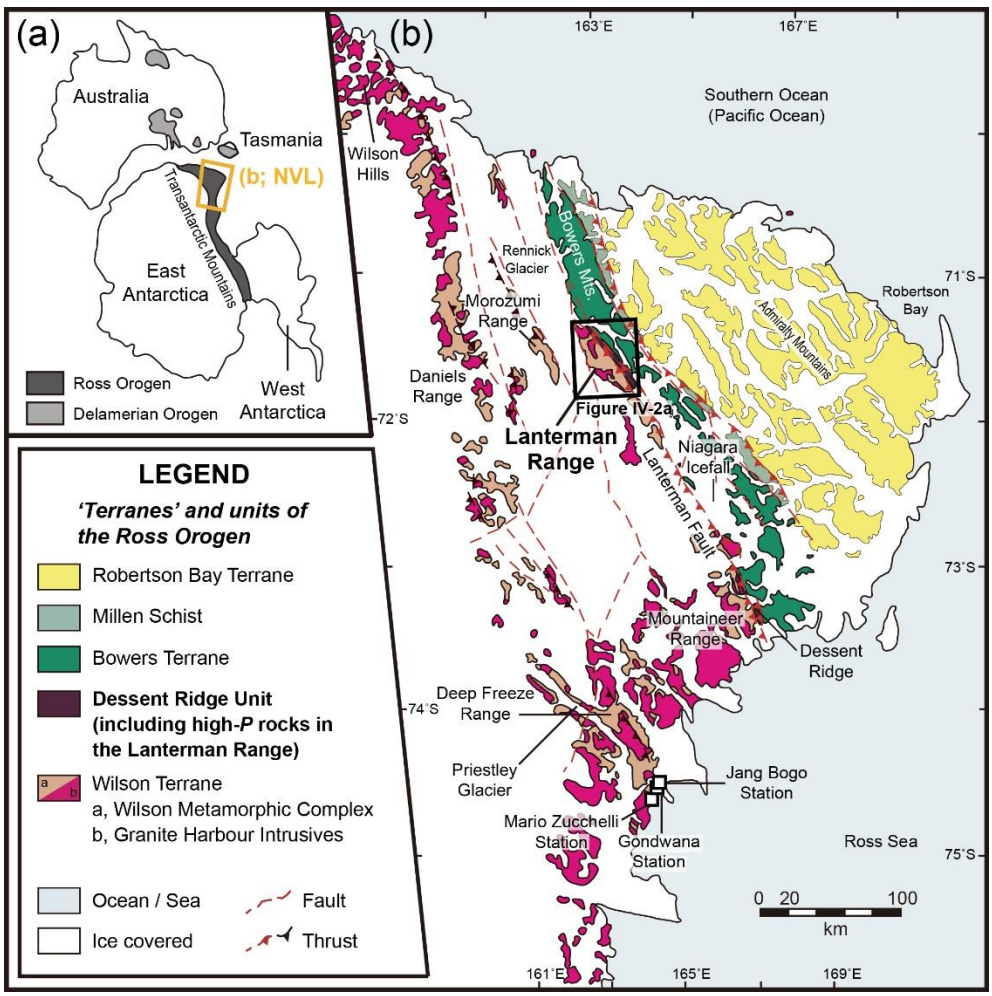

Figure IV-1. (a) Schematic map showing an Antarctic Ross and Australian Delamerian orogens prior to the breakup of Gondwana. An orange box denotes the location of northern Victoria Land (NVL) enlarged in (b). (b) Tectonic province map of NVL. The region in black box is enlarged in Figure IV-2a. Post-Ross rocks are omitted for clarity (modified from Kim et al., 2019).

1b). The range is dominated by the Wilson crystalline rocks (the WMC and Granite Harbour Intrusives; Talarico et al., 1998), but the granitoids are absent along its easternmost part where pristine eclogites were discovered in the contact with the Bowers Terrane (Ricci et al., 1996). The high-*P* metamafic and ultramafic rocks only occur along a ridge near the Husky Pass, which has served as an obvious target for many previous studies (Figure IV-2a; Di Vincenzo et al., 1997, 2016; Palmeri et al., 2007, 2011; Kim et al., 2019). The Lanterman Range eclogites defined in Kim et al. (2019) commonly occur in the field as lenses or boudins, enclosed by (garnet–)phengite-bearing metasedimentary country rocks. Metamorphic evolution of the Lanterman Range eclogites are summarized in Kim et al. (2019). Timing of prograde and peak metamorphism was constrained to be at *c.* 515 Ma and *c.* 500 Ma, respectively (Kim et al., 2019). The latter is consistent with Sm-Nd errorchron results obtained from retrograde 'hot' eclogite (Di Vincenzo et al., 1997). Retrograde cooling and exhumation rates under the amphibolite facies conditions were estimated to be >30 °C/Ma and 2–5 km/Ma respectively, on the basis of ^{40}Ar-^{39}Ar ages of amphibole (Di Vincenzo et al., 2001; Di Vincenzo and Palmeri, 2001; Goodge and Dallmeyer, 1996).

Metamorphic evolution of the garnet–phengite schists and gneisses was delineated by Palmeri et al. (2003, 2011). These high-*P* felsic rocks preserve prograde amphibolite facies at ~5–8 kbar and 500 ± 40 °C and alleged peak stages at the coesite stability field. The latter overlaps that of

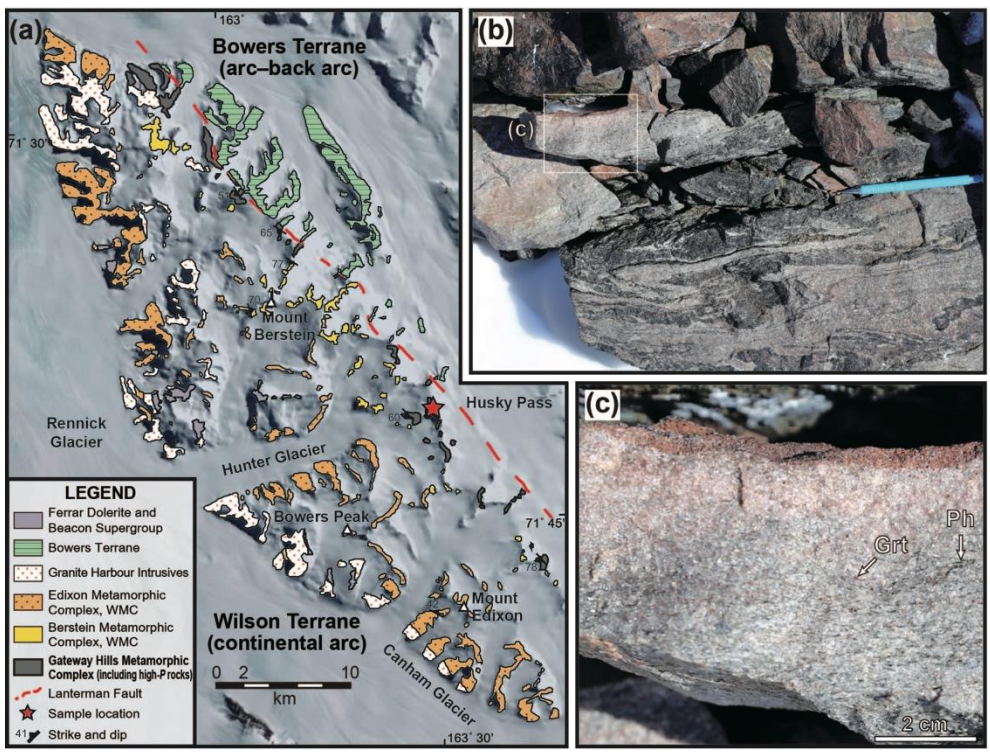

Figure IV-2. (a) Geological map of the Lanterman Range, northern Victoria Land, shown over the Google Earth satellite image. A red star denotes the eclogite sample locality at a ridge near the Husky Pass, corresponding to the 'outcrop 4' of Capponi et al. (1997). WMC, Wilson Metamorphic Complex. (b) Outcrop photograph showing complex structural relationships between amphibolitic and garnet–phengite-bearing felsic lithologies. A white box is enlarged in (c). A pen for scale is ~15 cm. (c) A manganiferous quartzite layer. Pinkish garnet and dark brown flakes of phengite are noticeable.

'hot' eclogite (Di Vincenzo et al., 1997). Retrograde path was defined on the basis of phengite breakdown to biotite–plagioclase symplectite, escaping solidus region (Palmeri et al., 2003). The celadonite-rich phengite yielded $^{40}Ar/^{39}Ar$ ages of *c.* 500 Ma (Di Vincenzo et al., 2001), whereas white mica neoblasts parallel to or discordant to the foliation gave 478–482 Ma, which is coeval with biotite recrystallization (Di Vincenzo et al., 2001). Apart from these garnet–phengite quartzofeldspathic rocks, metamorphic evolution and protolith origin of the manganiferous quartzites have not been investigated.

SAMPLE DESCRIPTION AND PETROGRAPHY

The manganiferous quartzite sample was collected from the northern part of 'outcrop 4' in the geological map of Capponi et al. (1997), where Di Vincenzo et al. (2016) and Kim et al. (2019) reported the 'tepid' eclogite. This site is situated several hundred metres northward from the 'hot' eclogite locality (Di Vincenzo et al., 1997). The manganiferous quartzitic schist shows a pink tinge to the naked eye, and rarely occurs as <10 cm thick level interleaved within amphibolitic schist and garnet–phengite schist (Figure IV-2b,c). The quartzite is fine- to medium-grained and strongly-foliated. Mineral assemblages of the sample (151223-1F) are represented by piemontite/epidote + garnet + magnetite + phengite + chlorite + quartz, together with subordinate amounts of accessory zircon, monazite, apatite and tourmaline (Figure IV-3a). Three types of garnet porphyroblasts are identified on the basis of the size and morphology. The first type of garnet

porphyroblasts (Grt I) is subhedral, and on average ~500 μm in the longest dimension (Figures IV-3b and IV-4a); it contains small amounts of inclusions such as rutile and quartz. Skeletal garnet porphyroblasts (Grt II) are coarser-grained than Grt I and commonly associated with chlorite (Figures IV-3c and IV-4b). Fine-grained hypidio- to xenoblastic garnet porphyroblasts (Grt III, mostly <200 μm) are inclusion-poor, and commonly elongate in shape with their long dimension subparallel to the foliation (Figure IV-3d). All types of garnet porphyroblasts are often typified by higher intensity of backscattered electron image at the outer part or rim. Pale brownish epidote group mineral is mostly epidote, but rarely preserves prominent compositional zonation consisting of piemontite core, allanite mantle and epidote rim (Figures IV-3a,b and IV-5). The core encloses quartz, and Mn silicate phases such as near-end member tephroite (Mn_2SiO_4). Magnetite is commonly elongate in shape (Figure IV-3a), and characterized by complex exsolution texture composed of Ti oxide minerals such as (Figure IV-4a). Rutile, ilmenite and pyrophanite ($MnTiO_3$) occur as inclusion within magnetite. Phengite flakes largely vary in their grain size, from 300 μm to 10 mm in the longest dimension. Quartz is commonly granoblastic and medium-grained (~500 μm on average), showing moderately-oriented structure parallel to the foliation (Figure IV-3). Weak deformation bands and undulose extinction are observed in quartz. Secondary K-feldspar and albite together form discrete bands after phengite (Figure IV-3b,c).

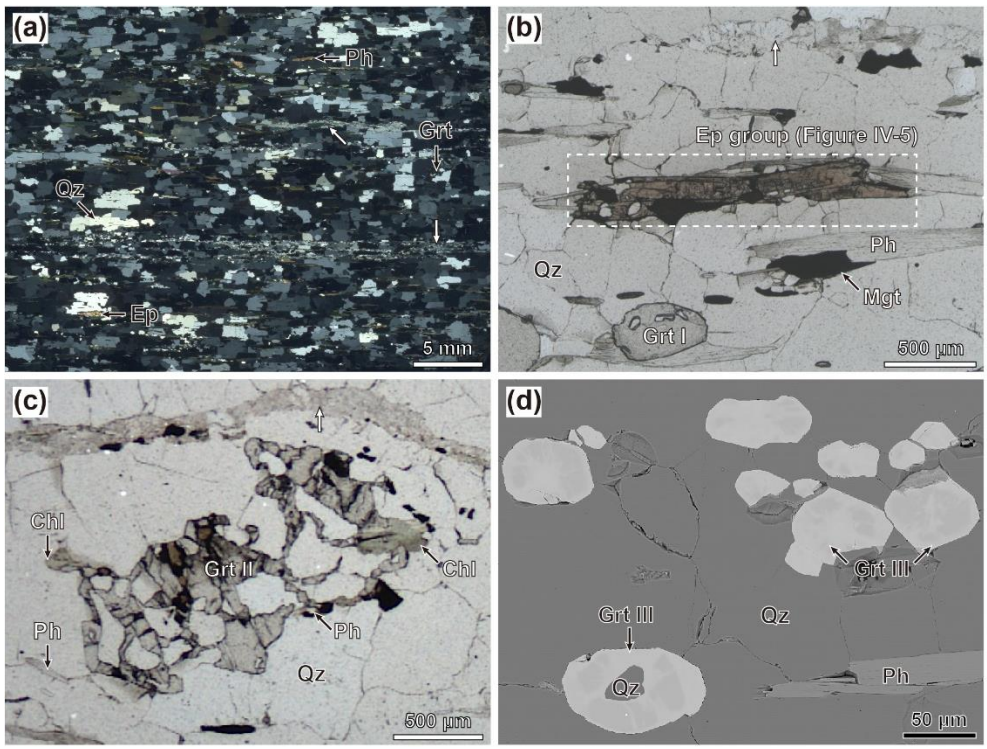

Figure IV-3. Photomicrographs (a–c) and backscattered electron image (BEI; d) of the manganiferous quartzitic schist showing mineral parageneses and occurrences of garnet porphyroblasts. Photomicrographs were taken under cross- (a) and plane-polarized light (b, c). White arrows denote albite–K-feldspar band after phengite. (a) An eclogite sample 151223-1F, mainly consisting of garnet, epidote group mineral, phengite, magnetite, chlorite and quartz. (b) Euderal piemontite porphyroblast overgrown by allanite and epidote. The X-ray chemical maps of the grain are shown in Figure IV-5. Subhedral Grt I includes quartz. (c) Xenoblastic Grt II partly mantled by chlorite. The X-ray chemical maps of the grain are shown in Figure IV-4b. (d) Fine-grained Grt III. The grains are elongate in shaped parallel to the foliation. Islands of low BEI intensity are surrounded by domains of high BEI intensity. Mineral abbreviations in this chapter are after Whitney and Evans (2010).

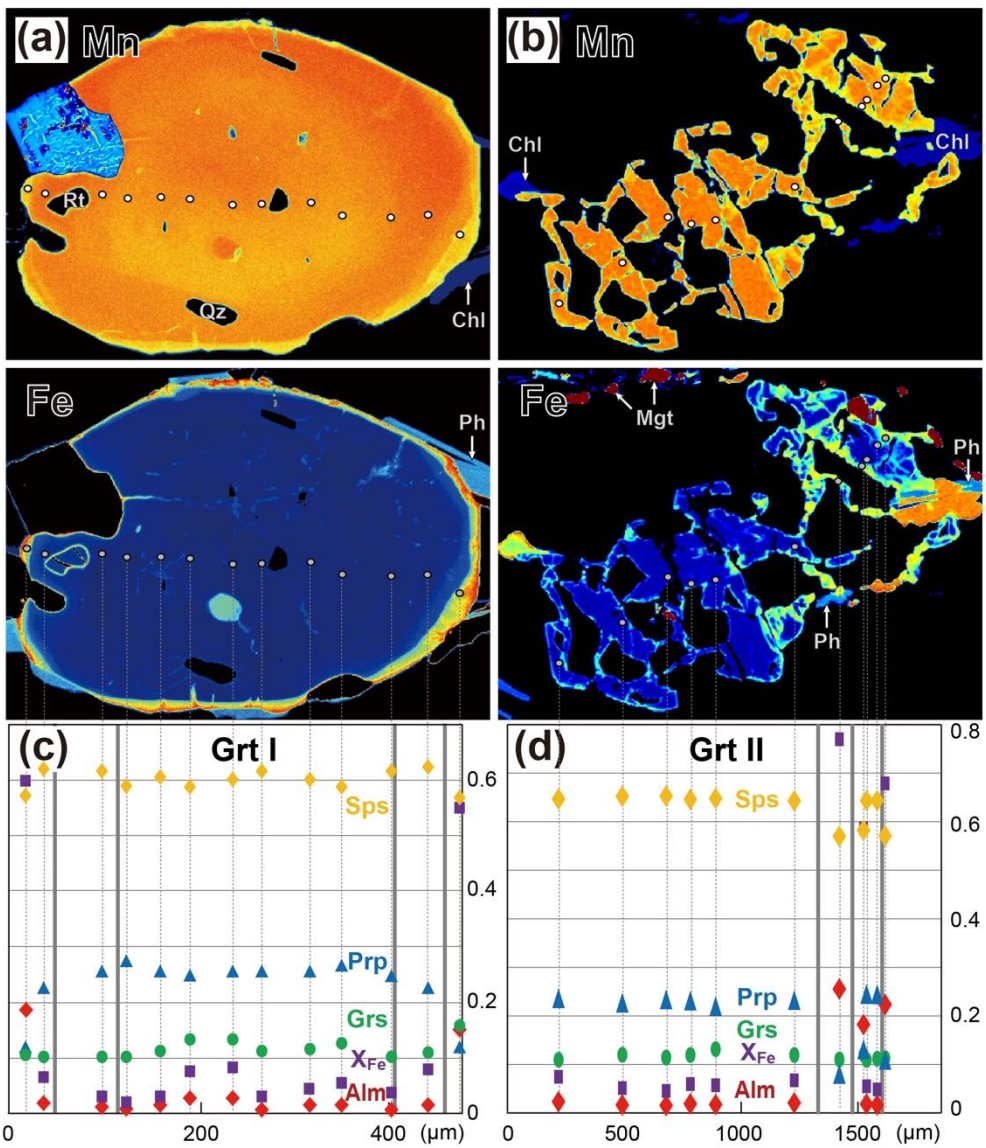

Figure IV-4. X-ray maps (a, b) and compositional profiles (c, d) of garnet porphyroblasts (Grt I and II). The Ti X-ray map for magnetite is shown with intensity colors. Relatively homogeneous cores are surrounded by thin rim with abrupt Fe enrichment. See text for further details.

Figure IV-5. Backscattered electron image and X-ray maps (a) and compositional profile (b) of euhedral porphyroblast of epidote group mineral. Four distinct compositional domains are defined on the basis of piemontite, epidote and allanite contents. A white arrow in the Mg map denotes the celadonite zonation of phengite.

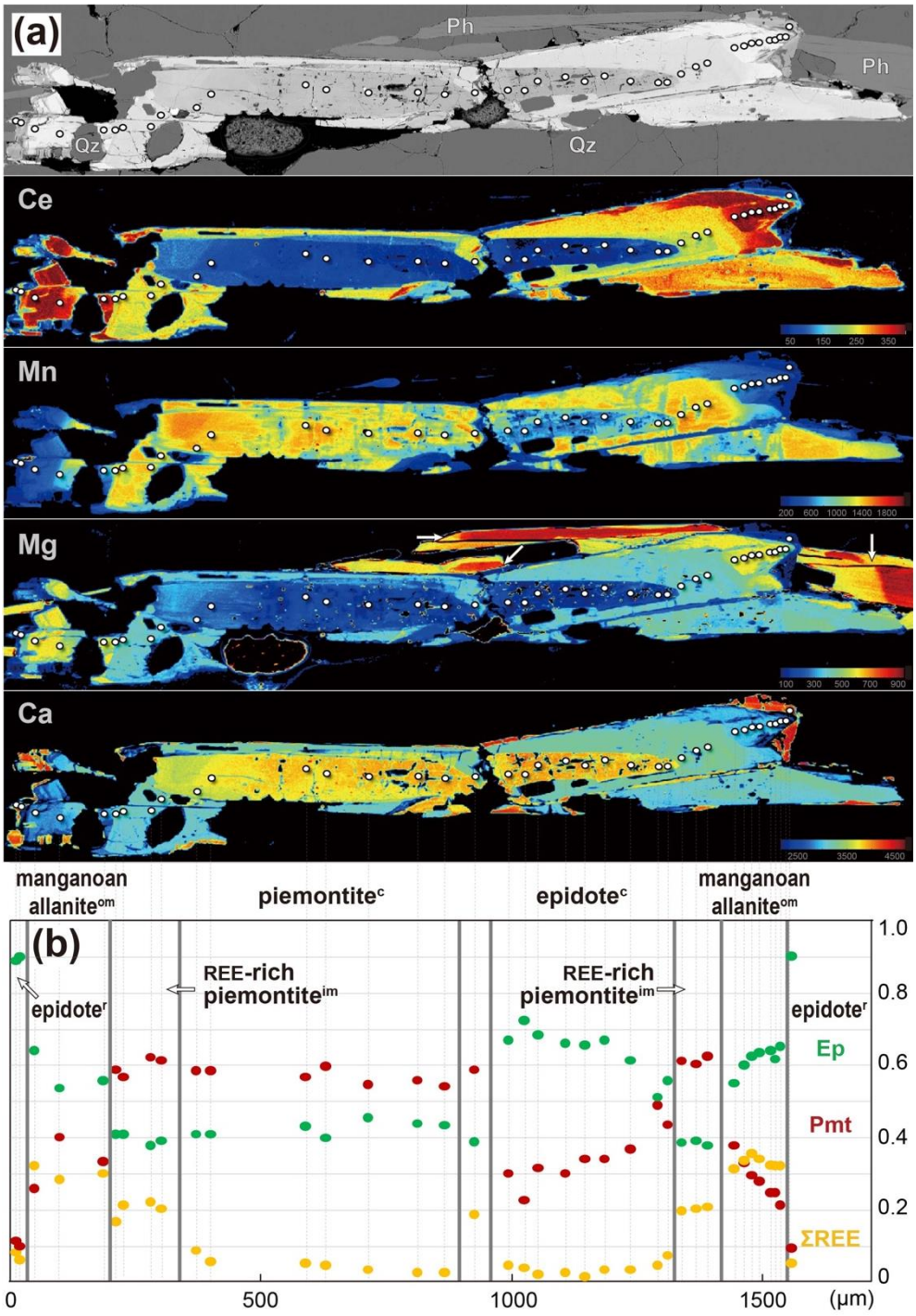
(a)
Ph
Ph
Qz
Qz
Ce
50 150 250 350
Mn
200 600 1000 1400 1800
Mg
100 300 500 700 900
Ca
2500 3500 4500
manganoan allanite^om
piemontite^c
epidote^c
manganoan allanite^om
(b)
epidote^r
REE-rich piemontite^im
REE-rich piemontite^im
epidote^r
Ep
Pmt
ΣREE
1.0
0.8
0.6
0.4
0.2
0
0
500
1000
1500
(μm)

ANALYTICAL METHODS

Mineral compositions were analysed using a JEOL JXA-8530F field-emission electron microprobe housed at the Korea Polar Research Institute, with 15 kV accelerating voltage, 10 nA beam current, 5 μm beam diameter and 20 s counting times. The compositions of epidote group minerals rich in REE were measured following the analytical conditions of Kim et al. (2009). Standard materials used for the calibration include natural silicates and synthetic oxides. Data acquisition and reduction were performed using the ZAF matrix correction. The X-ray mapping of garnet was conducted with 15 kV accelerating voltage, 500 nA beam current, 50 ms dwell time per pixel, 3 μm step size and focused beam. Whole-rock composition of manganiferous quartzite was determined by the inductively-coupled plasma optical emission spectroscopy at the Actlabs, Ontario, Canada, employing a lithium metaborate/tetraborate fusion.

Zircon separates were collected from a manganiferous quartzite (sample 151223-1F), using the heavy-liquid technique of Cheong et al. (2013), and were mounted in epoxy disc with SL13 and FC-1 standard zircon crystals. The former was use for measuring the U concentration (238 ppm; Claoué-Long et al., 1995), and the latter for calibrating $^{206}Pb/^{238}U$ ratios ($^{206}Pb^{*}/^{238}U$ = 0.1859; Paces and Miller, 1993). The cathodoluminescence (CL) images of zircon crystals were obtained using a JEOL JSM-6610LV scanning electron microscope (SEM) housed at the Korea Basic Science Institute (KBSI). Using the energy dispersive

spectroscopy system attached to the SEM, mineral inclusions inside zircon were also identified. The U-Th-Pb isotopic compositions of zircon were measured using the KBSI SHRIMP-IIe. The analytical protocol followed that of Williams (1998). All isotopes were measured using a primary O_2^- beam with ~3–5 nA and ~25 μm diameter spot. Common Pb contributions to total Pb counts were corrected using the ^{207}Pb correction method based on the Pb/U concordance and model common Pb composition (Cumming and Richards, 1975; Williams, 1998). The isotopic data were reduced using the Prawn/Lead 6.5.5 software (written communication, T. Ireland, 1996), and were plotted using the program Isoplot/Ex (Ludwig, 2008).

MINERAL CHEMISTRY

Garnet, epidote group minerals, phengite, chlorite, magnetite, ilmenite, pyrophanite and feldspar in the manganiferous quartzite sample (151223-1F) were analysed in order to determine their equilibrium compositions. Representative analyses of minerals are given in Table IV-1.

Garnet

Garnet porphyroblasts in the manganiferous quartzite sample are spessartine-rich and show near-constant grossular contents (Grs = $Ca/(Fe^{2+} + Mg + Ca + Mn)$ = 0.10–0.15). The Grt I preserves inner domain or core of relatively homogeneous composition (Sps = $Mn/(Fe^{2+} + Mg + Ca + Mn)$ = 0.58–0.63; $X_{Fe} = Fe^{2+}/(Fe^{2+} + Mg)$ = 0.07–0.12; Prp = $Mg/(Fe^{2+} + Mg +$

Table IV-1. Representative analyses of minerals in manganiferous quartzite (sample 151223-1F).

mineral	Garnet											
	Grt I c		Grt I r		Grt II id		Grt II od		Grt III id		Grt III od	
SiO_2	38.57	38.45	37.65	38.18	38.71	38.84	37.52	37.88	38.32	38.77	38.46	37.94
TiO_2	0.37	0.02	0.00	0.14	0.01	0.11	0.04	0.07	0.03	0.08	0.04	0.09
Al_2O_3	21.58	21.71	21.30	21.51	21.85	21.97	21.19	21.42	21.53	21.83	21.76	21.38
Cr_2O_3	b.d.	0.02	b.d.	b.d.	0.03	b.d.	b.d.	b.d.	b.d.	b.d.	0.03	0.04
FeO*	1.44	0.87	6.72	8.65	1.18	1.25	7.97	11.85	4.05	5.60	12.45	11.33
MnO	28.41	27.53	25.58	25.23	29.40	29.03	25.69	25.10	25.45	25.97	23.18	23.41
MgO	5.87	6.65	3.16	3.09	6.01	5.87	3.17	1.89	5.88	5.11	2.50	2.42
CaO	4.20	4.40	5.42	4.43	3.78	4.10	4.03	3.68	4.33	4.16	4.47	4.63
Na_2O	0.05	0.02	0.02	0.01	b.d.	0.08	0.03	b.d.	0.06	b.d.	0.04	b.d.
K_2O	b.d.	b.d.	0.01	b.d.	b.d.	b.d.	b.d.	0.01	b.d.	b.d.	b.d.	0.02
Total	99.77	99.67	100.23	100.34	100.07	99.71	99.65	100.00	99.65	100.02	100.44	99.46
Cations per 12 oxygens												
Si	3.00	3.00	3.00	3.00	3.00	3.00	3.00	3.00	3.00	3.00	3.00	3.00
Al	1.98	1.99	2.00	1.99	1.99	2.00	2.00	2.00	1.99	1.99	2.00	1.99
Cr	b.d.	0.00	b.d.	b.d.	0.00	b.d.	b.d.	b.d.	b.d.	b.d.	0.00	0.00
Ti	0.02	0.00	0.00	0.01	0.00	0.01	0.00	0.00	0.00	0.00	0.00	0.01
Fe^{2+}	0.09	0.06	0.45	0.57	0.08	0.08	0.53	0.78	0.27	0.36	0.81	0.75

Mn	1.87	1.82	1.72	1.68	1.93	1.90	1.74	1.68	1.69	1.70	1.53	1.57
Mg	0.68	0.77	0.38	0.36	0.69	0.68	0.38	0.22	0.69	0.59	0.29	0.29
Ca	0.35	0.37	0.46	0.37	0.31	0.34	0.34	0.31	0.36	0.35	0.37	0.39
Na	0.01	0.00	0.00	0.00	b.d.	0.01	0.00	b.d.	0.01	b.d.	0.01	0.00
K	b.d.	b.d.	0.00	b.d.	b.d.	b.d.	b.d.	0.00	b.d.	b.d.	b.d.	0.00
Total	8.00	8.01	8.01	7.99	8.00	8.00	8.00	8.00	8.01	8.00	8.01	8.00
X_{Fe}	0.12	0.07	0.54	0.61	0.10	0.11	0.58	0.78	0.28	0.38	0.74	0.72
Alm	0.03	0.02	0.15	0.19	0.03	0.03	0.18	0.26	0.09	0.12	0.27	0.25
Prp	0.23	0.26	0.12	0.12	0.23	0.23	0.13	0.07	0.23	0.20	0.10	0.10
Grs	0.12	0.12	0.15	0.13	0.10	0.11	0.12	0.10	0.12	0.12	0.12	0.13
Sps	0.62	0.60	0.57	0.56	0.64	0.63	0.58	0.56	0.56	0.57	0.51	0.52

*Total Fe as FeO.
b.d., below detection limit; c, core; r, rim; id, inner domain; od, outer domain; $X_{Fe} = Fe^{2+}/(Fe^{2+} + Mg)$; Alm = Fe^{2+}/M, Prp = Mg/M, Grs = Ca/M, and Sps = Mn/M, where M = (Fe^{2+} + Mg + Ca + Mn).

Table IV-1. Continued.

mineral	Epidote group mineral							
	core		inner mantle		outer mantle		rim	
SiO_2	37.86	38.09	36.32	36.38	35.67	35.39	38.07	38.00
TiO_2	0.02	0.01	0.02	0.02	0.05	0.05	0.00	0.02
Al_2O_3	23.28	22.64	20.09	20.37	20.48	20.14	22.24	22.81
Cr_2O_3	0.00	0.00	0.00	0.00	0.00	0.00	0.00	0.00
FeO*	6.10	9.67	5.97	6.27	7.21	7.58	11.85	10.63
MnO	7.47	5.02	9.17	8.82	5.37	3.53	1.32	1.33
MgO	0.22	0.22	1.31	1.15	1.92	2.10	0.23	0.32
CaO	20.20	19.96	16.61	16.93	15.09	14.69	21.59	21.64
Na_2O	0.00	0.02	0.00	0.00	0.12	0.40	0.08	0.01
SrO	0.76	0.87	0.36	0.36	0.41	0.23	0.20	0.00
Y_2O_3	0.04	0.03	0.01	0.00	0.03	0.00	0.00	0.00
La_2O_3	0.29	0.06	0.97	0.72	1.57	1.56	0.32	0.51
Ce_2O_3	0.42	0.39	5.32	4.35	6.98	8.72	1.47	1.73
Pr_2O_3	0.03	0.00	0.21	0.15	0.35	0.45	0.05	0.10
UO_2	0.10	0.10	0.81	1.00	1.60	1.64	0.34	0.35
Nd_2O_3	0.00	0.00	0.00	0.00	0.00	0.00	0.00	0.00
Sm_2O_3	0.00	0.00	0.09	0.05	0.00	0.13	0.08	0.00

Gd_2O_3	0.00	0.00	0.00	0.05	0.00	0.00	0.01	0.04
ThO_2	0.02	0.03	0.24	0.14	0.36	0.34	0.06	0.12
PbO	0.31	0.26	0.25	0.15	0.14	0.16	0.12	0.10
Total	97.13	97.36	97.75	96.92	97.34	97.14	98.03	97.71
Cations per 12.5 oxygens								
Si	2.91	2.90	2.89	2.90	2.93	2.93	2.87	2.90
Al^{IV}	0.09	0.10	0.11	0.10	0.07	0.07	0.13	0.10
Al^{VI}	2.02	2.00	1.99	2.00	2.06	2.07	1.96	2.00
Cr	0.00	0.00	0.00	0.00	0.00	0.00	0.00	0.00
Ti	0.00	0.00	0.00	0.00	0.00	0.00	0.00	0.00
Fe^{3+}	0.44	0.70	0.42	0.45	0.52	0.55	0.85	0.77
Mn^{3+}	0.55	0.37	0.66	0.64	0.40	0.26	0.10	0.10
Mg	0.03	0.03	0.17	0.15	0.25	0.27	0.03	0.04
Ca	1.88	1.84	1.51	1.55	1.41	1.37	1.98	2.00
Na	0.00	0.00	0.00	0.00	0.02	0.07	0.01	0.00
Sr	0.04	0.04	0.02	0.02	0.02	0.01	0.01	0.00
Y	0.00	0.00	0.00	0.00	0.00	0.00	0.00	0.00
La	0.01	0.00	0.03	0.02	0.05	0.05	0.01	0.02
Ce	0.01	0.01	0.17	0.14	0.22	0.28	0.05	0.05

Pr	0.00	0.00	0.01	0.00	0.01	0.01	0.00	0.00
U	0.00	0.00	0.02	0.02	0.03	0.03	0.01	0.01
Nd	0.00	0.00	0.00	0.00	0.00	0.00	0.00	0.00
Sm	0.00	0.00	0.00	0.00	0.00	0.00	0.00	0.00
Gd	0.00	0.00	0.00	0.00	0.00	0.00	0.00	0.00
Th	0.00	0.00	0.00	0.00	0.01	0.01	0.00	0.00
Pb	0.01	0.01	0.01	0.00	0.00	0.00	0.00	0.00
Total	8.00	8.00	8.00	8.00	8.00	8.00	8.00	8.00
REEs	0.02	0.01	0.20	0.17	0.28	0.35	0.06	0.08
X_{Czo}	0.02	0.00	0.00	0.00	0.06	0.07	0.00	0.00
X_{Ep}	0.44	0.66	0.39	0.41	0.54	0.63	0.90	0.89
X_{Pmt}	0.54	0.34	0.61	0.59	0.40	0.30	0.10	0.11

*Total Fe as FeO.
b.d., below detection limit; $X_{Czo} = (Al^{VI} – 2)/M$, $X_{Ep} = Fe^{3+}/M$, $X_{Pmt} = Mn^{3+}/M$, where $M = (Fe^{3+} + Mn^{3+} Al^{VI} – 2)$.

Table IV-1. Continued.

mineral	Phengite			Chlorite		Plagio clase	K-feldspar		Magnetite		Ilmenite	Pyrophanite	
	inner		outer	core	rim								
SiO_2	49.48	48.04	47.80	28.57	27.00	67.10	64.13	SiO_2	0.06	0.08	0.06	0.04	0.09
TiO_2	0.47	0.86	0.28	b.d.	0.12	b.d.	0.02	TiO_2	7.47	6.05	44.00	48.19	37.73
Al_2O_3	27.14	29.13	28.10	20.04	21.10	20.73	18.61	Al_2O_3	0.20	0.06	0.10	0.06	0.04
Cr_2O_3	0.02	0.04	0.00	0.03	b.d.	b.d.	b.d.	Cr_2O_3	0.00	0.00	0.00	0.01	0.01
FeO*	3.96	3.48	4.78	10.50	14.32	0.06	0.01	Fe_2O_3**	54.27	57.50	13.91	6.73	26.16
MnO	0.01	0.07	0.22	2.37	1.68	0.03	0.00	FeO**	37.45	36.83	39.35	2.60	5.46
MgO	2.99	2.52	2.39	23.38	21.22	0.01	0.00	MnO	0.63	0.15	0.27	40.20	28.20
CaO	0.03	0.01	0.01	0.04	0.02	0.96	0.00	MgO	0.03	0.00	0.01	0.04	0.01
Na_2O	0.65	0.59	0.15	0.03	0.02	11.04	0.20	CaO	0.00	0.00	0.02	0.01	0.00
K_2O	10.42	10.55	11.15	0.01	0.01	0.06	16.99	Na_2O	0.00	0.03	0.00	0.00	0.00
Total	95.15	95.30	94.88	84.97	85.49	100.00	100.04	K_2O	0.00	0.00	0.00	0.02	0.01
								Total**	100.12	100.71	97.72	97.91	97.72
Cations per 11, 14, 8, 4 and 3 oxygens for phengite, chlorite, feldspar, magnetite and ilmenite-pyrophanite, respectively.													
Si	3.34	3.24	3.27	2.89	2.77	2.94	2.98	Si	0.00	0.00	0.00	0.00	0.00
Al^{IV}	0.66	0.76	0.73	1.11	1.23	0.06	0.02	Ti	0.21	0.17	0.86	0.93	0.74
Al^{VI}	1.51	1.56	1.54	1.28	1.32	1.01	1.00	Al	0.01	0.00	0.00	0.00	0.00
Cr	0.00	0.00	0.00	0.00	b.d.	b.d.	b.d.	Cr	0.00	0.00	0.00	0.00	0.00

Ti	0.02	0.04	0.01	b.d.	0.01	b.d.	0.00	Fe^{3+}	1.56	1.64	0.27	0.13	0.51
Fe^{3+}	-	-	-	0.00	0.00	-	-	Fe^{2+}	1.19	1.17	0.86	0.06	0.12
Mn^{3+}	-	-	-	-	-	-	-	Mn	0.02	0.00	0.01	0.88	0.62
Fe^{2+}	0.22	0.20	0.27	0.89	1.23	0.00	0.00	Mg	0.00	0.00	0.00	0.00	0.00
Mn	0.00	0.00	0.01	0.20	0.15	0.00	0.00	Ca	0.00	0.00	0.00	0.00	0.00
Mg	0.30	0.25	0.24	3.53	3.24	0.00	0.00	Na	0.00	0.00	0.00	0.00	0.00
Ca	0.00	0.00	0.00	0.00	0.00	0.04	0.00	K	0.00	0.00	0.00	0.00	0.00
Na	0.09	0.08	0.02	0.01	0.00	0.94	0.02	Total	3.00	3.00	2.00	2.00	2.00
K	0.90	0.91	0.97	0.00	0.00	0.00	1.00	X_{Usp}	0.22	0.18		-	-
Total	7.04	7.05	7.08	9.92	9.95	5.00	5.03	X_{Pph}	-	-	0.01	0.88	0.62
X_{Fe}	0.43	0.44	0.53	0.20	0.27	-	-	X_{Ilm}	-	-	0.86	0.06	0.12
An	-	-	-	-	-	0.05	0.00	X_{Hm}	-	-	0.14	0.07	0.26
Ab	-	-	-	-	-	0.95	0.02						
Or	-	-	-	-	-	0.00	0.98						

*Total Fe as FeO.
**Recalculated after Carmichael (1967).
b.d., below detection limit; $X_{Fe} = Fe^{2+}/(Fe^{2+} + Mg)$; An = Ca/M, Ab = Na/M, and Or = K/M, where M = Ca + Na + K; X_{Usp} = Si + Ti.

Ca + Mn) = 0.23–0.27; Figures IV-4a and IV-6a). An abrupt increase in the X_{Fe} value (X_{Fe} = 0.54–0.61) accompanying slight Mn decrease (Sps = 0.56–0.57) is conspicuous in the rim. Compositional variations of the xenoblastic Grt II are similar to those of the Grt I, showing low-X_{Fe} inner domain (X_{Fe} = 0.10–0.12) enveloped by even higher-X_{Fe} outer domain (X_{Fe} = 0.58–0.78) in contact with the matrix (Figures IV-4b and IV-6a). Fine-grained Grt III also follows similar trends, except for higher X_{Fe} value (0.27–0.48) of the inner domain compared to that of Grt I and Grt II (Figure IV-6a).

Epidote group minerals

Epidote group minerals are rich in Mn, and ranges from piemontite, allanite to epidote. The compositions of cores are subdivided into two groups; piemontite ($X_{Pmt} = Mn^{3+}/(Fe^{3+} + Mn^{3+} + Al^{VI} - 2)$ = 0.54–0.59; $X_{Ep} = Fe^{3+}/(Fe^{3+} + Mn^{3+} + Al^{VI} - 2)$ = 0.41–0.46) and epidote (X_{Pmt} = 0.23–0.49; X_{Ep} = 0.51–0.72) (Figures IV-5 and IV-6). The core contains 0.03–0.05 a.p.f.u. Sr. Total REE contents are low (REEs = 0.01–0.08 a.p.f.u.). The mantles with increasing REE contents consist of two domains, REE-rich piemontite inner mantle and manganian allanite outer mantle (Figures IV-5 and IV-7). An abrupt light REE increase including Ce is conspicuous in the former (REEs = 0.17–0.20; X_{Pmt} = 0.57–0.62; X_{Ep} = 0.38–0.41). The outer mantles are typified by higher REEs and Fe^{3+} but lower Mn^{3+} (REEs = 0.28–0.35; X_{Pmt} = 0.21–0.40; X_{Ep} = 0.54–0.65) relative to the inner mantles. The rims are near-epidote end member in composition (X_{Ep} = 0.89–0.90).

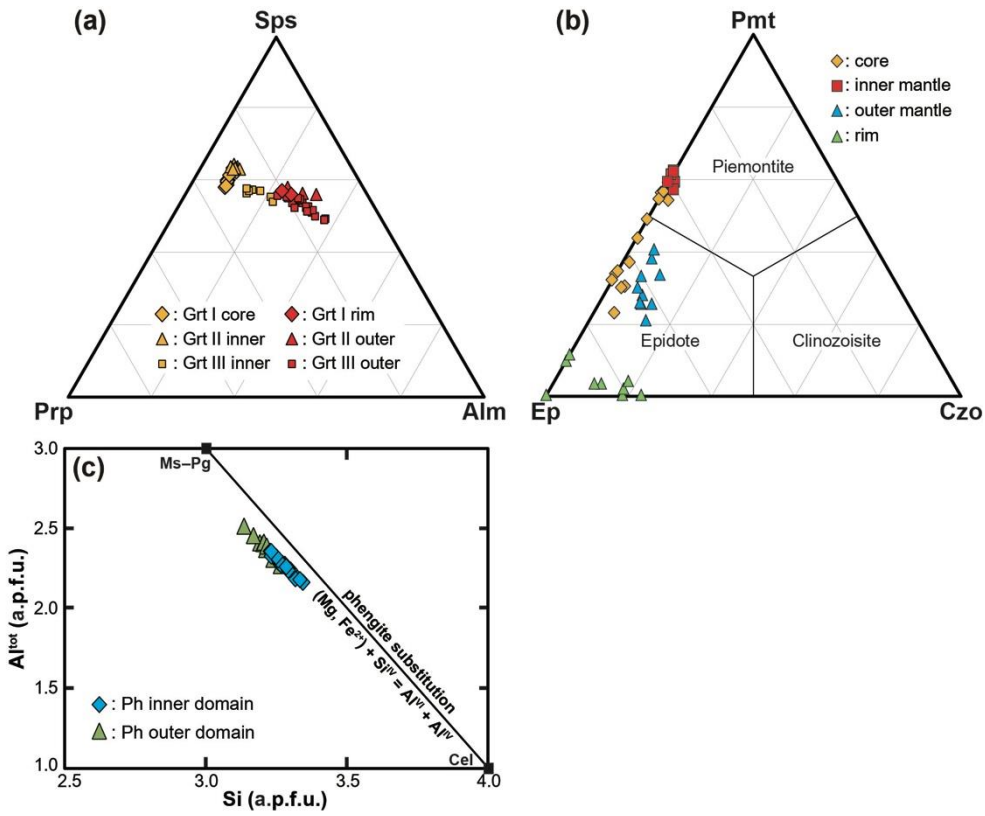

Figure IV-6. Compositional diagrams of (a) garnet, (b) epidote and (c) phengite.

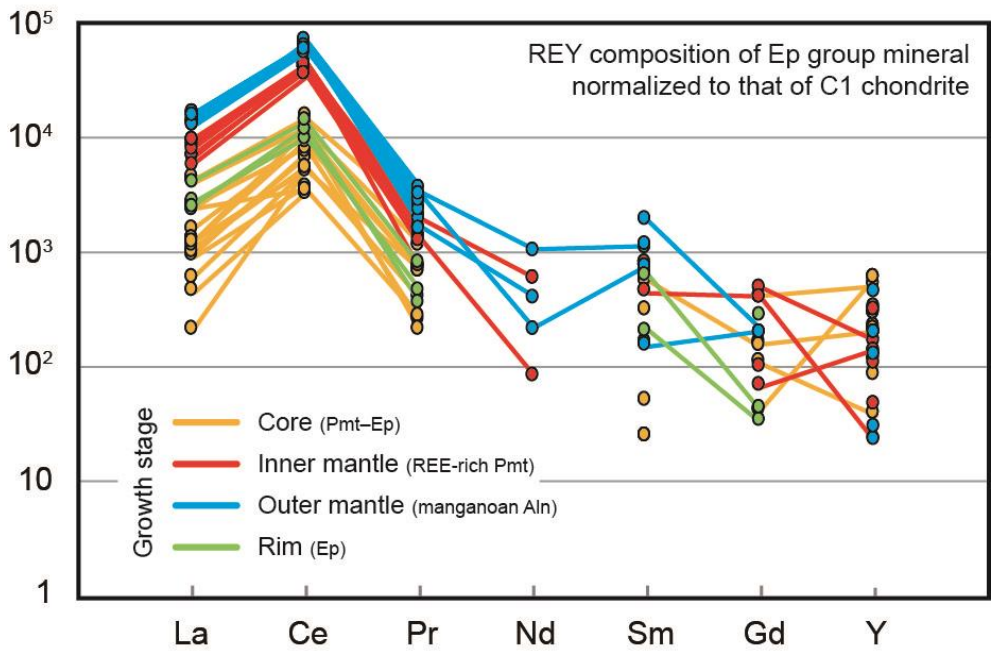

Figure IV-7. C1 chondrite-normalized rare earth elements and yttrium concentrations of epidote group minerals (Sun and McDonough, 1989).

Phengite

Phengite grains are zoned in the celadonite component, decreasing from the inner (Si = 3.23–3.34 a.p.f.u.) to outer segment (Si = 3.14–3.27 a.p.f.u.; Figures IV-5 and IV-6). The Ti contents are also slightly higher in the former (0.05–0.09 a.p.f.u.) than those in the latter (0.03–0.06 a.p.f.u.).

Chlorite

Chlorite is clinochlore in composition. The X_{Fe} values of chlorite core are in the range 0.20–0.24, and increase at the rim (0.27–0.28).

Magnetite, ilmenite and pyrophanite

Magnetite enclosing ilmenite and pyrophanite is the solid-solution of magnetite and ulvöspinel in composition (X_{Usp} = Si + Ti = 0.18–0.22). Ilmenite is rich in hematite component (X_{Ilm} = 0.86; X_{Hm} = 0.13; X_{Pph} = 0.01). The compositions of pyrophanite consists of two groups; Mn-richer (X_{Ilm} = 0.04–0.06; X_{Hm} = 0.07; X_{Pph} = 0.88–0.89) and Mn-poorer (X_{Ilm} = 0.12; X_{Hm} = 0.26; X_{Pph} = 0.62).

Feldspar

The compositions of phengite-replacing feldspars are near-end member albite (An = Ca/(Ca + Na + K) = 0.02–0.05) and K-feldspar (Or = K/(Ca + Na +K) = 0.98–0.99).

METAMORPHIC EVOLUTION AND *P–T* ESTIMATION

Mineral assemblages of the manganiferous quartzite sample are not very informative for reconstructing the *P–T* history using thermobarometers and pseudosection. Therefore, I infer metamorphic facies based on mineral assemblages including Mn-bearing phases. The presence of the piemontite-rich core of epidote group minerals (Figures IV-5 and IV-6b) suggests prograde metamorphism at high f_{O2} conditions. Rare occurrence of tephroite inclusion in the piemontite core, and that of rutile in the garnet core also record evidence for the prograde stage. Piemontite-rich epidote–tephroite–spessartine-rich garnet assemblages indicate greenschist to blueschist facies conditions (e.g. Reinecke, 1986; Martin and Lombardo, 1995; Abs-Wurmbach and Peters, 1999), although common Mn silicate phases in manganiferous quartzose rocks such as braunite and sursassite are absent.

The REE-rich mantles of epidote group mineral represent another prograde stage. The allanite enrichment ($^{A2}REE^{3+} + {}^{M3}(Fe^{2+}, Mg^{2+}) = {}^{A2}Ca^{2+} + {}^{M3}(Mn^{3+}>>Fe^{3+})$ substitution) suggests breakdown of possible REE sources such as monazite and apatite in the matrix. Peak metamorphic stage is represented by the high-X_{Fe} rim of garnet, celadonite-rich inner segment of phengite, outermost rim of epidote and matrix magnetite. The stability of magnetite rather than hematite, the latter of which is common in piemontite-bearing metasediments, as well as abrupt X_{Fe} increase in garnet rim indicates a decrease in f_{O2} during dehydration in the prograde stage.

Chlorite formation at the expense of garnet is retrograde in origin,

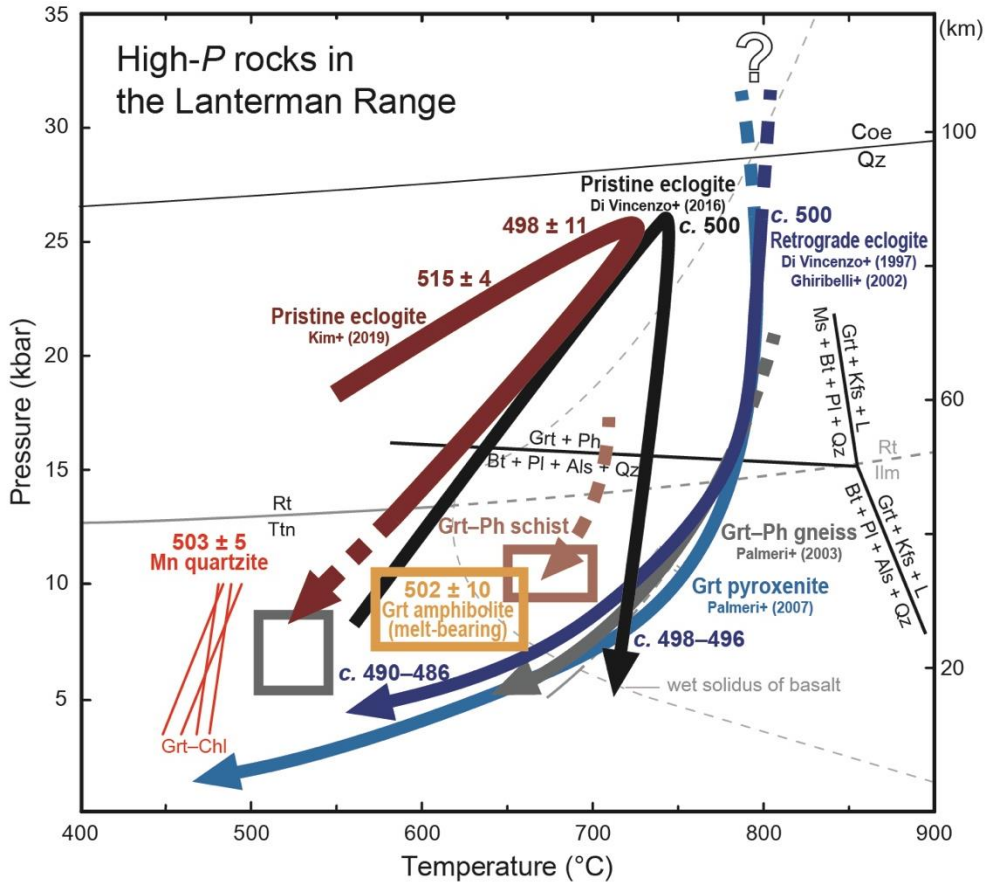

Figure IV-8. *P–T* diagram summarizing the *P–T*(*–t*) paths of various metamorphic rocks in the Lanterman Range; pristine eclogite (Di Vincenzo et al., 2016; Kim et al., 2019), retrograde eclogite (Di Vincenzo et al., 1997; Di Vincenzo and Palmeri, 2001; Ghiribelli et al., 2002), Grt–Ph gneiss (Palmeri et al., 2003), garnet pyroxenite (Palmeri et al., 2007), partially molten amphibolite, Grt–Ph schist and manganiferous quartzite (this study). The weighted mean $^{206}Pb/^{238}U$ ages are given in Ma.

which is coeval with relatively low-celadonite outer segment of phengite. The garnet–phengite thermometer (Krogh and Raheim, 1978; Green and Hellman, 1982) gave meaningless results for the core pair (>2,000 °C), whereas ~530–680 °C for the rim pair at 5 kbar. However, the results are unreliable because of the presence of significant ferri-muscovite component. The garnet–chlorite thermometer (Grambling, 1990; Dickenson and Hewitt, 1986) yielded ~450–480 °C at 5–10 kbar for the rim pairs (Figure IV-8). Near end-member compositions of plagioclase and K-feldspar suggest retrogression finally to low temperature <300 °C (Powell and Powell, 1977; Stormer and Whitney, 1985).

WHOLE-ROCK GEOCHEMISTRY

Whole-rock geochemical data of the manganiferous quartzite sample (151223-1F) were plotted (Figure IV-9) along with those of other piemontite-bearing quartzites from the Otago schist, New Zealand (Coombs et al., 1985), and Sanbagawa belt, Japan (Izadyar et al., 2003). The sample is enriched in MnO (1.78 wt%) and SiO_2 (86.63 wt%), compared to those of the dominant metasedimentary country rocks of siliciclastic compositions. The quartzite sample, together with those from the Otago schist and Sanbagawa belt, is plotted along the lineage from the average composition of chert (Hein and Karl, 1983) to that of pelagic deep clay (Marchig, 1978) in the SiO_2–Al_2O_3–(Fe_2O_3 + FeO) diagram (Figure IV-9), more akin to the chert. The Al_2O_3–MnO–(Fe_2O_3 + FeO) diagram shows higher Mn

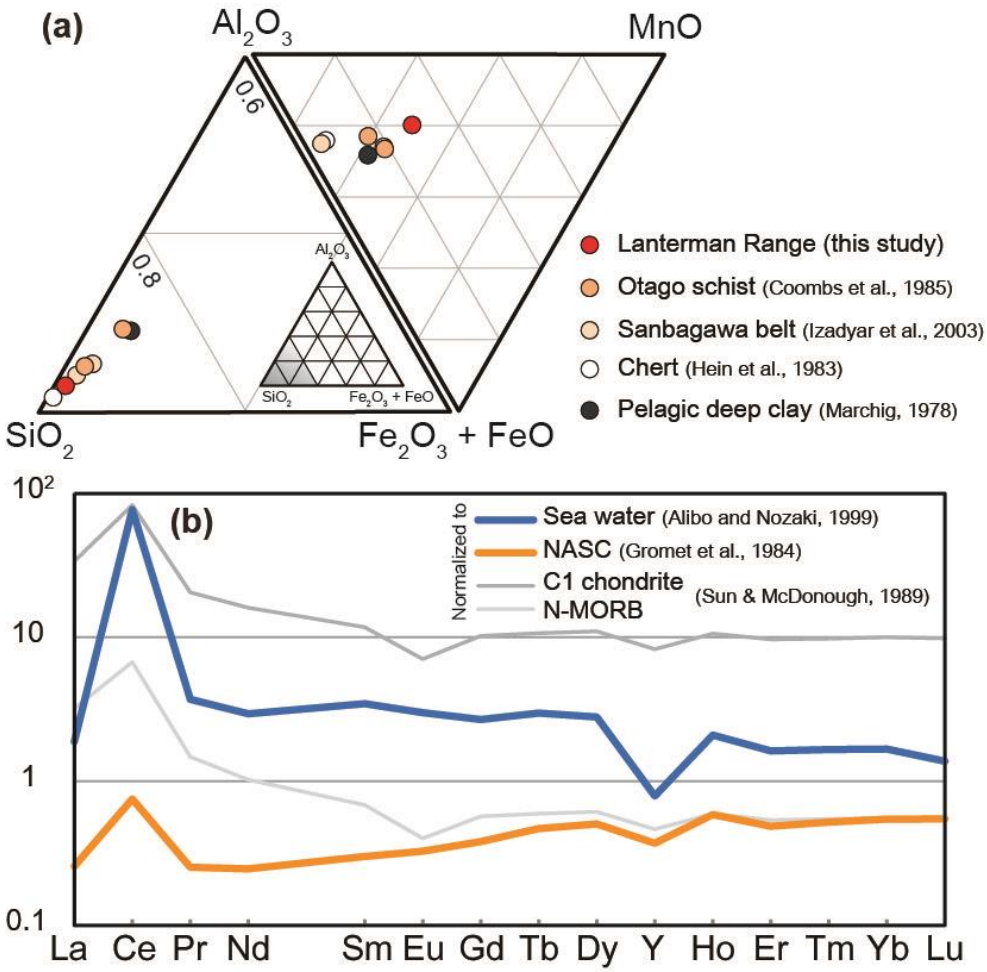

Figure IV-9. Whole-rock geochemical data of manganiferous quartzite from this study, New Zealand and Japan. (a) SiO_2–Al_2O_3–(Fe_2O_3 + FeO) and Al_2O_3–MnO–(Fe_2O_3 + FeO) ternary diagrams. Average compositions of chert and pelagic deep clay are also plotted. (b) REE patterns normalized to various reservoirs. NASC—North America shale composite; N-MORB—normal mid-ocean ridge basalt.

enrichment in the sample than those of the Otago schist and Sanbagawa belt. The REE and Y compositions normalized to those of various reservoirs such as sea water (Alibo and Nozaki, 1999), North America shale composite (Gromet et al., 1984), C1 chondrite and normal mid-ocean ridge basalt (Sun and McDonough, 1989) are characterized by strong positive anomaly of Ce (Figure IV-9).

ZIRCON GEOCHRONOLOGY

The manganiferous quartzite sample (151223-1F) only yielded fine-grained (<100 μm) subhedral to anhedral zircon (Figure IV-10). Core-rim zonation is common. Only one zircon grain shows oscillatory zoned core, surrounded by dark-CL rim (Figure IV-10). The U-Th-Pb isotopic compositions of 12 spots measured on 12 zircon crystals are shown in the Tera-Wasserburg concordia diagram (Figure IV-10; Table IV-2). The proportion of common ^{206}Pb is low (<0.7%). The spot dates of the zoned zircon yielded Paleoproterozoic apparent ages (2160 ± 14 Ma and 1880 ± 10 Ma, 1σ) for the core and rim. The U-Pb isotopic compositions of the remaining 10 analyses yielded mostly Cambrian ages, except for one Ediacaran age (spot 5.1; 565 ± 5 Ma, 1σ). Among the Cambrian spot dates, the spot 11.1 is low in concordance (6%) and the spot 2.1 is high in Th/U ratio (0.42). Seven Cambrian spot dates with low Th/U ratio (0.01–0.05) are in the range 516 ± 9 Ma (1σ) to 492 ± 8 Ma (1σ), resulting in the weighted mean $^{206}Pb/^{238}U$ age of 503 ± 5 Ma (2σ; MSWD = 1.03).

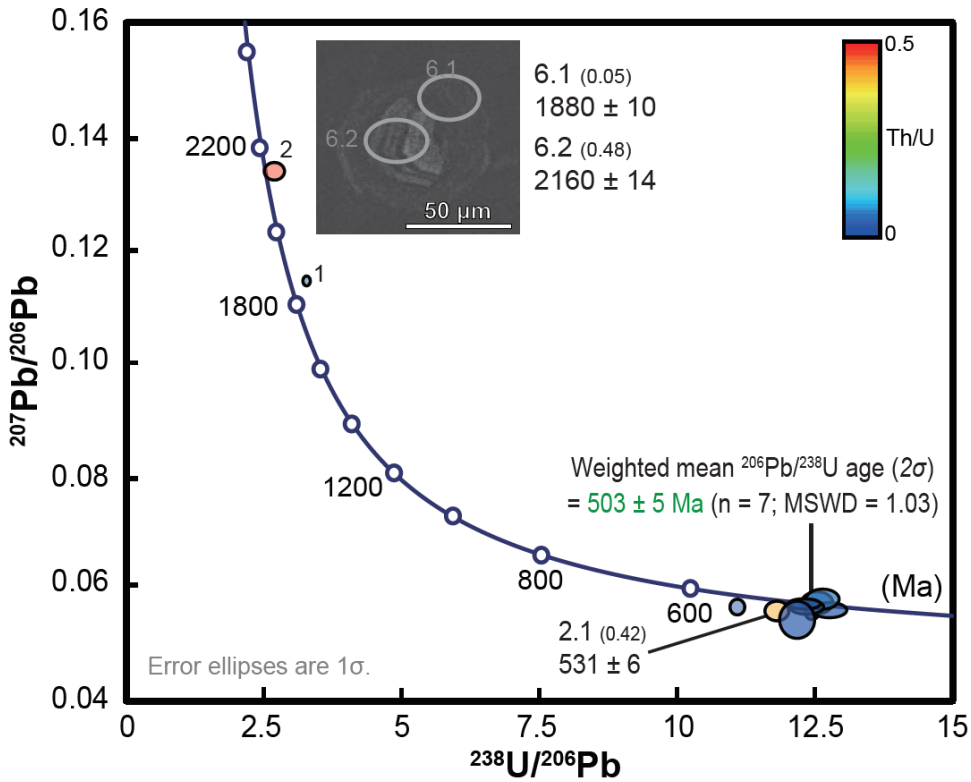

Figure IV-10. Tera-Wasserburg concordia diagram for the U-Pb spot analyses of zircon from the mangniferous quartzite sample (151223-1F). Inset diagram shows the CL image and analyzed spots of Paleoproterozoic grain 6.1.

Table IV-2. The SHRIMP U-Th-Pb isotopic compositions of zircon from the manganiferous quartzitic schist

Spot no.	Texture	U (ppm)	Th (ppm)	Th/U	Common ^{206}Pb (%)	$^{207}Pb^*/^{206}Pb^*$	$^{208}Pb^*/^{206}Pb^*$	$^{206}Pb^*/^{238}U$	$^{208}Pb^*/^{232}Th$	$^{207}Pb/^{206}Pb$ age (Ma)	$^{206}Pb/^{238}U$ age (Ma)	$^{208}Pb/^{232}Th$ age (Ma)	Concordance (%)
Sample 151223-1F													
1.1	dC	617	14	0.02	0.24	0.05707 ± 566	0.0082 ± 261	0.08363 ± 41	0.030 ± 830	520 ± 37	500 ± 8	604 ± 163	100
2.1	dC	558	243	0.45	0.66	0.05560 ± 305	0.0074 ± 307	0.08599 ± 49	0.001 ± 66	508 ± 54	531 ± 6	22 ± 13	96
3.1	dC	6	3	0.54	3.65	0.14534 ± 9372	0.1885 ± 4944	0.10097 ± 69	0.082 ± 5852	2292 ± 1109	549 ± 36	1585 ± 1094	174
4.1	dC	730	7	0.01	0.10	0.05552 ± 156	0.0038 ± 276	0.08387 ± 46	0.018 ± 1721	493 ± 33	503 ± 4	365 ± 342	97
5.1	dCr	889	7	0.01	-0.12	0.05622 ± 209	0.0066 ± 272	0.09331 ± 47	0.061 ± 3188	556 ± 43	565 ± 5	1196 ± 607	96
6.1	ozc	561	26	0.05	0.04	0.11500 ± 138	-0.0126 ± 500	0.31100 ± 175	0.092 ± 464	1899 ± 10	1705 ± 14	1779 ± 86	105
6.2	dCc	326	155	0.49	0.08	0.13471 ± 102	0.1343 ± 622	0.38293 ± 233	0.117 ± 322	2160 ± 13	2021 ± 73	2231 ± 58	103
8.1	dCr	220	7	0.03	0.20	0.05394 ± 194	0.0086 ± 354	0.08740 ± 48	0.016 ± 2243	498 ± 121	516 ± 9	327 ± 446	95
9.1	dCr	374	7	0.02	0.05	0.05573 ± 91	0.0049 ± 290	0.07923 ± 44	0.019 ± 584	442 ± 36	492 ± 8	375 ± 116	88
9.2	dC	573	28	0.05	0.41	0.05774 ± 120	0.0045 ± 390	0.07984 ± 43	0.007 ± 463	520 ± 45	495 ± 8	142 ± 93	105
10.1	bC	648	5	0.01	-0.03	0.05686 ± 61	0.0032 ± 273	0.08225 ± 44	0.036 ± 1483	486 ± 24	510 ± 8	709 ± 289	95
11.1	dCc	65	7	0.11	0.23	0.05161 ± 472	0.0328 ± 543	0.08303 ± 65	0.025 ± 324	268 ± 210	514 ± 12	500 ± 64	6
12.1	dC	401	5	0.01	-0.05	0.05629 ± 86	0.0062 ± 292	0.08198 ± 46	0.041 ± 1023	464 ± 34	508 ± 9	805 ± 199	90

*dC, dark CL; bC, bright CL; c, core; r, rim; oz, oscillatory zoned.
Errors are 1σ estimates. All the isotopic compositions were calculated using the ^{207}common Pb correction method except for $^{207}Pb^*/^{206}Pb^*$ ratios corrected by ^{204}Pb. Pb^* denotes radiogenic Pb. Concordance was calculated from $^{207}Pb/^{235}U$ and $^{206}Pb/^{238}U$ ages.

DISCUSSION

Protolith origin of the manganiferous quartzite

Whole-rock geochemistry of the manganiferous quartzite showed affinity to the deep sea chert (Hein and Karl, 1983) and, to a lesser degree, pelagic deep clay (Marchig, 1978; Figure IV-9). The quartzite sample is SiO_2-rich, but highly enriched in Mn compared to ordinary quartzose metasediments. Other hydrothermally mobile elements such as Fe could have been incorporated as well (Edmond et al., 1982). On the similar geochemical constraints, Reinecke et al. (1985) proposed pelagic siliceous mudstones containing Fe-Mn-oxyhydroxide nodules as source rocks, which is in line with the present-day metalliferous sediments overlying oceanic basaltic crust (Martin and Kienast, 1987).

Strong positive anomaly of Ce invokes the presence of deep sea ferromanganese deposits. Hydrogenetic precipitation from sea water is preferred, because diagenetic nodules or crusts from sediment pore fluids are characterized by a negative Ce anomaly (Hein and Koschinsky, 2014). Both precipitation processes took place at highly-oxidized conditions, which were established by bottom currents (e.g. Lusty and Murton, 2018). The pelagic protoliths should contain ferromanganese crusts and/or nodules; the former are prefereed because the latter are much richer in Mn than Fe (Hein, 2016). Tectonic setting for the sedimentation of the quartzitic protolith should be shallower than abyssal plain, and most likely continental shelf to slope (cf. Herbosch et al., 2016), because of the terrigenous contribution is

represented by detrital zircon grains. The continental input in the silica-rich deep sea sediments is in marked contrast to the biogenic origin of the manganiferous silica-rich rock (e.g. Mottana, 1986). Taken together, the manganiferous quartzitic schist originated from the dominantly silica-rich chemical precipitates, together with subordinate inputs of aluminum from terrigenous clay and manganese from ferromanganese deposits (e.g. Coombs et al., 1985).

Metamorphic and tectonic implications for subduction-zone processes

Spessartine is commonly stable over a wide range of f_{O2} and *P–T* conditions up to those of amphibolite-granulite facies (Abs-Wurmbach and Peters, 1999), and those coexisting with piemontite are more enriched in spessartine (Keskinen and Liou, 1987). With decreasing f_{O2} during prograde metamorphism, piemontite loses Mn and epidote is stable with increasing temperature (Figure IV-5; Keskinen and Liou, 1987). Pre-existing Mn-oxide buffer is necessary for the preservation of piemontite, thereby remaining in highly oxidized conditions during metamorphism (Reinecke, 1986). However, the presence of magnetite rather than hematite in the manganiferous quartzite is apparently indicative of the relatively reducing environments because of dehydration. Other possibilities such as low fluid/rock ratio during the metamorphism have been commonly inferred as well (Reinecke, 1986; Keskinen and Liou, 1987).

The turbiditic intercalation of decimeter-thick layers of the relatively highly-oxidized manganiferous quartzite within the quartzofeldspathic schists (e.g. Palmeri et al., 2003, 2011) has strong implications for the high-*P* metamorphism. Large variation in f_{O2} among the turbiditic sediments suggests that oxygen mobility not necessarily depends on that of dominantly hydrous fluids. The strong gradient of f_{O2} and resulting mineral assemblages indicates local f_{O2} buffering during high-*P* metamorphism (Reinecke, 1986).

The maximum deposition age (*c.* 530 Ma) constrained from the youngest detrital zircon of the manganiferous quartzite is comparable to late Neoproterozoic–early Cambrian upper limits of the siliciclastic sedimentation in the Wilson Terrane (Estrada et al., 2016; Paulsen et al., 2016; Kim et al., 2017). The depositional setting is possibly of passive margin environment, which preceded and/or was broadly coeval with the Ross tectonism (e.g. Rocchi et al., 2011). It is compatible with the protolith formation of the quartzite in deep ocean basin not far from continent. The weighted mean $^{206}Pb/^{238}U$ age of low Th/U zircon grains of the manganiferous quartzite is 503 ± 5 Ma (2σ; Figure IV-10), which corresponds to time of the high-*P* metamorphism in the context of the Ross orogeny (e.g. Kim et al., 2019).

CONCLUSIONS

The manganiferous quartzitic schist was investigated using mineral chemistry, whole-rock geochemistry and zircon geochronology, in order to

constrain process and tectonic setting of the protolith formation. Positive Ce anomaly together with geochemical affinity to deep sea sediments confirmed the dominantly quartzose pelagic sediment containing ferromanganese crusts and/or nodules, most likely at continental shelf or slope. Mineral assemblages represented by spessartine-rich garnet, piemontite-allanite-epidote, high-celadonite phengite and magnetite indicated greenschist to blueschist facies metamorphism. The relict piemontite core survived prograde metamorphism accompanied by dehydration. Close spatial relationship of the quartzite with the dominant siliciclastic (meta)sedimentary rocks suggest their common formation as turbiditic packages not earlier than early Cambrian. The Ross orogeny and subduction resulted in the inversion of passive margin and high-*P* metamorphism of the whole garnet–phengite-bearing metasediments.

REFERENCES

Abraham, K., & Schreyer, W. (1976). A talc-phengite assemblage in piemontite schist from Brezovica, Serbia, Yugoslavia. *Journal of Petrology*, 17, 421–439.

Abs-Wurmbach, I. & Peters, T. (1999). The Mn–Al–Si–O system: an experimental study of phase relations applied to parageneses in manganese-rich ores and rocks. *European Journal of Mineralogy*, 11, 45–68.

Alibo, D., & Nozaki, Y. (1999). Rare earth elements in seawater: Particle association, shale-normalization, and Ce oxidation. *Geochimica et Cosmochimica Acta*, 63, 363–372.

Boger, S.D. (2011). Antarctica – Before and after Gondwana. *Gondwana Research*, 19, 335–371.

Bomparola, R.M., Ghezzo, C., Belousova, E., Griffin, W.L., & O'Reilly, S.Y. (2007). Resetting of the U–Pb zircon system in Cambro-Ordovician intrusives of the Deep Freeze Range, Northern Victoria Land, Antarctica. *Journal of Petrology*, 48, 327–364.

Borg, S.G., & Stump, E. (1987). Paleozoic magmatism and associated tectonic problems of northern Victoria Land, Antarctica. In G.D. McKenzie (Ed.), *Gondwana six: Structure, tectonics and geophysics.* American Geophysical Union (AGU) Geophysical Monograph Series (vol. 40, pp. 67–75). Washington, DC: AGU.

Capponi, G., Castelli, D., Fioretti, A.M., & Oggiano, G. (1997). Geological mapping and field relationships of eclogites from the Lanterman Range (Northern Victoria Land, Antarctica). In C.A. Ricci (Ed.), *The Antarctic region: Geological evolution and processes* (pp. 219–225). Siena: Terra Antartica Publication.

Cawood, P.A. (2005). Terra Australis Orogen: Rodinia breakup and development of the Pacific and Iapetus margins of Gondwana during the Neoproterozoic and Paleozoic. *Earth-Science Reviews*, 69, 249–279.

Claoué-Long, J.C., Compston, W., Roberts, J., & Fanning, C.M. (1995). Two Carboniferous ages: A comparison of SHRIMP zircon dating with conventional zircon ages and $^{40}Ar/^{39}Ar$ analysis. In W.A. Berggren, D.V. Kent, M.-P. Aubry, & J. Hardenbol (Eds.), *Geochronology, time scales and global stratigraphic correlation*, Society for Sedimentary Geology (SEPM) Special Publication (vol. 54(4), pp. 3–21). Tulsa, OK.: SEPM.

Cheong, W., Cho, M., & Kim, Y. (2013). An efficient method for zircon separation using the gold pan. *Journal of the Petrological Society of Korea*, 22, 63–70 (in Korean with English abstract).

Coombs, D.S., Dowse, M., Grapes, R., Kawachi, Y., & Roser, B. (1985). Geochemistry and origin of piemontite-bearing and associated manganiferous schists from Arrow Junction, western Otago, New Zealand. *Chemical Geology*, 48, 57–78.

Cumming, G.L., & Richards, J.R. (1975). Ore lead isotope ratios in a continuously changing earth. *Earth and Planetary Science Letters*, 28, 155–171.

Dallmeyer, R.D., & Wright, T.O. (1992). Diachronous cleavage development in the Robertson Bay terrane, Northern Victoria Land, Antarctica: Tectonic implications. *Tectonics*, 11, 437–448.

Dickenson, M.P. III, & Hewitt, D.A. (1986). A garnet-chlorite geothermometer (abstract). Geological Society of America Abstracts Program t8:584.

Di Vincenzo, G., Ghiribelli, B., Giorgetti, G., & Palmeri, R. (2001). Evidence of a close link between petrology and isotope records: constraints from SEM, EMP, TEM and in situ ^{40}Ar–^{39}Ar laser analyses on multiple generations of white micas (Lanterman Range, Antarctica). *Earth and Planetary Science Letters*, 192, 398–405.

Di Vincenzo, G., Horton, F., & Palmeri, R. (2016). Protracted (~30 Ma) eclogite-facies metamorphism in northern Victoria Land (Antarctica): Implications for the geodynamics of the Ross/Delamerian Orogen. *Gondwana Research*, 40, 91–106.

Di Vincenzo, G., & Palmeri, R. (2001). An ^{40}Ar–^{39}Ar investigation of high-pressure metamorphism and the retrogressive history of mafic eclogites from the Lanterman Range (Antarctica): evidence against a simple temperature control on argon transport in amphibole. *Contributions to Mineralogy and Petrology*, 141, 15–35.

Di Vincenzo, G., Palmeri, R., Talarico, F., Andriessen, P.A., & Ricci, C.A. (1997). Petrology and geochronology of eclogites from the Lanterman Range, Antarctica. *Journal of Petrology*, 38, 1391–1417.

Edmond, J.M., Vondamm, K.L., McDuff, R.E., & Measures, C.I. (1982). Chemistry of hot springs on the east Pacific Rise and their effluent dispersal. *Nature*, 297, 187–191.

Estrada, S., Läufer, A., Eckelmann, K., Hofmann, M., Gärtner, A., & Linnemann, U. (2016). Continuous Neoproterozoic to Ordovician sedimentation at the East Gondwana margin – Implications from detrital zircons of the Ross Orogen in northern Victoria Land, Antarctica. *Gondwana Research*, 37, 426–448.

GANOVEX Team. (1987). German Antarctic North Victoria Land Expedition 1982/83: GANOVEX III (vol. 2). In F. Tessensohn & N.W.

Roland (Eds.), Geologisches Jahrbuch (vol. B66, pp. 324). Hannover: Bundesanstalt für Geowissenschaften und Rohstoffe.

Goemare, E., Demarque, S., Dreesen, R., & Declercq, P.Y. (2016). The geological and cultural heritage of the Caledonian Stavelot-Venn Massif, Belgium. *Geoheritage*, 8, 211–233.

Grambling, J.A. (1990). Internally-consistent geothermometry and H_2O barometry in metamorphic rocks: the example garnet-chlorite-quartz. *Contributions to Mineralogy and Petrology*, 105, 617-628.

Gromet, L.P., Dymek, R.F., Haskin, L.A., & Korotev, R.L. (1984). The "North American shale composite": its compilation, major and trace element characteristics. *Geochimica Cosmochimica Acta*, 48, 2469–2482.

Hein, J.R. (2016). Manganese nodules. In J. Harff et al. (eds.), *Encyclopedia of Marine Geosciences*: Springer.

Hein, J.R., & Karl, S.M. (1983). Comparisons between open-ocean and continental margin chert sequences. In: Iijima, A., Hein, J.R., & Siever, R. (Eds.), *Siliceous Deposits in the Pacific Region*, Elsevier, Amsterdam, pp. 25–44.

Hein, J.R., & Koschinsky, A. (2014). Deep-ocean ferromanganese crusts and nodules. *In* K. Turekian, & H. Holland, (eds.), *Treatise on Geochemistry*: Elsevier.

Herbosch, A., Liegeois, J.-P., & Pin, C. (2016). Coticules of the Belgian type area (Stavelot-Venn Massif): Limy turbidites within the nascent Rheic oceanic basin. *Earth-Sciences Reviews*, 159, 186–214.

Huebner, J.S., Flohr, M.J.K., & Grossman, J.N. (1992). Chemical fluxes and origin of a manganese carbonate-oxide-silicate deposit in bedded chert. *Chemical Geology*, 100, 93–118.

Izadyar, J., Tomita, K., & Shinjoe, H. (2003). Geochemistry and origin of piemontite-quartz schists in the Sanbagawa Metamorphic Belt, central Shikoku, Japan. *Journal of Asian Earth Science*, 21, 711–730.

Jöns, N., & Schenk, V. (2004). Petrology of whiteschists and associated rocks at Mautia Hill (Tanzania): Fluid infiltration during high-grade metamorphism?. *Journal of Petrology*, 45, 1959–1981.

Kim, T., Kim, Y., Cho, M., & Lee, J.I. (2019). *P–T* evolution and episodic zircon growth in barroisite eclogites of the Lanterman Range, northern Victoria Land, Antarctica. *Journal of Metamorphic Geology*, 37, 509–537.

Kim, Y., Yi, K., & Cho, M. (2009). Parageneses and Th-U distributions among allanite, monazite, and xenotime in Barroviantype metapelites, Imjingang belt, central Korea. *American Mineralogist*, 94, 430–438.

Kleinschmidt, G., & Tessensohn, F. (1987). Early Paleozoic westward directed subduction at the Pacific margin of Antarctica. In G.D. McKenzie (Ed.), Gondwana six: Structure, tectonics and geophysics. American Geophysical Union (AGU) Geophysical Monograph Series (vol. 40, pp. 89–105). Washington, DC: AGU.

Ludwig, K.R. (2008). User's manual for Isoplot 3.6: A geochronologicalvtoolkit for Microsoft Excel. Berkeley Geochronology Center Special Publication (no. 4). Berkeley, CA: Berkeley Geochronology Center, 77 pp.

Lusty, P.A.J., & Murton, B.J. (2018). Deep-ocean mineral deposits: metal resources and windows into earth processes. *Elements*, 14, 301–306.

Marchig, V. (1978). Brown clays from the central Pacific—metalliferous sediments or not? *Geologische Jahrboek*, D30, 3–25.

Martin, S. & Lombardo, B. (1995). Sursassite, spessartine, piemontite in Fe-Mn metacherts from Lago Bleu, upper Val Varaita (western Alps), *in* B. Lombardo (ed.), *Studies on metamorphic rocks and minerals of the western Alps*. A Volume in Memory of Ugo Pognante. Boll. Museo Regionale Scienze Naturali. Torino, 13/2, 103-130.

Massone, H.J., & Schreyer, W. (1989). Stability field of the high-pressure assemblages talc-phengite and two new phengite barometers. *European Journal of Mineralogy*, 1, 391–410.

Mottana, A. (1986). Blueschist-facies metamorphism of manganiferous cherts: a review of the Alpine occurrences. *Geological Society of America, Memoir*, 164, 267–299.

Paces, J.B., & Miller, J.D. (1993). Precise U-Pb ages of Duluth Complex and related mafic intrusions, northeastern Minnesota: Geochronological insights to physical, petrogenetic, paleomagnetic, and tectonomagmatic

processes associated with the 1.1 Ga Midcontinent Rift system. *Journal of Geophysical Research,* 98, 13997–14013.

Palmeri, R., Ghiribelli, B., Ranalli, G., Talarico, F., & Ricci, C.A. (2007). Ultrahigh-pressure metamorphism and exhumation of garnet-bearing ultramafic rocks from the Lanterman Range (northern Victoria Land, Antarctica). *Journal of Metamorphic Geology*, 25, 225–243.

Palmeri, R., Ghiribelli, B., Talarico, F., & Ricci, C.A. (2003). Ultra-high pressure metamorphism in felsic rocks: the garnet-phengite gneisses and quartzites from the Lanterman Range, Antarctica. *European Journal of Mineralogy*, 15, 513–525.

Palmeri, R., Talarico, F.M., & Ricci, C.A. (2011). Ultrahigh-pressure metamorphism at the Lanterman Range (northern Victoria Land, Antarctica). *Geological Journal*, 46, 126–136.

Paulsen, T.S., Deering, C., Sliwinski, J., Bachmann, O., & Guillong, M. (2016). Detrital zircon ages from the Ross Supergroup, north Victoria Land, Antarctica: Implications for the tectonostratigraphic evolution of the Pacific-Gondwana margin. *Gondwana Research*, 35, 79–96.

Powell, M., & Powell, R. (1977). A nepheline-alkali feldspar geothermometer. *Contributions to Mineralogy and Petrology*, 62, 193–204.

Reinecke, T. (1986). Phase relationships of sursassite and other Mn-silicates in highly oxidized low-grade, high-pressure metamorphic rocks from Evvia and Andros Islands, Greece. *Contributions to Mineralogy and Petrology*, 94, 110–126.

Reinecke, T. (1991). Very-high-pressure metamorphism and uplift of coesite-bearing metasediments from the Zermatt-Saas zone, Western Alps. *European Journal of Mineralogy,* 3, 7–17.

Reinecke, T. (1998). Prograde high- to ultrahigh-pressure metamorphism and exhumation of oceanic sediments at Lago di Cignana, Zermatt-Saas Zone, western Alps. *Lithos*, 42, 147–189.

Reinecke, T., Okruch, M., & Richter, P. (1985). Geochemistry of ferromanganoan metasediments from the Island of Andros, Cycladic blueschist belt, Greece. *Chemical Geology,* 53, 249–278.

Ricci, C.A., Talarico, F., Palmeri, R., Di Vincenzo, G., & Pertusati, P.C. (1996). Eclogite at the Antarctic palaeo-Pacific active margin of Gondwana (Lanterman Range, northern Victoria Land, Antarctica). *Antarctic Science*, 8, 277–280.

Schreyer, W. (1985). Metamorphism of crustal rocks at mantle depth: High-pressure minerals and mineral assemblages in metapelites. *Fortschritte der Mineralogie*, 63, 227–261.

Stormer, C.S.Jr., & Whitney, J.A. (1985). Two feldspar and iron-titanium oxide equilibria in silicic magmas and the depth of origin of large volume ash-flow tuffs. *American Mineralogist*, 70, 52–64.

Sun, S.s., & McDonough, W.F. (1989). Chemical and isotopic systematics of oceanic basalts: implications for mantle composition and processes, in Saunders, A.D., and Norry, M.J., eds., *Magmatism in the ocean basins*: London, Geological Society [London] Special Publication, 42, p. 313–345.

Thomson, J.A. (2001). Relationships of coticule geochemistry to stratigraphy in the Perry Mountain and Megunticook formations, New England Appalachians. *Canadian Mineralogist*, 39, 1021–1037.

Weaver, S.D., Bradshaw, J.D., & Laird, M.G. (1984). Geochemistry of Cambrian volcanics of the Bowers Supergroup and implications for the Early Palaeozoic tectonic evolution of northern Victoria Land, Antarctica. *Earth and Planetary Science Letters*, 68, 128–140.

Whitney, D.L., & Evans, B.W. (2010). Abbreviations for names of rock-forming minerals. *American Mineralogist*, 95, 185–187.

Williams, I.S. (1998). U-Th-Pb geochronology by ion microprobe. In M.A. McKibben, W.C. Shanks III, & W.I. Ridley (Eds.), *Applications of microanalytical techniques to understanding mineralizing processes,* Reviews in Economic Geology (v. 7, pp. 1–35). Littleton, CO: Society of Economic Geologists.

CHAPTER V

Conclusions and future work

CONCLUSIONS

Among the Lanterman Range eclogites, pristine barroisite eclogites with no ultrahigh-*P* precursor were investigated in order to determine a quantitative *P*–*T* path and age of mafic protoliths. The prograde *P*–*T* evolution consisting of three metamorphic stages (M_1–M_3) attests to low thermal gradient (~5–10 ℃/km), thus cold subduction regime. The prograde segments, $M_{1–2}$ and M_3, representing two distinctive stages of burial are linked to two-stage episodic growth of high-*P* zircon at *c.* 515 Ma and *c.* 500 Ma, respectively. The latter could mark the accretion time of the Bowers Terrane onto the Wilson Terrane. An interim exhumation stage was present during the prolonged subduction. Taken together, I suggest two cycles of subduction and exhumation during the Cambrian.

The pristine eclogites preserve igneous zircon cores of Ediacaran ages (591 ± 8 Ma and 603 ± 4 Ma, *t*σ). The discovery of Ediacaran rift-related mafic magmatism in northern Victoria Land, or the Transantarctic Mountains, is comparable to *c.* 600–580 Ma rift-related volcanics in the Tasmanides. I propose that the Ross onset at early Cambrian times was preceded by the Ediacaran rift to passive margin stage, which was distinct from Cryogenian rifting followed by Ediacaran arc initiation of previous research. The Ediacaran magmatic rocks, together with other felsic to intermediate components, are a strong candidate for the source of the Pacific-Gondwana zircon group (*c.* 700–500 Ma). This zircon population is widespread in the late Neoproterozoic to Triassic sediments along the

Gondwana margin including the Transantarctic Mountains and Tasmanides, and the Ediacaran age peak is distinct in these ‘mud-pile’.

Peculiar lithology, manganiferous quartzitic schist, was collected along with the garnet–phengite quartzofeldspathic schists and gneisses. The quartzite preserves Mn-silicate and oxide minerals such as piemontite-rich epidote, attesting oxidized nature of the sedimentary protolith. Pelagic chert-like protolith is most likely, containing hydrogenetic ferromanganese deposits in the deep sea environments. Tectonic evolution from early Cambrian deposition to middle Cambrian metamorphism (503 ± 5 Ma, 2σ) is broadly coeval with that of the country gneisses enclosing the eclogite boudins.

FUTURE WORK

In this thesis, I solved many petrologic and geochronologic aspects of high-*P* metamorphic rocks in the Lanterman Range, northern Victoria Land, Antarctica. There are still far more way to go, i.e. more in-depth researches are required in line with new topics. Here I briefly list up the unsolved problems and intriguing points of the high-*P* metamorphic rocks in the Lanterman Range, as well as on-going projects.

(1) Time line spanning from protolith formation of eclogite through cyclic subduction-exhumation, to final exposure to crustal depths. In chapter II, I delineated *c.* 15 Ma duration of two cycles of burial and exhumation. However, timing of the interim

exhumation could not be determined. Combined with geochronology, REE geochemistry and thermometry (e.g. Ti-in-zircon) of zircon from retrograde eclogite, a time frame of eclogite evolution could be discovered.

(2) Tectonic correlation of the Lanterman Range eclogites to the high-*P* metamorphic rocks in the Tasmanides. Eclogites and blueschists of Cambrian to Ordovician ages have been reported in the Tasmanides of eastern Australia. Spatial distribution and *P*–*T*–*t* evolution of these possibly coeval high-*P* rocks should tell orogen-scale tectonic architecture and thermal structure.

(3) Geochronologic constraint on the formation and accretion of the Bowers terrane. The formation of the Lanterman Range eclogites are closely correlated to the terrane accretion, but the timing of the Bowers terrane formation is still unclear. The lowermost unit, i.e. Glasgow volcanics, contains volcanic clasts of dominantly mafic composition. Time constraint on the formation of this possible oceanic arc basement would give important implications for the regional tectonics. Other mafic bodies along the terrane boundary such as the Tiger gabbro and Niagara Ice Fall mafic suites are potential targets as well.

(4) Detrital zircon geochronology of the country rocks enclosing mafic boudins. The host rocks are mostly garnet–phengite

quartzofeldspathic schists and gneisses, and their sedimentary protoliths are commonly linked to passive margin to active margin sediments of the Wilson Terrane. Timing of deposition and pre-subduction architecture would delineate changing provenances associated with tectonic inversion.

(5) The manganiferous quartzite investigated in the chapter IV consists of many uncommon Mn-bearing minerals. More in-detail documentation of minerals is necessary in order to understand the mineral parageneses. Pseudosection analyses and accessory mineral dating are another crucial projects.

(6) The manganiferous quartzite protolith needs further consideration on its formation process, in particular timing. The youngest detrital zircon (*c.* 530 Ma) attests its deposition in possibly early Cambrian. The juxtaposition process of continental and oceanic materials and its timing are to be investigated.

(7) Compilation of *P*–*T*–*t* paths of the high-*P* metamorphic rocks in the Lanterman Range. Each high-*P* block could experience distinct evolutionary path, thus quantitative determination and comparison of their *P*–*T*–*t* paths should give implications for tectonic processes in the high-*P* metamorphic terrane.

요약(국문초록)

남극 북빅토리아랜드 랜터만 산맥의 고압 에클로자이트와 주변 변성퇴적암류의 변성지구조 진화

서울대학교 대학원 지구환경과학부
김태환

안데스형 로스 조산운동의 맥락에서 고압 터레인의 변성지구조 진화를 밝히기 위해 본 연구에서는 랜터만 산맥 에클로자이트와 주변 변성퇴적암류를 연구하였다. 신선한 에클로자이트 시료들은 주로 석류석+옴파사이트+칼슘/소듐-칼슘 각섬석+녹렴석+펜자이트+금홍석+석영으로 구성되며, 이로부터 두 개의 구별되는 압력-온도 경로, M_{1-2}와 M_3를 정의하는 세 단계의 전진변성작용을 밝혀냈다. 슈도섹션 모델링, 포획광물 공생관계, 지온지압계 등으로부터 에클로자이트가 ~15-20kbar와 520-570℃(M_1)에서 ~22-25kbar와 630-650℃(M_2), ~26±3kbar와 720±80℃(M_3)까지 진화했음을 알아냈다. 저어콘의 외연부와 최외부 띠에 대한 슈림프 우라늄-납 연령측정을 통해 각각 515±4Ma($t\sigma$; M_2)와 498±11Ma($t\sigma$; M_3), 두 차례에 걸친 단편적 에클로자이트 저어콘 성장사를 구별해냈다. 이로부터 계산한 평균매몰속도는 차가운 섭입을 고려하면 너무 낮아(<2mm/year), 두 단계의 전진변성 압력-온도 경로 사이에 융기단계가 있었어야 한다. 따라서, 로스 조산운동 동안 두 차례의 불연속적인 매몰-융기 사건이 약 15Ma를 두고 일어났음을 알 수 있다.

저어콘 상속핵 연령들(590.8±8.3Ma와 603.2±4.4Ma, $t\sigma$)과 약알칼리, 판내부 내지 대륙현무암에 가까운 에클로자이트 시료들의 지화학조성은 반려암질 모암이 호주 동부 타스마나이드의 약 600-580Ma의 열곡대 내지 수동형 경계부 화성암류와 시공간적 대비를 시사한다. 이는 로스 조산대 내 에디아카라기 열곡대 고철질 화성활동의 첫 발견으로, 신원생대 동안 호주와 남극의 고지리적 대비에서 결여된

연결고리를 채우는 것이다. 나아가, 호주-남극의 동쪽 경계부에서 크라이오제니아기(약 670-650Ma) 에서 에디아카라기(약 600-580Ma)로 열곡활동이 해양쪽으로 이동한 사실과 함께, 각각 에디아카라기(약 590-570Ma)와 캠브리아기 초기(약 540-530Ma) 때 호 환경으로의 지구조적 전이를 제안한다. 이들 후기 신원생대 열곡활동들은 소위 고생대 곤드와나 '진흙 더미'에서 인지되는 태평양-곤드와나 저어콘 연령군(약 700-500Ma)의 기원 중 하나일 수 있다.

함망간규암 편암은 랜터만 산맥에서 얇은 레이어 형태로 드물게 산출하는데, 변성고철질 렌즈를 둘러싸는 석영장석질 편암류와 편마암류 내에 교호한다. 함망간규암의 강한 Ce 양의 이상은 수동형 경계부의 대륙사면 내지 대륙붕 환경에서 형성된 원양성 퇴적기원 모암 내에 함철망간 노듈이나 각 등이 포함되었음을 지지한다. 스페서틴이 풍부한 석류석, 피몬타이트-갈렴석이 풍부한 녹렴석, 펜자이트, 자철석, 석영의 광물조합은 상대적으로 산소분압이 높은 환경에서의 녹색편암상 내지 청색편암상의 조건을 지시한다. 수동형 경계부 퇴적암류들은 로스 조산운동의 맥락에서 중기 캠브리아기 때 변성작용을 경험하였다. 랜터만 산맥의 고압 변성암류들의 압력-온도 경로를 취합한 결과는 각기 다른 섭입-융기 경로를 가질 수 있음을 증명한다.

주요어: 에클로자이트, 단편적 저어콘 성장, 신원생대 후기 열곡활동, 함망간규암, 랜터만 산맥, 로스 조산대, 동곤드와나 경계부

ACKNOWLEDGEMENTS

I am indebted to many people who gave a lot of help and encouragement during the doctoral course. Above all, I am very grateful to my advisors, Profs. Moonsup Cho and Haemyeong Jung who led myself as a geologist and petrologist since my undergraduate years at Seoul National University. I deeply appreciate unreserved advice and constructive comments by thesis committee members, Profs. Insung Lee, Jung-Woo Park (Seoul National Univ.) and Yoonsup Kim (Chungbuk National Univ.), and Dr. Seung Ryeol Lee (KIGAM). In particular, this thesis could not be produced without Prof. Yoonsup Kim's support during the latter half of the doctoral course.

Geological field work and collecting rock samples in Antarctica, main targets of the PhD thesis, was impossible without enormous help of researchers in the KOPRI including Drs. Jong Ik Lee and Jusun Woo, and safety members of the OBK team. It was a great pleasure to have time with many friends and colleagues at Lab of Petrotectonics in SNU, Drs. Chul Lim, Yuyung Lee and Daeyeong Kim, and Junseok Na, Jihyuk Kim and Jeongmin Lee. Many thanks are also due to those of Lab of Tectonophysics in SNU, Drs. Munjae Park and Yi Cao, and other students including Yong Park. The members in CBNU are warmly thanked as well; Drs. Wonseok Cheong and Changhwan Oh, and Hyun Woo Aum, Bui Vinh Hau, Ji Yeong Park, Giun Han and Seonghyeok Mun. My thanks are also extended to Dr. Hyeoncheol Kim (KIGAM) for his encouragement and Dr. Keewook Yi (KBSI) for helping SHRIMP analyses. Prof. Thorsten Nagel (Aarhus Univ.) and Dr. Jinxue Du (China Univ. of Geosciences Beijing) are thanked for their suggestion in thermodynamic modelling.

Lastly, how on earth I could express my gratitude to my parents and brother who gave infinite love for over 30 years, taking this opportunity I would like to give words of thanks, respect and love to them. My sincere thanks should reach to my wife Jiyeon, who has been with me for a long time with unwavering faith in each other and will be together for the future as a lifetime partner. Abiding love of my family is a vital force of my life as a scientist and human being.

사사

박사 학위기간 동안 많은 분들의 도움과 격려가 있었기에 무사히 졸업할 수 있었다. 먼저 서울대 학부 시절부터 쭉 지질학, 암석학 연구자로 인도해주신 조문섭 교수님과 정해명 교수님, 두 분 지도교수께 깊이 감사드린다. 흔쾌히 박사논문 심사에 참여하시어 아낌없는 조언과 건설적인 비평을 주신 서울대 이인성 교수님, 박정우 교수님, 충북대 김윤섭 교수님, 지자연의 이승렬 박사님께도 감사드린다. 특히 박사학위 기간 후반부 과정에 대한 김윤섭 교수님의 지원 없이는 이 논문이 탄생하지 못했을 것이다.

박사학위 논문 주제인 남극 지질조사와 암석 시료 확보에는 극지연구소의 이종익 박사님, 우주선 박사님을 포함한 연구원 분들과 OBK 안전 요원분들의 도움이 결정적이었다. 서울대 암석지구조학 연구실에서 임철 박사님, 유영형, 대영형, 준석형, 지혁, 정민과 함께 했던 시간은 학위기간 동안 큰 즐거움이었으며, 가깝게 지낸 서울대 지체구조물리학 연구실의 문재형과 차오, 그리고 용이를 포함한 학생들에게도 감사드린다. 충북대의 정원석 박사님, 오창환 박사님, 현우형, 하우, 지영, 기운, 성혁에게도 고마움을 전한다. 격려해주신 지자연의 김현철 박사님과 슈림프 분석에 도움을 주신 기초연의 이기욱 박사님께도 감사드린다. 열역학 모델링에 대해 조언해주신 Thorsten Nagel 교수(오르후스대)와 Jinxue Du 박사(북경중국지질대)께도 감사드린다.

마지막으로, 학위기간을 포함한 30여 년 동안 무한한 사랑을 주신 아버지, 어머니, 동생에 대한 고마움을 차마 표현할 수 있겠나마는, 이 글을 빌어 감사와 존경과 사랑의 말씀을 전한다. 오랫동안 서로에 대한 변함없는 믿음으로 곁에 있어주고, 이제 인생의 반려자로써 미래를 함께할 아내 지연에게도 진심으로 고마움을 전한다. 가족들의 변함없는 사랑은 앞으로도 연구자로써, 한 사람으로써 인생을 살아가는 동력임이 분명하다.